Trinity College Dublin

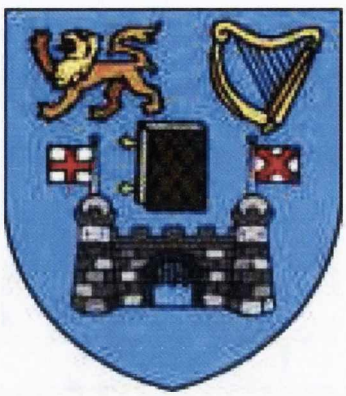

School of Physics

Plasmon resonance studies in silver nanoparticles arrays grown by Atomic Terrace Low Angle Shadowing (ATLAS)

A thesis submitted to the University of Dublin, Trinity College,
in application for the degree of Doctor in Philosophy
by

Floriano Cuccureddu

February 2009

To my parents, Sergio and Vittoria.

Declaration

This thesis is submitted by the under signed for the degree of Doctor in Philosophy at the University of Dublin.
It has not been submitted as an exercise for a degree at any other university.

Apart from the advice, assistance and joint effort mentioned in the under signed and in the text, this thesis is entirely my own work.
I agree that the library may lend or copy this thesis freely on request.

Acknowledgments

Five years are quite a long time, specially under the rain. One meets so many people, some of them will become friends while some other will be forgotten. It is thanks to all of them if the last five years have been an irreplaceable life experience. I met great people who made my staying enjoyable. Apart from the weather. And the food. And....ok, stop, let us spare the moaning.
Firstly, I would like to thank my supervisor Prof. I.V.Shvets for giving me the opportunity of working in his group and carry out this project.
I am grateful to Prof. S.Bohzko for the joint work on alumina surfaces.
I truly want to thank Prof.G.Cocco and Prof.S.Enzo for motivating me to go into research and showing me the real bright side of science during my undergrad studies.
I am sincerely grateful to Dr.Shane Murphy who worked with me when I first joined. We started the ATLAS project when many people around were ironically mistrustful. He taught me all the nasty "nuts and bolts" stuff and helped me out when more physics was needed.
I would like to thank my UNISS mate Dr.Giuseppe Manai (gaz) for he facilitated my landing in Ireland. So I should probably blame him!...but he actually was very helpful when I was first looking for a PhD. Graziegaz.
I am very grateful to Ciaran McEvoy with whom I shared the lab life for a while at about 45°C and 150dB. We had many conversations exchanging views about everything; I here confess I have constantly tried to steal english (and irish) expressions from him. He also was kind enough to proofread papers and this thesis for me which, I guess, is as much entertaining as making lousy electrical contacts.
I made some friends over here and, in random order, I start thanking Sumesh for offering me different perspectives on many aspects of life; we had extended discussions about every kind of art. He also filled my scientific gaps many times with his wide knowledge and gave me the chance of a great life experience bringing me straight to his own country (For which I expect him to come and visit mine). I would like to thank Rafa for introducing me to the "mumblism" and for being a great coffee manager at the beginning...then he became a scientist and all went lost. We spent pretty much the same time

here, surviving only with a sarcastic approach to the irish lifestyle. And then he brought Noa who we all have to thank for showing us the real meaning of life: running aimless and joyful just for the fun of it...that is some lesson. I am indebted to my bud Barry for the countless chats refreshed by his colloquial english and "slight" north-Dublin accent. That was some training for my ears. We have different opinions on the concept of "socializing" but I guess it is a mediterranean versus north-European clash. And we also shared a great time in India, where our opinion-mismatch did not matter anymore. If he only could have finished that book...I want to thank Han Chun for sharing with me the dark sides of a PhD. I think we talked also about science one or two times, whenever we ran out of interesting topics.
I would also like to thank my soccer buddies: Ken Concannon, Robbie Gu., Robbie Ga., Nigel, Tonaldinho and maybe someone else. My ankles are happy you let them live through. Sore but alive.
I would also like to thank a few staff members. Marie who helped me to sort out many annoying issues, Mick and Pat from the workshop, John Kelly for refereeing the first (and only) Magnetite Cup.
Thanks also to a few past and present group members who gave some kind of help, scientific or not: Roman, Ken, Sergio, Kevin the irish Texan, Paul and his Scotch, Cormac and his Mead, Jin, Sunil, Louise, Bala, Keith and, apart from the human tragedy, Californium.
I sure thank Ricardo for the time spent together inside and outside the soccer pitch and for sharing with me the least crowded barbecue party in the history of mankind (3 people...Guido, are you there?).
I want to thank a couple of friends I met only twice in the last years: Ed, Mike, Stone, Jeff and Matt who helped me quite a lot when I felt particularly blue suggesting that no matter how long the winter, there's a springtime ahead.
I can only thank Simona but she deserves much more than that, since there is not other person that supported me as much as she did. She coped with me and my dark views of the future at any stage of this experience. I can only say words and thank her a million times but it will never be enough.
Un grazie sincero va ai colleghi del "Carasau Team" con cui, purtroppo solo ultimamente, ho condiviso dei momenti di puro relax e "magnate" all'italiana. Adriele a cui sono debitore anche per l'aiuto offertomi quando la tesi era un mi-

raggio taaanto lontano. Guido per i continui suggerimenti e per la particolare interpretazione dell'accentistica sarda. Simone per gli elucidanti commenti a bollino rosso su piu'o meno ogni donzella nei paraggi. E ultimo ma non ultimo il mio connazionale Giovanni da Tissi che mi ha riportato un po'di sardita' "come si tocca" (che mi mancava come il pane!)Avanti Fortza Paris!
Grazie ai miei amici piu' fidati. Mauro, con cui ho condiviso praticamente ogni giorno in tempo reale e che mi ha sempre offerto la sua visione positiva delle cose, oltre che indimenticabili visite in Olanda (PJ!!!) e a Villa Amadori. Siamo riusciti nell'impresa di far figurare i nostri nomi sullo stesso articolo (Nanoletters!!!). Senza parlare della traversata europea...Such a memories...Ringrazio Giommaria per il continuo incitamento e per gli scambi di vedute su...tutto. C'ho messo quattro anni ma son riuscito a portarlo in terra dei celti.
Ringrazio sinceramente i miei genitori per il costante e incessante incoraggiamento anche se "ero lontano". E ringrazio me stesso per aver finito qualcosa che non mi andava proprio di lasciare a meta'.
And thanks to all the people that somehow, even for a few minutes, made my day better.

"Somewhere theres a siren singing
A song only he hears
All the strength that you might think
Would disappear...resolving"
E.V.

Summary

Nanotechnology refers to the study of nanomaterials aiming to understand the physical properties and phenomena that materials show at the nanometre scale. A key goal in nanotechnology is acquiring the ability to manipulate nanostructures in order to produce nanomaterials with desired properties. Many techniques have been explored and they can be divided into top-down and bottom-up approaches. Success in the formation of nanowires, planar or not, has been achieved but from the literature it stands there are difficulties in forming regular and well-ordered arrays on insulating substrates. A novel technique was developed in our laboratories called Atomic Terrace Low Angle Shadowing (ATLAS). The ATLAS approach uses the basic principle of shadowing of a glancing incidence flux of atoms by the step-bunched terraces of a vicinal single crystal substrate. The Atomic Terrace Low Angle Shadowing (ATLAS) technique is valuable in that it is not material-specific but rather universal in its application unlike many other processes for bottom-up fabrication of nanowires.

The ATLAS technique requires the use of vicinal surfaces and, in order to fulfill these requirement, a study of the morphological surface evolution upon annealing of sapphire, α-Al_2O_3, was carried out. Sapphire samples were annealed for different times at high temperature, such as 1100°C, to produce a step and terrace morphology. Lower temperatures did not produce any satisfactory results on any of the samples. Samples characterization was done using atomic force microscopy (AFM) and revealed that flat samples did not show any step bunching even for long annealing times. This can be due to the temperature

which was too low to trigger the rearrangement of surface atoms, as confirmed by annealing of flat substrates at higher temperature. In contrast, vicinal samples provided good results since the high temperature annealing was able to induce the step bunching process. The surface morphology presents a number of coalescence points, i.e. local areas where two steps merge and form a higher step. The formation of step and terrace morphology makes C-plane oriented α-alumina a suitable substrate to act as a template for nanowire growth using the ATLAS technique.

The nanostructures growth performed by ATLAS is affected by several critical parameters such as the deposition angle, the step orientations, the deposition rate etc. A detailed study was carried out in order to find out the morphological growth of the metal on the substrate. Silver nanoparticles arrays were routinely produced and it was found that each key parameter can heavily influence the morphology of the nanostructures. Also, the particle size was found to be related to the deposition time, increasing with longer times. Post-annealing of the nanoparticle samples induces a reorganization and gradually destroys the long-range order. As well as silver nanoparticles arrays, nanowires of iron and cobalt were routinely produced showing the same parameters dependence as observed for silver.

Linear chains and two dimensional arrays of silver nanoparticles have applications in several fields and are of particular interest in optics and advanced photonics. A new sub-field has been suggested and called "plasmonics" with the aim to study potential applications of the Surface Plasmon Resonance (SPR) phenomenon. SPR is due to the interaction between an external electromagnetic field and the electrons. The oscillating dipole field generated can

have strong coupling with the light at a resonance frequency within the visible wavelength range and this can be exploited for optical and sensor applications, channeling of flow of electromagnetic energy over hundreds of nanometers without significant loss, electromagnetic energy transport, sub-wavelength photonic waveguiding etc. The optical properties of silver nanoparticles arrays were investigated by means of UV-vis spectroscopy which revealed a different plasmonic response of the samples depending on the light polarization. The dipole-dipole interaction between the particles causes a split of the plasmonic peak which might find applications in integrated photonics as transmission lines of electromagnetic energy. In the aligned nanostructures produced, the shift of the resonance peak proves that strong near-field coupling, which in turn is the mechanism for energy transport, is present. Also it was found that different morphologies can give rise to a similar optical response due to the local contributions to the overall response.

A qualitative insight of the studied phenomena was given by using the discrete dipole approximation DDA as a numerical approximate method to calculate the interaction between electromagnetic radiation and objects of arbitrary geometry. DDA analysis suggests that the experimentally observed splitting is not due to shape effects but to the electrodynamic interaction between the particles. An enhanced collective behavior is responsible for the red-shift (longitudinal polarization) and blue-shifts (transversal polarization) of the resonance peak. Furthermore, volume effects resulted less strong than shape effects.

Publications and Conferences

"Concept of a nanowire array magnetoresistance device"

I.V.Shvets, H.C.Wu, V.Usov, **F.Cuccureddu**, S.K.Arora and S.Murphy

Appl. Phys. Lett. 92, 023107 (2008)

"Planar nanowire arrays formed by atomic-terrace low-angle shadowing"

F.Cuccureddu, V.Usov, S.Murphy, C.O.Coileain, and I.V.Shvets

Rev.Sci.Inst. 79, 053907 (2008)

"Plasmon Resonance in Silver Nanoparticles Arrays Grown by Atomic Terrace Low-Angle Shadowing"

F.Cuccureddu, S.Murphy and I.V.Shvets, M. Porcu and H. W. Zandbergen

Nanolett. 8, 10, 3248-3256 (2008)

"Surface morphology of c-plane Sapphire after annealing at high temperature"

F.Cuccureddu, S.Murphy and I.V.Shvets, M. Porcu and H. W. Zandbergen, N.S. Sidorov and S. I. Bozhko

In preparation

"Silver Nanoparticles Arrays Grown By Using ATLAS (Atomic Terrace Low Angle Shadowing)"

F.Cuccureddu, S.Murphy and I.V.Shvets, M. Porcu and H. W. Zandbergen

IOM3 3rd international Conference on Nanomaterials and Nanomanufacturing

CRANN, TCD, Dublin, Ireland

December 17-18, 2007

"Plasmon Resonance in Silver Nanoparticle Arrays Grown By ATLAS"

F.Cuccureddu, S.Murphy and I.V.Shvets

VC-IAN2008 Conference on Interaction among Nanostructures

Orlando, FL, USA

February 3-7, 2008

List of Figures

List of Tables

List of Abbreviations

AACVD - Aerosol Assisted Chemical Vapor Deposition

AES - Auger Electron Spectroscopy

ALCVD - Atomic Layer Chemical Vapor Deposition

AFM - Atomic Force Microscopy/Microscope

AGFM - Alternating gradient field magnetometre

ATLAS - Atomic Terrace Low Angle Shadowing

CVD - Chemical Vapor Deposition

DDA - Discrete Dipole Approximation

DF - Dark Field (TEM)

DUV - Deep Ultra-violet Lithography

EBL - Electron Beam Lithography

EUV - Extrem Ultra-violet Lithography

FDTD - Finite-Difference Time-Domain

FEL - Fast-Entry Loadlock

FIB - Focused Ion Beam

FMR - Ferromganetic Resonance

GLAD - Glancing Low Angle Deposition

HRTEM - High Resolution Transmission Electron Microscopy/Microscope

HRXRD - High Resolution X-Ray Diffraction

ICT - Information Communication Technology

LED - Light Emitting Diodes

LPCVD - Low Pressure Chemical Vapor Deposition

LSPR - Localized Surface Plasmon Resonance

MBE - Molecular Beam Epitaxy

MOCVD - Metallorganic Chemical Vapor Deposition

NPPR - Nanoparticle Plasmon Resonance

PBG - Photonic Band Gap

PECVD - Plasma Enhanced Chemical Vapor Deposition

PSTM - Photonic Scanning Tunneling Microscopy

PVD - Physical Vapor Deposition

REM - Reflection Electron Microscopy

RHEED - Reflection High Energy Electron Diffraction

SAM - Self Assembled Monolayer

SAW - Surface Acoustic Wave

SEM - Scanning Electron Microscopy/Microscope

SERS - Surface-Enhanced Raman Spectroscopy

SPM - Scanning Probe Microscopy

SPP - Surface Plasmon Polariton

SPR - Surface Plasmon Resonance

STM - Scanning Tunneling Microscopy/Microscope

TEM - Transmission Electron Microscopy/Microscope

UHV - Ultra High Vacuum

XPS - X-ray Photoelectric Spectroscopy

YBCO - Yttrium Barium Copper Oxide

List of Symbols

$\mathbf{a_1}$, $\mathbf{a_2}$, $\mathbf{a_3}$, $\mathbf{c}$ - Lattice constants

$\mathbf{B}$ - Magnetic Induction

c - Speed of light

$\mathbf{D}$ - Dielectric Displacement

$\mathbf{E}$ - Electric Field

$\mathbf{H}$ - Magnetic Field

$\hbar$ - Planck's constant

hkil - Miller-Bravais indices

$\mathbf{J_{ext}}$ - Current density

k_0 - Free-space wavevector

k_{SP} - Surface plasmon wavevector

k_{light} - Light wavevector

k(ω) - Extinction coefficient

m_e - Electron mass

m_{eff} - Effective electron mass

n(ω) - Complex refractive index

$\mathbf{P}$ - Polarization

R - Reflectivity

α - polarizability

β - propagation constant

Γ - Collision frequency

$\varepsilon(\omega)$ - Complex dielectric function

ε_0 - Electric permittivity of vacuum

$\varepsilon_1(\omega)$ - Real part of the complex dielectric function

$\varepsilon_2(\omega)$ - Imaginary part of the complex dielectric function

ε_{met} - Dielectric function of the metal layer

ε_{diel} - Dielectric function of the dielectric layer

λ - Wavelength

ϱ - Charge density

τ - Relaxation time

χ - Dielectric susceptibility

ω - Frequency of light

ω_p - Plasma frequency

Contents

"Per me si va ne la città dolente,
per me si va ne l'etterno dolore,
per me si va tra la perduta gente.
[...]
Lasciate ogne speranza, voi ch'intrate"

D.Alighieri

("La Divina Commedia, Inferno III, 1-9")

Part I

Introduction and Theoretical background

Chapter 1

General introduction: Nanotechnology

> It was a bright cold day in April, and the clocks were striking thirteen.
>
> *G. Orwell (1984)*

The many different definitions of nanotechnology reflect the broad spectrum of research fields that this new discipline offers, often requiring inter- and multi-disciplinary efforts. Nanotechnology is a technology of design, fabrication and application of nanomaterials aiming to understand the physical properties and phenomena that materials show at the nanometre scale. The structures involved are extremely small, a nanometer is one billionth of a meter, or 10^{-9}m and is approximately the length of 10 hydrogen or 5 silicon atoms in a row.

Nanotechnology is not the simple miniaturization from micrometer scale down to nano-meter scale because if it is true that materials in the micrometer scale exhibit mostly the same physical properties as the bulk form, in the nanometer scale they can exhibit properties far different from the bulk. For example, crystals at the nanometer scale have a low melting point and reduced lattice constants, since the number of surface atoms becomes a significant fractions of the total number of atoms and the surface energy plays an important role in thermal stability. The preparation in nanometer size form allows many materials to maintain stable crystal structures at much lower temperatures than they would on macroscopic scale, so ferroelectric and ferromagnetic materials could lose their ferroelectricity and ferromagnetism when they are shrunk to the nanometers scale. Even bulk semiconductors may become insulators if scaled to 1-5 nm size [1]. A key goal in nanotechnology is acquiring the ability to manipulate nanostructures in order to produce nanomaterials with desired properties. Many techniques have been explored and they can be divided into top-down and bottom-up approaches. Here a brief introduction and discussion will be given on the main techniques for the fabrication of nanostructures and nanopatterns, focusing on the distinction between top-down and bottom-up approaches [2].

1.1 Top-Down Techniques - Lithography

The top-down approach involves molding or etching materials into smaller components. This approach has been practiced with great success by the

electronics industry to manufacture integrated circuits. Lithography is the process of transferring a pattern onto a reactive polymer film (resist) which will be used to replicate that pattern into an underlying substrate [3]. While many techniques have been developed in the last half century employing various radiation sources, they all share the same technical approaches and are based on the same fundamentals [2].

1.1.1 Photolithography

Photolithography is the most widely used technique in microelectronic fabrication. The process consists of producing a mask carrying the pattern information and transferring it onto a photoactive polymer, using some optical technique. The resist material is applied as a thin coating over a substrate and is exposed through a mask in such a way that light illuminates only selected areas. Then the exposed resist is subjected to a development process that leads to a three dimensional relief image which is a replication of the opaque and transparent areas of the mask. After the etching process, the resist is removed by stripping to produce a positive or negative relief image on the substrate. Conventional photolithography is capable of fabricating features of 200nm and above. To obtain higher resolutions, shorter wavelength light and lens systems with larger numerical apertures can be used [2].

Deep Ultra-Violet lithography (DUV) based on exposure at wavelengths below 300nm, presents far more difficult technical challenges but allows one to obtain patterns with a minimal size of 100nm [4]. Extreme UV (EUV) lithography with wavelengths in the range of 11-13nm has been explored and is a strong

candidate for achieving dimensions of 70nm and below even if this techniques has many technical drawbacks [5, 6].

1.1.2 Electron beam lithography (EBL)

In EBL a focused beam of electrons is rastered over a surface coated with a radiation sensitive polymeric material. The beam can be used to write patterns of very high resolution [7, 8]. The electron beam can be focused to a few nanometers in diameter and deflected either electromagnetically or electrostatically. EBL is the most powerful tool for the fabrication of features as small as 3-5 nm [9]. The maximum resolution is limited by forward scattering of the electrons in the resist layer and back scattering from the underlying substrate. Also it is quite a slow process and it is impossible to deflect an electron beam to cover a large area [2].

1.1.3 X-Ray lithography

X-rays are an alternative radiation source with wavelengths in the range of 0.04 to 0.05 nm, for high resolution pattern replication into polymeric resist materials [10]. Absorption of X-ray photons results in the formation of a photoelectron which undergoes elastic and inelastic collisions within the absorbing material producing secondary electrons which are responsible for the chemical reactions in the resist film. A major limitation is given by the mask which does not cast a sharp shadow degrading the pattern resolution (penumbral shadowing). The resolution limit of X-ray lithography is around 25nm [11].

1.1.4 Focused Ion Beam (FIB) lithography

Focused ion beam technology has been rapidly developed in the last 30 years into a very attractive tool in lithography, etching, deposition and doping [12]. Since scattering of ions in the MeV range is several order of magnitude less than that for electrons, ion beam lithography offers improved resolution [13]. The advantages of FIB include its high resist exposure sensitivity, higher than that of EBL, and its negligible ion scattering in the resist as well as low back scattering from the substrate. FIB offers advantages also for the fabrication of magnetic nanostructures: ions are heavier than electrons and thus the FIB is much less influenced by the magnetic properties of the material. However, FIB lithography suffers from some drawbacks such as lower throughput and extensive substrate damage [2].

1.1.5 Soft lithography

Soft lithography has been developed as an alternative to photolithography for micro and nanofabrication and comprises a set of non-photolithographic techniques that are based on the printing of Self Assembled Monolayers (SAMs) and moulding of liquid precursors [14, 15]. Microcontact printing is a technique that uses an elastomer stamp with relief on its surface to generate patterned SAMs on the surfaces of both planar and curved substrates [16]. Nanoimprint lithography has demonstrated both high resolution and high throughput for fabricating nanometer scale structures [17]. A stamp with the desired features is pressed onto a thermoplastic polymer previously spun onto a substrate, causing a deformation in the plastic layer. The patterned polymer left on

the substrate is used for further processing (dry etching or lift-off) or for use directly as a device component. A challenge is presented regarding the ability of exact alignment of multi-layers, as well as the control of temperature and pressure during the process [18].

1.2 Bottom-Up Techniques

The bottom-up approach comprises techniques capable of building structures by combining smaller components, as opposed to carving them out of larger ones (top down) and so it basically refers to the build-up of a material from the bottom: atom-by-atom, molecule-by-molecule or cluster-by-cluster [2].

1.2.1 Nanomanipulation and Nanolithography

Nanomanipulation and nanolithography are based on scanning probe microscopy (SPM) which offers the possibility to directly manipulate molecules and nanostructures on a surface [19].

Nanomanipulation. In addicion to the ability to image surface topography with atomic resolution, the interactions or forces between the tip and the sample surface offer a means to carry out precise manipulation of nanostructures on a surface [20, 21]. STM tips are able to drag the atoms along the surface and positions the atoms at a desired spot. The motion of the manipulated atom can be parallel to the surface so that the bond between the atom and the surface is never broken or perpendicular with the STM tip so that it lifts the adsorbed atom from the surface and carries it to a desired position [21].

Similarly AFM has been investigated for nanomanipulation and three basic manipulation modes have been explored, depending on the nature of the interactions between the tip and the adatoms: pushing, pulling and sliding [22]. SPM manipulation offers some advantages: the SPM tip has a nanoscale sharp point which offers extremely fine positional control in all three dimensions; moreover, it offers the possibility to manipulate and characterize in-situ at the same time. However, some drawbacks are the small scanning area, the slow scanning speed and the required high quality of SPM tips [19].

Nanolithography. SPM-based nanolithography has been exploited to obtain patterns with a minimal size of 10-20 nm [23] or 1 nm in UHV [24]. Nanometer holes can be formed using low energy electrons from a STM tip when a pulsed electric voltage is applied in the presence of sufficient gas molecules between the substrate and the tip. Nanostructures can be created using field evaporation by applying bias pulses to the STM tip-sample tunnelling junction [25]. The AFM tip can be used as a sharply pointed tool in order to produce fine grooves on the sample surface by direct contacting, writing or scratching [26].

1.2.2 Self-assembly Techniques

Self assembly is a generic term used to describe a process where the arrangement of molecules, small particles and atoms occurs spontaneously under the influence of certain forces such as chemical reactions, electrostatic attraction and capillary forces [27]. Self-assembly offers a versatile approach to the fabrication of nanoscale devices. The key idea in the self-assembly process is that the final structure is close to or at thermodynamic equilibrium, it thus tends to

form spontaneously and to reject defects. The following discussion will provide a general picture about the most common approaches used in self assembly of nanocrystals and nanorods [28].

Chemical Techniques: CVD and Sol-gel

CVD (Chemical Vapor Deposition) is a process where a chemically reacting volatile compound of a material is deposited, with other gases, to produce a nonvolatile solid that deposits on a suitably placed substrate. CVD has been extensively studied [29] and different variations have been investigated: MOCVD for metallorganic precursors, PECVD plasma is used to enhance chemical reactions, LPCVD (low pressure CVD), laser enhanced or assisted CVD, AACVD (aerosol-assisted CVD) and ALCVD (atomic layer CVD) [2]. Sol-gel processing is widely used and capable of producing nanoparticles, nanorods and thin films offering many advantages including low processing temperature and molecular level homogeneity [30].

Physical Techniques: PVD, MBE and Sputtering

Physical Vapor Deposition (PVD) is a general term used to describe several methods to deposit thin films by the condensation of a vaporized form of the material onto various surfaces. The coating method involves purely physical processes rather than a chemical reaction at the surface as in CVD.
Molecular Beam Epitaxy (MBE) is a highly controlled evaporation process from a variety of sources in ultrahigh-vacuum of typically 10^{-10}torr [31]. In MBE the evaporated atoms do not interact with each other under such a low pressure; the ultra clean environment and the slow growth rate enable the

precise fabrication of nanostructures and nanomaterials with absence of impurities and contamination. The main attributes of MBE include:

- low growth temperature.
- low growth rate.
- individually controlled evaporation sources.
- possibility of *in situ* analysis.

Sputtering is a process based on the ejection of atoms from a solid target material due to bombardment by energetic ions. Although various sputtering techniques have been developed, the fundamentals of the process remain the same [32]. Compared to MBE, sputtering shows some differences: it requires different operating conditions, like a relatively high pressure and atoms do collide with each other before reaching the substrate.

1.3 Top-Down vs Bottom-Up: Advantages and Disadvantages

The urgency of developing new techniques able to substitute lithography rapidly increases. At smaller scales optical lithography doesn't have the required resolution and other lithography techniques, such as electron beam, X-ray or extreme UV lithography are either slow, very expensive or complicated by tough technical challenges [5, 33].

Besides, top-down techniques such as lithography can cause significant atomic-scale damage to the processed patterns as well as the possibility of introducing

defects during the etching process. For instance, nanowires made by lithography are not smooth and contain a lot of impurities and structural defects on the surface. Such imperfections have a strong impact on the physical properties and surface chemistry of nanomaterials, since the surface/volume ratio is very large. The surface imperfections result in a reduced conductivity (due to inelastic surface scattering), which in turn leads to the generation of excessive heat imposing extra challenges in device design and fabrication [2]. However, top-down techniques will continue to play an important role in the synthesis and fabrication of nanostructures.

Bottom-up is nothing new in material synthesis: polymers are fabricated in organic chemistry by connecting individual monomers together and in crystal growth, the growth species, after impinging onto the substrate, assemble into a crystal structure [34, 35]. However, the bottom-up approach plays an important role in the fabrication of nanostructures because when the structures fall into a namometer scale, top-down approaches are no longer suitable [2]. Consumers and industry require smaller and faster PCs and chips, and therefore the technology inside has to shrink continually. In the next decade, traditional "top-down" lithographic fabrication techniques are expected to reach their physical limits in their ability to produce sub-50 nm features [5]. "Bottom-up" fabrication methods based on parallel self-assembly of complementary functionalities offer a new strategy for the successful fabrication of next-generation devices. The bottom-up approach also promises a better chance to obtain structures with less defects, more homogeneous chemical composition, and better short and long range ordering. All of this is due to the fact that the driving

force is mainly the reduction of the Gibbs free energy, so that the nanostructures produced are in a state that is closer to thermodynamic equilibrium. In practice, both top-down and bottom-up methods are useful and future applications will likely require the successful integration of both "top-down" and "bottom-up" methodologies [36].

1.4 Nanowires as basis for new ICT devices

Only a small number of nanowire-related publications in the current literature can be considered interesting when it comes to practical applications in planar electronic devices. This is due to the nature of the papers: many of them relate to non-conducting nanowires or to conducting nanowires grown on conducting substrates where the charge transfer will be carried out by the substrate itself instead of the nanowires. In many cases, the nanowires are grown perpendicularly to the substrate making uniform parallel positioning difficult because many of them do not follow the same azimuth creating a disorganized pattern [37, 38]. Nonetheless there are demonstrations of technological advances in prototypes devices based on nanowires such as transistors of a single nanowire [39, 40], memory devices [41] etc. Some success in the formation of planar arrays of nanowires has been achieved by growing Au on vicinal Si(111) [42] but there are likely limitations in relation to the choice of the materials and to the thickness of the wires. Most studies of nanowire arrays face the difficulty of forming regular arrays on insulating substrates. The development of this project provides a method of fabrication of well-ordered arrays of nanowires of many materials with a range of magnetic, electronic,

optical and optoelectronic properties on insulating, semiconducting or metal substrates. The Atomic Terrace Low Angle Shadowing (ATLAS) technique is valuable in that it is not material-specific but rather universal in its application unlike many other processes for bottom-up fabrication of nanowires. The ATLAS approach uses the basic principle of shadowing of a glancing incidence flux by the atomic or step-bunched terraces of a vicinal single crystal substrate [43]. In the present project the substrate utilized will be sapphire, α-Al_2O_3, an excellent insulator that cannot be made conducting by doping.

References

[1] R.W. Kelsall, I.W. Hamley, and M. Geoghegan. *Nanoscale Science and Technology.* Wiley, UK, (2005).

[2] B. Bhushan. *Springer Handbook of Nanotechnology.* Springer, Berlin, (2004).

[3] D. Brambley, B. Martin, and P.D. Prewett. *Adv.Mater.Opt.Electron.*, 4:55, 1994.

[4] M.K. Herndon, R.T. Collins, R.E. Hollinsworth, P.R. Larson, and M.B. Johnson. *Appl.Phys.Lett.*, 74:141, 1999.

[5] T. Ito and S. Okazaki. *Nature*, 406:1027, 2000.

[6] B.Q. Wua and A. Kumar. *J.Vac.Sci.Tech.B*, 25:1743, (2007).

[7] W. Chen and H. Ahmed. *Appl.Phys.Lett.*, 62:1499, 1993.

[8] S.Y. Chou. *Proc.IEEE*, 85:652, 1997.

[9] C. Vieu, F. Carcenac, A. Pepin, Y. Chen, M. Mejias, A. Lebib, L. Manin-Ferlazzo, L. Couraud, and H. Lunois. *Appl.Surf.Sci*, 164:111, 2000.

[10] L.F. Thompson and M.J. Bowden. *Introduction to Microlithography.* The American Chemical Society, Washington D.C., 1983.

[11] T. Kitayama, K. Itoga, Y. Watanabe, and S. Uzawa. *J.Vac.Sci.Technol.*, B18:2950, 2000.

[12] P.D. Prewett and G.L.R. Mair. *Focused Ion Beams from Liquid Metal Ion Sources.* Wiley, New York, 1991.

[13] S. Matsui, Y. Kojima, Y. Ochiai, and T. Honda. *J.Vac.Sci.Technol.*, B9:2622, 1991.

[14] Y. Xia, J.A. Rogers, K.E. Paul, and G.M. Whitesides. *Chem.Rev.*, 99:1823, 1999.

[15] P. Kim, K.W. Kwon, M.C. Park, S.H. Lee, S.M. Kim, and K.Y. Suh. *Biochip Journal*, 2:1, (2008).

[16] R. Jackman, R. Wilbur, and G.M. Whitesides. *Science*, 269:664, 1995.

[17] B. Heidari, Maximov I., E.L. Sarwe, and L. Montelius. *J.Vac.Sci.Technol.*, B17:2961, 1999.

[18] H. Schift. *J.Vac.Sci.Tech. B*, 26:458, (2008).

[19] A.A. Tseng, A. Notargiacomo, and T.P. Chen. *J.Vac.Sci.Tech.*, 23:877, (2005).

[20] D.M. Eigler and E.K. Schweizer. *Nature*, 344:524, 1990.

[21] J.A. Stroscio and D.M. Eigler. *Science*, 254:1319, 1991.

[22] C. Baur, A. Bugacov, B.E. Koel, A. Madhukar, N. Montoya, T.R. Ramachandran, A.A.G. Requicha, R. Resch, and P. Will. *Nanotechnology*, 9:360, 1998.

[23] K. Matsumoto, M. Ishii, K. Segawa, Y. Oka, B.J. Vartanian, and J.S. Harris. *Appl.Phys.Lett.*, 68:34, 1996.

[24] J.W. Lyding, T.C. Shen, J.S. Tucher, and G.C. Abeln. *Appl.Phys.Lett.*, 64:2010, 1994.

[25] X. Hu, D. Sarid, and P. von Blanckenhagen. *Nanotechnology*, 10:209, 1999.

[26] A. Notargiacomo, V. Foglietti, E. Cianci, G. Capellini, M. Adami, P. Faraci, F. Evangelisti, and C. Nicolini. *Nanotechnology*, 10:458, 1999.

[27] R. Bogwe. *Ass.Aut.*, 28:211, (2008).

[28] Y. Huang, X. Duan, Q. Wei, and C.M. Lieber. *Science*, 291:630, 2001.

[29] K.L. Choy. *Prog.Mater.Sci.*, 48:57, 2003.

[30] J.D. Wright and N.A.J.M. Sommerdijk. *Sol-gel Materials: Chemistry and Applications.* Gordon and Breach Science Publishers, Amsterdam, 2001.

[31] E.H.C. Parker (ed). *The Technology and Physics of Molecular Beam Epitaxy.* Plenum Press, New York, (1985).

[32] M. Ohring. *The Materials Science of Thin Films.* Academic Pres, San Diego, CA, (1992).

[33] C. Barth and M. Reichling. *Nature*, 414:54, (2001).

[34] K. Byrappa and T. Ohachi. *Crystal Growth technology.* William Andrew Publishing, New York, USA, (2003).

[35] A. Pimpinelli and J. Villain. *Physics of Crystal Growth.* Cambridge University Press, Cambridge, UK, (1998).

[36] E. Di Fabrizio and F. Romanato. *M.R.S.Proc.*, 921E:211, (2006).

[37] C.M. Zhou and D. Gall. *Appl.Phys.Lett.*, 88:203117, (2006).

[38] K.D. Harris, D. Vick, E.J. Gonzalez, T. Smy, K. Robbie, and M.J. Brett. *Surf.Coat.Tech*, 138:185, (2001).

[39] L.J. Lauhon, M.S. Gudiksen, C.L. Wang, and C.M. Lieber. *Nature*, 420:6911, (2002).

[40] D. Wang, B.A. Sheriff, M. McAlpine, and J.R. Heath. *Nano Res.*, 1:9, (2008).

[41] A.M. Song, M. Missous, P. Omling, P. Maximov, W. Seifert, and L. Samuelson. *Appl.Phys.Lett.*, 86:042106, (2005).

[42] K.N. Altmann, J.N. Crain, A. Kirakosian, J.L. Lin, D.Y. Petrovykh, F.J. Himpsel, and L. Rosio. *Phys.Rev.B*, 64:035406, (2001).

[43] I.V. Shvets, H.C. Wu, V. Usov, F. Cuccureddu, S.K. Arora, and S. Murphy. *Appl.Phys.Lett.*, 92:023106, (2008).

Chapter 2

The ATLAS project

> The individual has always had to struggle to keep from being overwhelmed by the tribe. If you try it, you will be lonely often, and sometimes frightened. But no price is too high to pay for the privilege of owning yourself.
>
> *F. Nietzsche*

The bottom-up approach to the fabrication of nanostructures has become a popular subject in current science and engineering circles, especially for the fabrication of nanowires of many different materials, driven by a wide range of potential applications [1, 2, 3, 4, 5, 6]. Looking at the literature, two principal geometries can be identified: either the nanowires orient out of the substrate surface plane [2, 7, 8, 9, 10, 11, 12] or lie in plane with the surface [13, 14, 15, 16, 17, 18]. The latter are particularly interesting from the point of

view of planar electronic applications. Planar nanowire arrays can be prepared by step flow growth [19]. However, preparation of nanowires by the step-flow growth mechanism is restricted in that it only works well for certain materials on certain metal or semiconductor surfaces. This is unfortunate if one is interested, for example, in forming arrays on insulating, e.g. oxide substrate. Our approach is based on utilizing the shadowing effect by the step-and-terrace morphology of a vicinal surface on a molecular beam at oblique incidence to the substrate surface. We term this approach atomic-terrace low-angle shadowing (ATLAS) [20]. This method utilizes the advantages of the bottom-up fabrication and its principal attraction is its relative simplicity. The method does not involve multiple lithography steps and can be applied to metal, semiconductor, or oxide surfaces alike, thus, making it potentially interesting for practical applications. Vicinal surfaces can be formed by annealing a surface that is off cut from a low-index orientation [21, 22, 23]. The width of the atomic terraces can be controlled by the off-cut angle. Therefore, the separation between the nanowires within the array and their width could be readily controlled.

2.1 Deposition at oblique angles

Recently, low-temperature physical vapor deposition of thin films at highly oblique vapor incidence angles has emerged as a distinct new microfabrication technology [24, 25]. This technique is mainly used to grow a variety of columnar films with different morphologies [26, 27], but it has also been possible to produce linear arrays of nanoparticles [28]. The idea has been known for a

while and developed, for the first time, more than 40 years ago [29, 30] and subsequently modeled [31] and investigated through the years [32, 33, 34].
The GLAD technique, developed by Robbie and Brett [35, 36], represents an evolution of oblique thin-film deposition, in which the substrate is not only tilted to a high angle relative to the incoming flux (the substrate tilt angle α), but also rotated about an axis normal to the substrate (given by the substrate rotation angle φ) allowing one to sculpt columnar thin films easily [26, 27, 37]. The GLAD technique has been applied to sputtering systems as well as e-beam and thermal evaporation systems, with no need for vapor collimation as long as the distance from the vapor source to the substrate is an order of magnitude higher than the substrate dimensions [9, 38, 39, 40]. Huth et al. managed to grow ordered arrays of nanostripes by using the MBE (Molecular Beam Epitaxy) technique at shallow incident angle with the substrates held at high temperatures of 450°C [41, 42, 14]. However, even in this case the dimensions of the nanostructures grown were far larger than those that can be grown with ATLAS. The nanodots and nanowires reported have widths that range from 25 to 100 nm and thicknesses ranging from 19 to 40nm.

2.2 The ATLAS system

The aim of the project is the fabrication of nanowires and nanoparticles arrays using glancing angle deposition. The morphology, texture, and crystallography of the nanowires can be controlled by varying the process parameters such as deposition flux, deposition angle and substrate miscut and symmetry. Most of the theoretical and practical studies on obliquely deposited films have been

concerned with deposition on initially flat substrates [8, 26, 27, 43]. In our case, we intend to use vicinal substrates annealed to provide steps and terraces of atomic scale. These surfaces offer the possibility to use atomic or bunched steps to provide the shadowing effect [14, 15, 41, 42]. To achieve this unusual mode of growth one needs to direct the flux at a shallow angle with respect to the substrate surface, say 0.5 - 5 degrees off the surface plane. During the deposition stage the collimated beam of evaporant atoms forming the wires, directed at the substrate in a direction nearly parallel to the atomic terraces formed by the substrate steps, is well collimated by geometry by placing the evaporator at a large working distance from the substrate, e.g. 1 - 3 m, depending on the width of the desired nanowires. Only a very small layer thickness will be deposited using this shallow deposition technique. In this way, for example, dopant nanowires can be deposited on vicinal Silicon surfaces generating, after annealing, doped semiconducting nanowires. Moreover different subsets of magnetic nanowires can be grown along with spacer nanowires producing configurations with areas of different coercivity [20].

An important issue is represented by the regularity of the step-and-terrace morphology of the substrate. An ideal candidate for the ATLAS technique would be characterized by an extended homogeneity of the steps which shape the surface showing uniformity both at short and long range. This configuration would allow to grow extremely regular nanowires whose distribution and characteristics are determined only by the growth parameters. As it will be shown and extensively discussed in the experimental section, the situation in reality is quite different because no substrate can provide such an ideal

morphology. The terrace width is actually subject to fluctuations which statistically provide a width distribution that can be quantified by means of a standard deviation from a mean value. The width distribution has to be taken into account since it heavily affects the nanostructures grown on top of the terraces. Due to the lack of uniformity, the distance between nanowires is not constant but related to the distance between adjacent steps. This becomes, in turn, of crucial relevance since the physical properties will be affected. If two neighbor steps are, for instance, too close to each other, the nanowires grown on them will be consequently very close giving rise to cross-talk between different wires which could compromise the properties. An additional factor to be taken in account is the stability and the orientation of the vicinal planes. It will be shown in the experimental section that vicinal substrates can be characterized by a pronounced faceting where a surface decomposes into two or more planar surfaces. Due to the facets formation, the steps change temporarily direction turning away from their original orientation and depriving the surface of ideal uniform straight steps. The presence of faceting affects the nanostructure growth since, for instance, two nanowires may come into contact wherever two steps, as a result of faceting, join together. In this case it might be useful estimating the average distance, and its distribution, between two junctions since this distance can be considered as the mean portion of step running straight along a defined direction. This distance will offer an estimate of the average length at which every nanowire (or nanoparticles chain) can extend before joining a second wire. However, the faceting itself is not necessarily an irreparable problem depending on how long the desired nanowires have to

be for the intended applications. In fact, whenever the average distance allows to grow nanowires of the desired and needed length the faceting becomes a secondary issue since the merging points will be out of the area of interest.
As shown in Fig.2.1 the nanowires can be grown on the inner or outer step edge of a vicinal substrate.

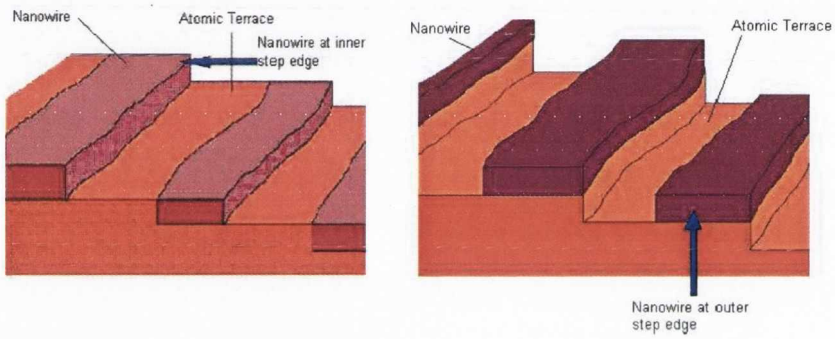

Figure 2.1: Schematic representation of nanowire formation at shallow angle deposition

A schematic of the basic ATLAS system is shown in Fig.2.2. All other depositions, i.e. protective overlayers, etc. are deposited using a conventional MBE configuration, i.e. flux normal to the substrate surface.

The characterization of the samples is done using High Resolution X-Ray Diffraction (HRXRD), Atomic Force Microscopy (AFM), as well as optical analysis.
In principle, two distinct growth mechanisms can be identified depending on the terraces orientation. Fig.2.1 (right side), shows the atomic flux directed from an outer step edge to a lower terrace (descending step direction). The deposition angle β between the beam and the surface is only $1°-3°$ in order that some areas of the atomic terraces are exposed to the beam, while others are

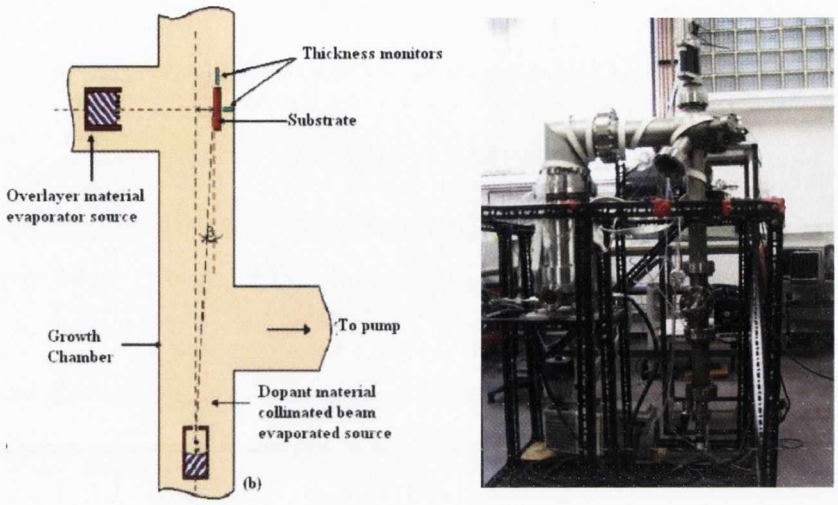

Figure 2.2: Schematic representation and photograph of the first ATLAS system

geometrically shadowed by atomic steps. As a result, the deposited material grows along the terrace step edges. Changing the deposition angle β changes the nanowire width which is given by:

$$width \approx h\left(\frac{1}{\alpha} - \frac{1}{\alpha+\beta}\right) \tag{2.1}$$

where, h is a step height, α is a miscut angle, and β is a deposition angle, defined as the angle between the surface and the incident beam. Both α and β are assumed to be small. Rotating the substrate by 180° the beam is almost parallel to the plane of the atomic terraces (ascending step direction). The step faces provide the bonding sites and the deposited material grows along the steps similar to the step-flow growth mechanism [19].

2.2.1 Nucleation and growth of nanostructures

Nucleation. For thin film growth the condensation of the vapor atom is determined by its interaction with the impinged surface whose atoms attract the vapor atoms [19, 44, 45]. As a result of the attraction, the incoming atom loses its velocity component normal to the surface, provided the incident kinetic energy is not too high. The atom is then physically adsorbed ("adatom") but it may not be in complete thermal equilibrium. It may move over the surface because of thermal activation from the surface and/or its own kinetic energy parallel to the surface. Once landed, during its finite residence time on the surface, the adatom can interact with other adatoms and form stable clusters or be incorporated into the surface (chemical adsorption) with release of the heat of condensation. If not adsorbed, the adatom desorbs into the vapor phase. Therefore, the condensation is the net result of an equilibrium between the adsorption and desorption process [46]. The same concepts can be applied to nanowires or nanoparticles growth for which the deposition temperature should be chosen such that the adatom free path on the substrate is limited to a few nanometers [47].

The probability for the adatom to be incorporated is called "sticking" coefficient and measured by the ratio of the amount of material condensed on a surface to the total amount impinged. The capturing of incident atoms can be analyzed considering a head-on collision of an atom with one-dimensional lattice and shows a unity condensation coefficient for kinetic energies up to 25 times the desorption energy Q_{des}. The capture for three-dimensional lattice is less complete because of the greater stiffness. If the impinging atom is lighter

than the substrate atom or it has higher kinetic energy, the sticking coefficient can be appreciably less than unity [19, 48].

The captured atom will lose all but a small part of the energy within the three lattice oscillations for comparable masses. The mean stay time for the adatom moving over the surface, before being desorbed, is:

$$\tau_s = \frac{1}{\nu} exp\left(\frac{-Q_{des}}{kT}\right) \tag{2.2}$$

where ν is the adatom surface-vibrational frequency. τ_e, the mean relaxation time required for an adatom to thermally equilibrate with the substrate, is:

$$\tau_e \approx 2\tau_s exp\left(\frac{-Q_{des}}{kT}\right) \tag{2.3}$$

At high binding energies $Q_{des} \gg kT$ and τ_e is small: the thermal equilibrium occurs rapidly. If $Q_{des} \sim kT$ the adatoms do not equilibrate rapidly and the condensation coefficient is less than unity. The Einstein relation for the Brownian movement gives the diffusion distance for the equilibrated adatom:

$$X = 2^{1/2} a \cdot exp\left(\frac{Q_{des} - Q_d}{2kT}\right) \tag{2.4}$$

where a is the jump distance between the absorption sites and Q_d is the activation energy for a surface-diffusion jump.

Nucleation theory. The growth of thin film performed near equilibrium conditions can be analyzed by using thermodynamic arguments. A theory regarding

the homogeneous and heterogeneous nucleation was developed by Volmer and Weber [49]. In this theory, which takes into account the total free energy of formation of a cluster of adatoms, the clusters form by collision of adatoms on the substrate surface or also in the vapor phase when the supersaturation is high. Assuming that bulk thermodynamical quantities can be applied to describe small clusters the radius of the critical nucleus is given by:

$$r^* = \frac{2\sigma_{cv}V}{kTln(p/p_e)} \tag{2.5}$$

where σ_{cv} is the condensate-vapor free energy, V is the volume condensed from supersaturated vapor of pressure p to the equilibrium pressure p_e.
The critical free energy is given by:

$$\Delta G^* = \frac{16}{3}\pi\frac{2\sigma_{cv}^3}{\Delta G_v^2}\varphi(\vartheta) \tag{2.6}$$

with ΔG_v being the Gibbs free energy per unit volume and φ depends on the contact angle ϑ: $\varphi(\vartheta) = 1/4(2-3cos\vartheta+cos^3\vartheta)$. For some ϑ values, clusters with smaller critical free Gibbs energy will form at steps rather than on flat surfaces and the concentration of nuclei at steps would be higher leading to a step-decoration effect.

Growth considerations. The subsequent process after nucleation is the growth of the nuclei to continuous films or bigger islands. The driving force behind the growth is the balance and minimization of surface and interface energies (where the surface energy is the reversible work per unit area required to create

a surface) summarized in the Bauer criterion in 1958 [50] and leading to three different growth modes. In the case of metal-on-oxide growth the parameters needed to taken into account are the surface free energy of the clean oxide in vacuum (γ_{ox}), the deposited metal (γ_m), and the interfacial free energy ($\gamma_{m/ox}$) which is typically much smaller than the surface energy. Using the equation:

$$\Delta\gamma = \gamma_m + \gamma_{m/ox} - \gamma_{ox} \tag{2.7}$$

when $\Delta\gamma > 0$, the oxide surface tends to maximize its exposed area leading to the formation of 3D particles without monolayer formation in the so-called Volmer-Weber (VW) or 3D metal growth mode. Conversely, if the surface energy between of the film is lower than that of the substrate, then $\Delta\gamma < 0$ and a layer-by-layer growth mode, also called 2D or Frank-van der Merwe growth (FM), is predicted. In the intermediate case one or sometimes several monolayers grow in the layer-by-layer mode before the formation of 3D islands starts. This is known as Stranski-Krastanov (SK) growth and is related to the misfit strain at the interface. Anyway near-equilibrium growth is a very slow process and in reality film growth is typically carried out far from equilibrium where kinetic processes dominate [51, 48]. The epitaxial growth of thin films using the MBE technique, where a supersaturated molecular beam is applied to grow film rapidly, is a non-equilibrium process determined by kinetic phenomena, so that the resulting film morphologies can deviate more or less from the thermodynamic picture. The supersaturated molecular beam can result for example in the formation of novel metastable phases. The important considerations that determine the film morphology are substrate defects such as steps, kinks,

dislocations which act as capture sites, and the kinetic processes involved such as adsorption, diffusion, nucleation, desorption etc. One of the most important considerations is the effect of steps on adatom diffusion because steps introduce the so-called Ehrlich-Schwoebel barrier to diffusion between terraces which regulates interlayer mass transport [52, 53]. The extent of the interlayer mass transport can determine whether the film morphology will be 3D (Volmer-Weber), 2D (Frank-van der Merwe) or somewhere between (Stranski-Krastanov) because the height of the Ehrlich-Schwoebel barrier at step and island edges determines whether adatoms can diffuse across or be reflected by steps, leading to a specific surface morphology. When all step- and island-edges reflect diffusing adatoms the interlayer mass transport is negligible and 3D growth mode dominates. If the barrier to diffusion across both step- and island-edges is low 2D or layer-by-layer growth is obtained. The intermediate case of SK growth is obtained where the diffusion behaviour on the substrate surface lends itself to layer-by-layer growth i.e. step-edges are non-reflective but the diffusion on top of the film is limited or island-edges are reflective. A full discussion of these topics is given in [54].

References

[1] M. Gleiche, L.F. Chi, and H. Fuchs. *Nature*, 403:173, (2000).

[2] G.S. Wu, T. Xie, X.Y. Yuan, Y. Li, L. Yang, Y.H. Xiao, and L.D. Zhang. *Solid St.Comm.*, 134:485, (2005).

[3] D.H. Cobden. *Nature*, 409:32, (2001).

[4] J. Grabowska, K.K. Nanda, E. McGlynn, J.P. Mosnier, and M.O. Henry. *Surf. Coat. Tech.*, 200:1093, (2005).

[5] L.J. Lauhon, M.S. Gudiksen, C.L. Wang, and C.M. Lieber. *Nature*, 420:6911, (2002).

[6] K. Fan, B. Shen, W. Wang, and J. Deng. *J.Mol.Struct.*, 422:191, (1998).

[7] N.J. Quitoriano and T.I. Kamins. *J.Appl.Phys.*, 102:044311, (2007).

[8] C.M. Zhou and D. Gall. *Appl.Phys.Lett.*, 88:203117, (2006).

[9] M. Suzuki, K. Nagai, S. Kinoshita, K. Nakajima, K. Kimura, T. Okano, and K. Sasakawa. *Appl.Phys.Lett.*, 89:133103, (2006).

[10] G. Richter, K. Hillerich, D.S. Gianola, R. Monig, O. Kraft, and C.A. Volkert. *Nanolett*, 9:3048, (2009).

[11] P. Li, H. Liu, F. Xu, and Y. Wei. *Mat.Chem.Phys.*, 112:393, (2008).

[12] A.J. Yin, L. Li, W. Jian, A.J. Bennett, and J.M. Xu. *Appl.Phys.Lett.*, 79:1039, (2001).

[13] A. Cazacu, S. Murphy, and I. Shvets. *Phys.Rev.B*, 74:045413, (2006).

[14] J. Oster, M. Kallmayer, L. Wiehl, H.J. Elmers, H. Adrian, F. Porrati, and M. Huth. *J.Appl.Phys.*, 97:014303, (2005).

[15] Y.F. Guan and A.J. Pedraza. *Nanotechnology*, 16:1612, (2005).

[16] D. Whang, S. Jin, Y. Wu, and C.M. Lieber. *Nano letters*, 3:1255, (2003).

[17] X.F. Duan, C.M. Niu, V. Sahi, J. Chen, J.W. Parce, S. Empedocles, and J.L. Goldman. *Nature*, 425:274, (2003).

[18] K.N. Altmann, J.N. Crain, A. Kirakosian, J.L. Lin, D.Y. Petrovykh, F.J. Himpsel, and R. Losio. *Phys.Rev.B*, 64:035406, (2001).

[19] K. Byrappa and T. Ohachi. *Crystal Growth technology.* William Andrew Publishing, New York, USA, (2003).

[20] I.V. Shvets, H.C. Wu, V. Usov, F. Cuccureddu, S.K. Arora, and S. Murphy. *Appl.Phys.Lett.*, 92:023106, (2008).

[21] L. Pham Van, O. Kurnosikov, and J. Cousty. *Surf.Sci.*, 411:263, (1998).

[22] O. Kurnosikov, L. Pham Van, and J. Cousty. *Surf.Sci.*, 459:256, (2000).

[23] Y. Shiratsuchi, M. Yamamoto, and Y. Kamada. *J.Jap.Appl.Phys.*, 41:5719, (2002).

[24] Y.P. Zhao, D.X. Ye, G.C. Wang, and T.M. Lu. *Nano Letters*, 2:351, (2002).

[25] M.O. Jensen and M.J. Brett. *IEEE Transactions on Nanotech.*, 4:2, (2005).

[26] K.D. Harris, D. Vick, E.J. Gonzalez, T. Smy, K. Robbie, and M.J. Brett. *Surf.Coat.Tech*, 138:185, (2001).

[27] J. Lintymer, J. Gavoille, N. Martin, and J. Takadoum. *Surf.Coat.Tech.*, 174:316, (2003).

[28] A. Sugawara and M.R. Scheinfein. *Phys.Rev.B*, 56:R8499, (1997).

[29] L. Holland. *J.Opt.Soc.Amer.*, 45:376, (1953).

[30] T.G. Knorr and R.W. Hoffman. *Phys.Rev.*, 113:1039, (1958).

[31] D. Vick, S.K. Friedrich, L.J. anc Dew, m.J. Brett, K. Robbie, M. Seto, and T. Smy. *Thin Solid Films*, 339:88, (1999).

[32] P. Meakin and J. Krug. *Phys.Rev.A*, 46:3390, (1992).

[33] Y. Taga and T. Motohiro. *J.Cryst.Growth*, 99:638, (1990).

[34] C. Teichert, J. Barthel, H.P. Oepen, and J. Kirschner. *Appl.Phys.Lett.*, 74:588, (1999).

[35] K Robbie and M.J. Brett. *J.Vac.Surf.Films*, 15:1460, (1997).

[36] M.O. Jensen and M.J. Brett. *IEEE Trans.Nanotech.*, 4:1536, (2005).

[37] D.A. Gish, M.A. Summers, and M.J. Brett. *Phot.Nanostr.-Fund.Appl.*, 4:23, (2006).

[38] A. Sugawara, T. Coyle, G.G. Hembree, and M.R. Scheinfein. *Appl.Phys.Lett.*, 70:1043, (1997).

[39] K. Robbie, L.J. Friedrich, S.K. Dew, T. Smy, and M.J. Brett. *J.Vac.Technol.A*, 13:1032, (1995).

[40] C. Buzea, K. Kaminska, G. Beydaghyan, T. Brown, C. Elliott, C. Dean, and K. Robbie. *J.Vac.Technol.B*, 23:2545, (2005).

[41] M. Huth, K.A. Ritley, J. Oster, H. Dosch, and H. Adrian. *Adv.Funct.Mater.*, 12, No.5:333, (2002).

[42] J. Oster, M. Huth, L. Wiehl, and H. Adrian. *J.Magn.Magn.Mater.*, 272-276:1588, (2004).

[43] J.R. Frederick, J. D'Arcy-Gall, and D. Gall. *Thin Solid Films*, 494:330, (2006).

[44] D.M. Mattox. *Handbook of physical vapor deposition (PVD) processing.* Noyes Publishing, New York, USA, (1998).

[45] H. Vehkamaki. *Classical nucleation theory in multicomponent systems.* Springer, Berlin, (2006).

[46] R.F. Bunshah. *Handbook of deposition technologies for films and coatings.* Noyes Publications, USA, (1994).

[47] B. Bhushan. *Springer Handbook of Nanotechnology.* Springer, Berlin, (2004).

[48] A. Pimpinelli and J. Villain. *Physics of Crystal Growth.* Cambridge University Press, Cambridge, UK, (1998).

[49] M. Volmer and A. Weber. *Z.Phys.Chem.*, 119:277, (1925).

[50] E. Bauer. *Z.Kristallogr.*, 110:372, (1958).

[51] J. Venables. *Introducion to Surface and Thin Film Processes.* Cambridge University Press, Cambridge, UK, (2000).

[52] R.L. Schwoebel and E.J. Shipsey. *J.Appl.Phys.*, 37:3682, (1967).

[53] G. Ehrlich and F.G. Hudda. *J.Chem.Phys.*, 44:1039, (1966).

[54] D.A. King and D.P. Woodroof, editors. volume 8 of *The chemical physics of solid surfaces.* Elsevier, Amsterdam, (1997).

Chapter 3

α-Alumina as a template to grow nanowires

Put your hand on a hot stove for a minute, and it seems like an hour.
Sit with a pretty girl for an hour, and it seems like a minute.
THAT's relativity.
A.Einstein

3.1 Introduction

Sapphire (α-Al_2O_3) is used in a range of technological fields; e.g. in electronics as a substrate for epitaxial thin film growth [1], in high power optics [2], chemical catalysis [3] etc.

In the following, the morphology of low miscut and vicinal α-Al_2O_3 c-plane substrates as a function of anneal time and temperature in air have been investigated using atomic force microscopy.

For this project, C-plane Sapphire was chosen as an substrate for the ATLAS technique. One of the tasks is, in fact, generating regular and planar nanostructures of metal on oxide for electronics and/or photonics applications. As it is going to be explained, among the various oxides, α-Al_2O_3 was selected because its surface reconstructs with a fairly regular step-and-terrace morphology upon annealing at high temperature, offering an appropriate template for the growth of nanostructures by ATLAS. Also, the annealing procedure for Sapphire is quite straightforward since it is carried out in air, unlike other oxides such as $SrTiO_3$, shortening the experimental time. Besides, α-Al_2O_3 is a material of large technological interest and although the amount of research concerning it is remarkable, much is still unknown.

3.2 Structure and properties of α-Alumina

Sapphire has an hexagonal crystal structure [4]. In the hexagonal unit cell the lattice vectors of the basal plane (sides $\mathbf{a}_1$, $\mathbf{a}_2$ and $\mathbf{a}_3$) are equivalent, with an angle of 120 degrees between the two. Side $\mathbf{c}$ is not equal to $\mathbf{a}$ and is normal to the basal plane, as shown in Fig.3.1. The planes and directions in the crystal lattice are denoted by Miller-Bravais Indices. The Miller-Bravais lattices provide a four numbered description of location within the crystal. The generic representation of a direction is $\langle hkil \rangle$ and of a plane is (hkil).

The structure of α-Al_2O_3 places atoms in two types of sites: hexagonal and

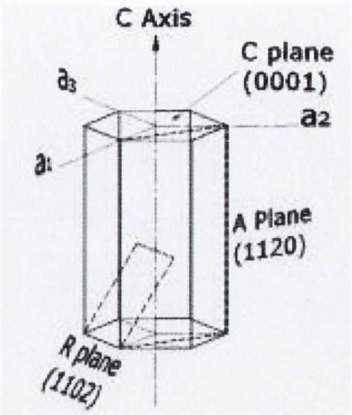

Figure 3.1: Orientation Planes of α-Alumina (Al_2O_3)

octahedral (Fig.3.2). The hexagonal corner sites are occupied by oxygen anions. The octahedral sites are present between a face which adjoins two layers of vertical stacking. Aluminum cations are in 2/3 of the octahedral sites, and oxygen anions are in 1/3 of the octahedral sites. Each oxygen is shared between four octahedra. The oxygen presence in octahedral sites permits strong bonding and, therefore, gives rise to the characteristic properties of alumina. For substrate applications, the most commonly encountered crystallographic planes in α-Al_2O_3 are the c-, r- and a-planes.

C-plane (0001) sapphire substrates are the most widely used, particularly to grow III-V and II-VI compounds such as GaN for blue Light Emitting Diodes (LED) and laser diodes [5]. In addition, it is useful for infrared detector applications [6].

A-plane(1120) sapphire substrates provide a uniform dielectric constant and high insulation for hybrid microelectronic applications [7]. High T_c superconductors such as yttrium barium copper oxide (YBCO) can also be grown on

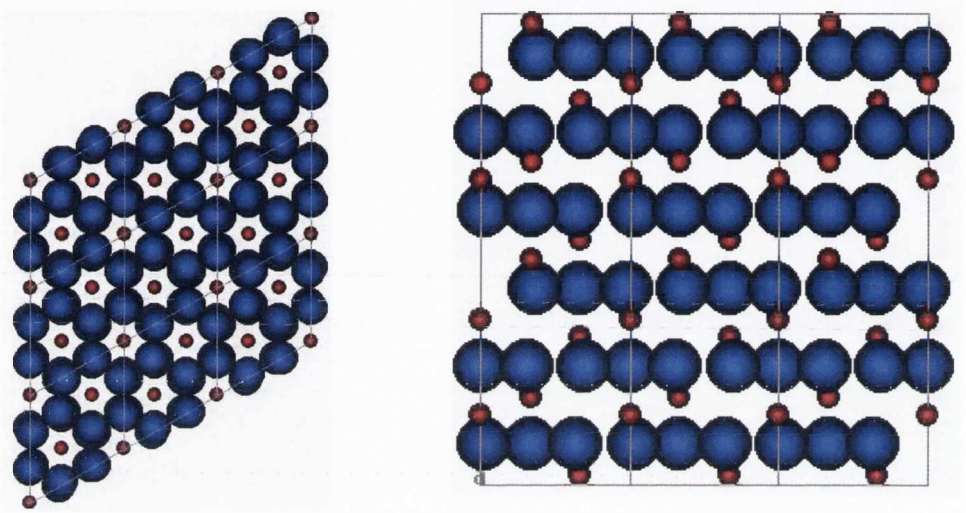

(a) C-plane of α-Alumina.

(b) Sideview of stacking α-Alumina planes along <1-210> direction.

Figure 3.2: α-Alumina structure.

a-plane sapphire substrates [8].

R-plane(1012) sapphire substrates are used for the hetero-epitaxial deposition of silicon for microelectronic IC applications. Sapphire is an excellent choice for hybrid substrates such as microwave IC's because of its high dielectric constant. In addition, when coated with an epitaxial silicon process, high speed IC and pressure transducers can be created [9]. Superconducting components, high impedance resistors and growth of GaN are among the other applications [10]. Sapphire has been investigated and often used as a deposition substrate for many other materials, e.g. AlN has been studied for surface acoustic wave (SAW) materials and applications in wireless communication [11]; ZnO nanorods have been grown on c-sapphire as an alternative to GaN for wide band-gap device applications [12]. The growth of several metals on

sapphire has been studied, for example copper and palladium [13] as well as silver and gold [14, 15, 16, 17, 18, 19].

We decided to focus on c-plane sapphire as a template for growing nanowires because it can form surface with well-ordered steps [20, 21, 22, 23]. The (0001) surface can terminate at three chemically different surface terminations. They are an oxygen surface layer, a surface with two aluminium layers or a surface ending between the two aluminium layers. The last one has been predicted to have the lowest surface energy from theoretical calculations whilst the oxygen-terminated surface has the highest surface energy [24]. Several studies have been carried out in order to follow the surface evolution at high temperature. Using a dynamic scanning force microscopy technique [25] an hexagonal arrangement of atoms after surface reconstruction was observed[26]. It has also been found that, in addition to the (1×1) termination, the(0001) surface exists in several ordered phases that can be reversibly transformed into each other by thermal treatment and oxygen exposure [27]. The high-temperature phase is known to be oxygen-deficient [28] with a large $(\sqrt{31} \times \sqrt{31})R \pm 9$ unit cell observed by electron [29] and X-ray diffraction [30]. The surface of this superstructure has been demonstrated to promote the self-organization of nanoclusters [26].

3.3 Research on α-Alumina

As alumina is such a good insulator, investigations of the surface structures by conventional methods utilising electrons as a probe such as scanning electron microscopy (SEM), transmission electron microscopy (TEM) etc. have often

been limited. Atomic force microscopy (AFM) provides a powerful technique to study the alumina surface [20, 21, 22, 23]. Successful investigations of vicinal surfaces of alumina at the nanometre scale were also performed by using high-resolution transmission microscopy (HRTEM)and reflection electron microscopy (REM) [31, 32, 33].

Annealing of (0001) α-alumina samples for several hours in air produces a terrace-and-step morphology consisting of wide terraces (typically several hundreds of nm) separated by surface steps (typically 1-5 nm) whose height is usually a multiple of c (where c=1.3 nm is the unit cell parameter of alumina along the c-axis). Different authors have observed the formation of stepped surfaces after annealing at temperatures above 1000°C and the surface evolution in the 1000-1500°C temperature range has been explored to give an insight in processes of step formation on the alumina surface [20, 21, 22, 34]. In particular, it has been found that annealing gives rise to steps up to $\sim$2 nm in height. Furthermore, annealing at 1400°C between 10 min and 8 hours leads to facet nucleation and facet coarsening where the faceting process is attributed to the gathering of several $c/6$ steps in order to build faceted steps with a height equal to or higher than c [35].

Faceting obviously enhances the complexity of the surface evolution of sapphire. Basically different processes can be identified during the step growth like step coalescence, step decomposition [21], step faceting and step bunching [20, 33]. From the point of view of this project step bunching is definitely the most interesting process because the gathering of steps, due to a step-to-step attractive interaction at long distances [36], allows the formation of multiple

steps whose height is considerable and more useful for shallow angle deposition. As well as the classical parameters such as temperature and time, Kurnosikov *et al.* [23] showed that the values of miscut angle (θ) and azimuth orientation angle (φ) can control the surface evolution, and it is often difficult to separate the respective influences. Step bunching is expected to be a transient phenomenon preceding the step faceting and its disappearance rate is related, among the other parameters, to the miscut angle θ: the higher θ, the slower the rate [23].

Step bunching is a complex phenomenon of surface evolution where two or more steps tend to join together [37, 38, 39, 40, 41, 42, 43]. A considerable number of theoretical studies are available regarding the evolution and motion of step trains but nevertheless the origin of this particular kinetic instability is still debated and is unclear due to the fact that step bunching can be seen in various physical situations [44, 45, 46, 47]. The asymmetric kinetic behavior due to the Ehrlich-Schwoebel effect is a possible cause. Incorporation rates of adatoms from upper and lower terraces are significatively different and this can generate an instability of the step trains motion during step-flow growth [48, 49]. Step-step long range interactions were proposed to play an important role in step bunching and also impurities can interfere with the kinetic processes and create more complex instabilities [50, 51, 52, 53, 54, 55]. A model proposed by Frank in 1958 suggested that impurities on the surface can destabilize the uniform step train during evaporation (or the crystal growth) impeding the motion of the step and reducing its velocity [54, 56]. If all the steps had the same velocity step bunching would not occur, so different ve-

locities are necessary and they can be due to the presence of elasticity and impurities [51, 52, 53]. In particular impurities seem to be a reasonable explanation for alkali metal halides where particles present on the surface are observed to pin the steps. It is reported that common segregation of Ca, Mg, Ba, Si etc. affects the step and surface structure evolution of alumina samples: the presence of such impurities forces the steps to bend around them generating mesoscopic bunching [57]. The mechanism of step bunching remains rather unclear and a complex interplay among the discussed possible causes and maybe some others, such as electromigration [58], chemical potential [59] and elasticity [51, 52], is likely to be responsible for it.

C-plane oriented α-alumina proves to be a suitable candidate to act as a template for the nanowire growth using the ATLAS technique due to the step and terrace morphology achievable by high temperature annealing. From preliminary studies r-plane sapphire seems to be a reasonable candidate as well.

References

[1] T.J. Minvielle, R.L. White, M.L. Hildner, and R.J. Wilson. *Surf.Sci.*, 366:L755, (1996).

[2] P.E. Dyer, S.R. Jackson, P.H. Key, W.J. Metheringham, and M.J.J. Schmidt. *Appl.Surf.Sci.*, 96-98:849, (1996).

[3] I. Stara, V. Nehasil, and V. Matolin. *Surf.Sci.*, 365:69, (1996).

[4] P.R. Kenway. *J.Am.Ceram.Soc.*, 77:349, (1994).

[5] M.M. Wong, J.C. Denyszyn, C.J. Collins, U. Chowdhury, T.G. Zhu, K.S. Kim, and Dupuis R.D. *Elec. Lett.*, 37:1188, (2001).

[6] G.M. Smith, J.M. Redwing, R.P. Vaudo, E.M. Ross, J.S. Flynn, and V.M. Phanse. *Appl.Phys.Lett.*, 75:25, (1999).

[7] L.J. Singh, Z.H. Barber, Y. Miyoshi, Y. Bugoslavky, W.R. Branford, and L.F. Cohen. *Appl. Phys. Lett.*, 84:2367, (2004).

[8] M. Shirakawa, M. Miura, T. Ohazama, Y. Shingai, A. Saito, M. Mukaida, and S. Ohshima. *Physica C*, 412-414:1277, (2004).

[9] C. Mueller, S. Alterovits, E. Croke, and G. Ponchak. *Mat.Res.Soc.Symp.Proceed.*, 809:193, (2004).

[10] J.J. Huang, K.C. Shen, W.Y. Shiao, Y.S. Chen, T.C. Liu, T.Y. Tang, Huang C.F., and C.C. Yanga. *Appl.Phys.Lett.*, 92:231902, (2008).

[11] T. Suetsugu, T.and Yamazaki, S. Tomabechi, K. Wada, K. Masu, and Tsubouchi K. *Appl.Surf.Sci*, 117:540, (1997).

[12] J. Grabowska, K.K. Nanda, E. McGlynn, J.P. Mosnier, and M.O. Henry. *Surf.Coat.Tech*, 200:1093, (2005).

[13] C.L. Pang, H. Raza, S.A. Haycock, and G. Thornton. *Surf.Sci.*, 460:L510, (2000).

[14] J. Feng, W. Zhang, and W. Jiang. *Phys.Rev.B*, 72:115423, (2005).

[15] K. Luo, X. Lai, C.W. Yi, K.A. Davis, K.K. Gath, and Goodman D.W. *J.Phys.Chem.B*, 109:4064, (2005).

[16] D.G. Van Campen and J. Hrbej. *J.Phys.Chem.*, 99:16389, (1995).

[17] F.X. Bock, T.M. Christensen, S.B. Rivers, L.B. Doucette, and R.J. Lad. *Thin Solid Films*, 468:57, 2004.

[18] P.R. Ribic and G. Bratina. *Surf. Sci.*, 109:13138, (2006).

[19] M. Yoshimoto, T. Maeda, T. Ohnishi, H. Koinuma, O. Ishiyama, M. hinohara, M. Kubo, R. Miura, and A. Miyamoto. *Appl.Phys.Lett.*, 67:2615, (1995).

[20] J.R. Heffelfinger, M.W. Bench, and C.B. Carter. *Surf.Sci.*, 370:L168, (1997).

[21] L. Pham Van, O. Kurnosikov, and J. Cousty. *Surf.Sci.*, 411:263, (1998).

[22] O. Kurnosikov, L. Pham Van, and J. Cousty. *Surf.Sci.*, 459:256, (2000).

[23] O. Kurnosikov, L. Pham Van, and J. Cousty. *Surf.Interface Anal.*, 29:608, (2000).

[24] S. Blonski and S.H. Garofalini. *Surf.Sci.*, 295:263, (1993).

[25] A. de Lozanne. *Science*, 291:2561, (2001).

[26] C. Barth and M. Reichling. *Nature*, 414:54, (2001).

[27] T.M. French and J.A. Somorjai. *J.Phys.Chem.*, 74:2489, (1970).

[28] M. Gautier, J.P. Duraud, and M.J. Pham Van, L.and Guittet. *Surf.Sci.*, 250:71, (1991).

[29] C.C. Chang. *J.Appl.Phys*, 39:5570, (1968).

[30] G. Renaud, B. Villette, L. Vilfan, and A. Bourret. *Phys.Rev.Lett.*, 73:1825, (1994).

[31] T. Hsu and Y. Kim. *Surf.Sci.*, 258:119, (1991).

[32] Y. Kim and T. Hsu. *Surf.Sci.*, 258:131, (1991).

[33] Y. Kim and T. Hsu. *Surf.Sci.*, 275:339, (1992).

[34] P.R. Ribic and G. Bratina. *Surf. Sci.*, 601:44, (2007).

[35] J.R. Heffelfinger and C.B. Carter. *Surf.Sci.*, 389:188, (1997).

[36] T. Kimoto, A. Itoh, and H. Matsunami. *Appl.Phys.Lett*, 66:3645, (1995).

[37] T. Maroutian, L. Douillard, and H.J. Ernst. *Phys.Rev.Lett.*, 83:4353, (1999).

[38] C. Schelling, G. Springholz, and F. Schaffler. *Phys.Rev.Lett.*, 83:995, (1999).

[39] I. Berbezier, B. Gallas, A. Ronda, and J. Derrien. *Surf.Sci.*, 412:415, (1998).

[40] P. Tejedor, P. Smilauer, C. Roberts, and B.A. Joyce. *Phys.Rev.B*, 59:2341, (1999).

[41] A.V. Latyshev, L.A. Litvin, and A.L. Aseev. *Appl.Surf.Sci.*, 130:139, (1998).

[42] J.E. Van Nostrand, S.J. Chey, and D.G. Cahill. *Phys.Rev.B*, 57:12536, (1998).

[43] A. Pascale, I. Berbizier, A. Ronda, A. Videcoq, and A. Pimpinelli. *Appl.Phys.Lett.*, 89:104108, (2006).

[44] S.N. Filimonov and B. Voigtlander. *Surf.Sci.*, 549:31, (2004).

[45] M. Esser, E. Zoethout, H.J.W. Zandvliet, H. Wormeester, and B. Poelsema. *Surf.Sci.*, 552:35, (2004).

[46] V. Zielasek, L. Feng, Z. Yuegang, J.B. Maxson, and M.G. Lagally. *Phys.Rev.B*, 63:201320, (2001).

[47] J.M. Blakely, S. Tanaka, and R.M. Tromp. *J. Electron.Microsc.*, 48:747, (1999).

[48] R.L. Schwoebel and E.J. Shipsey. *J.Appl.Phys.*, 37:3682, (1966).

[49] G. Ehrlich and F.G. Hudda. *J.Chem.Phys.*, 44:1039, (1966).

[50] M. Sato and M. Uwaha. *Phys.Rev.B*, 51:11172, (1995).

[51] R. Asaro and R.A. Tiller. *Metall.Trans.*, 3:1789, (1972).

[52] C. Duport, P. Nozieres, and J. Villain. *Phys.Rev.Lett.*, 74:134, (1995).

[53] J.P. Van der Eerden and H. Muller-Krumbhaar. *Phys.Rev.Lett.*, 57:2431, (1986).

[54] N. Cabrera and D.A. Vermileya. *Growth and Perfection of Crystals.* Wiley, New York, (1958).

[55] J.P. van der eerden and H. Muller-Krumbhaar. *Morphology and Growth Unit of Crystals.* TerraPub, Tokio, (1989).

[56] A. Pimpinelli and J. Villain. *Physics of Crystal Growth.* Cambridge University Press, Cambridge, UK, (1998).

[57] N. Ravishankar and C.B. Carter. *J.Mater.Res.*, 17:98, (2002).

[58] S. Stoyanov and V. Tonchev. *Phys.Rev.B*, 58:1590, (1998).

[59] F.K. Men, L. Feng, P.J. Wang, C.H. Chen, D.L. Cheng, and J.L. Lin. *Phys.Rev.Lett.*, 88:096105, (2002).

Chapter 4

Surface Plasmon Polariton Resonance

Talent hits a target no one else can hit; Genius hits a target no one else can see.

A.Schopenhauer

4.1 Introduction

Surface Plasmons, also known as Surface Plasmon Polaritons (SPPs), are propagating wave solutions of Maxwells equations at the interface between a dielectric and a metal [1]. They are bound to the interface and coupled to a light field which has a maximum at the interface and decays exponentially in

the directions perpendicular to the interface [2](Fig.4.1).

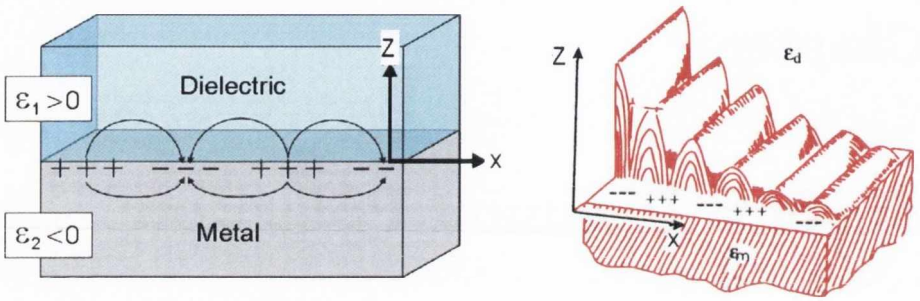

Figure 4.1: Scheme of a surface plasmon polariton on a metal/dielectric interface.

SPPs are the the result of the resonant interaction between a light wave and collective oscillations of the free electrons of the conductor (the term surface plasmon polaritons reflects this hybrid nature) at the metal interface and have an evanescent tail into both the metal and the dielectric. As a resonant phenomenon, the SPP near field is considerably enhanced with respect to the exciting light field. SPPs can manifest themselves both on flat thin films and metal nanostructures with several differences that will be highlighted later on. Usually surface plasmon resonance (SPR) refers to planar surfaces and Localized surface plasmon resonance (LSPR) refers to nanometer-sized metallic structures. SPPs on metal nanoparticles are particularly interesting and have attracted a great deal of interest in the last decades [3, 4]. In fact, optical spectra of noble metal clusters show characteristic resonance lines due to the collective excitations of their conduction electrons. The ability of these structures to sustain coherent electron oscillations leading to electromagnetic fields confined to the metallic surface have attracted considerable interest and have been intensively investigated both for the fundamental physics involved

and for potential applications [1, 5, 6]. In the 1980s SPPs became a matter of interest for chemists as well, since the electric-field enhancement around metal nanostructures was found to have a key role in surface-enhanced Raman spectroscopy [7]. Recently the development of nanofabrication methods such as electron beam lithography (EBL), self-assembly and the availability of more powerful simulation tools led to a renewed interest in this field, especially for potential applications in advanced photonics with the development of subwavelength photonic devices [2]. The name "plasmonics" has also been suggested for this subfield of modern optics [1, 8]. Many parameters control the optical properties of these clusters; for instance the peak position, intensity and width of the plasmon resonance depend on the dielectric properties of the metal nanoparticles with silver clusters having higher plasmon energies than gold clusters. But also shape and size influence the spectral position as outlined in Figs.4.2 and 4.3 for typical Ag and Au nanoparticles [9]. A different nanoparticles shape and/or size generates a different optical response with the resonance peak accordingly shifted (visually corresponding to a different color).

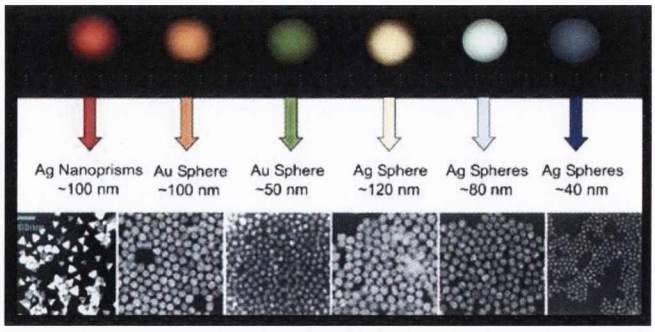

Figure 4.2: Size dependence of the plasmonic response.

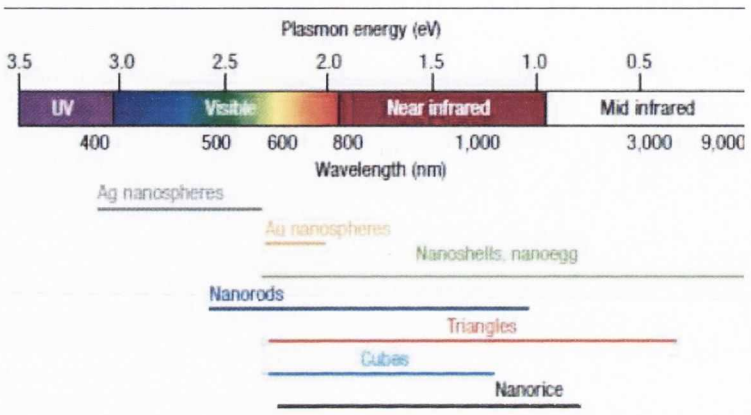

Figure 4.3: Shape dependence of the plasmonic response.

Size effects have been extensively studied [5]. The increase in size causes the appearance of higher multipolar interactions besides the usual dipolar resonance because the field is not uniform across the nanoparticle. The red shift associated with the increasing size was explained in terms of retardation effects and contributions from multipolar terms [10]. The dependence of the bandwith on the size is usually illustrated by identifying two different size domains. For particles larger than 20-25nm the bandwidth increases with the size and this is attributed to retardation effects and inhomogeneous polarization of the nanoparticles. When the particles are smaller the ratio between the surface area and the volume becomes important and a 1/r (r is the particle radius) dependence of the bandwidth is observed [11].

Drastic effects occur on the surface plasmon absorption when the nanoparticle shape is changed. If the shape is non-spherical the dipolar resonance splits into two or more non-degenerate plasmon modes that differ by their oscillation direction [12]. This makes nanoparticle plasmons tunable to an extent

by changing the nanoparticle features. Many other different shapes have been investigated both experimentally and theoretically [13]. In the latter case only spherical particles can have an exact solution while for any other case the complexity of the situation requires the use of different numerical methods in order to simulate the optical response [5].

In addiction to these effects, usually investigated on non-interacting particles, collective effects have to be considered when particles get close enough to each other [14]. In this case a redshift of the peak is observed and assigned to the cooperative electromagnetic interaction between the nanoparticles [15]. If additional order is introduced in the nanostructure a blueshift can appear due to the unfavorable interaction among the particles when they are illuminated with perpendicularly polarized light [16]. In this case it is harder to assign the optical response to intimate properties of the nanoparticles (shape, size etc.) since they are masked by the collective effects.

The tunability of the plasmon resonance has been widely demonstrated in relation to the dielectric environment. The dielectric material induces a screening of the charges that lower the plasmon excitation energy red-shifting the resonance peak [17, 18, 19].

Thus the optical spectra originate from a large variety of physical and chemical effects generating great interest but the experimental investigations are performed on cluster ensembles that are inhomogeneous with respect to shape, size etc. These tend to mask the properties of individual clusters and make it difficult to compare theory and results. SPPs are typically supported by silver and gold but are also observed on Cu, Ti and Cr [5].

4.2 Electromagnetism in metals

Metals show a strong frequency dependence of the optical response which can be described via a complex dielectric function $\varepsilon(\omega)$. In the low-frequency regime, up to the visible region of the spectrum, metals are highly reflective and allow only a negligible fraction of the electromagnetic wave to penetrate into their surface. In the near-infrared and visible region of the spectrum the penetration increases with an increased dissipation. Finally at ultraviolet frequencies electromagnetic waves propagate through the metal and the degree of attenuation depends on the electronic band structure: alkali metals have ultraviolet transparency due to their almost free-electron-like response while noble metals show a strong absorption due to transitions between electronic bands [5, 20].

The interaction of metals with electromagnetic fields can be understood in a framework based on Maxwell's equations which link the electric field $\mathbf{E}$, the magnetic field $\mathbf{H}$, the magnetic induction $\mathbf{B}$ and the dielectric displacement $\mathbf{D}$ with the external charge ρ and current density $\mathbf{J_{ext}}$ [1]:

$$\nabla \cdot \mathbf{D} = \rho_{ext} \tag{4.1}$$

$$\nabla \cdot \mathbf{B} = 0 \tag{4.2}$$

$$\nabla \times \mathbf{E} = -\frac{\delta \mathbf{B}}{\delta t} \tag{4.3}$$

$$\nabla \times \mathbf{H} = \mathbf{J_{ext}} + \frac{\delta \mathbf{D}}{\delta t} \tag{4.4}$$

The external electric field causes the alignment of microscopic dipoles and the electric dipole moment per unit volume inside the material is described by the polarization $\mathbf{P}$ with:

$$\mathbf{D} = \varepsilon_0 \mathbf{E} + \mathbf{P} \tag{4.5}$$

where $\varepsilon_0 \approx 8.854 \times 10^{-12} F/m$ is the electric permittivity of vacuum. For linear, isotropic and nonmagnetic media it can be written:

$$\mathbf{D} = \varepsilon_0 \varepsilon \mathbf{E} \tag{4.6}$$

and using the dielectric susceptibility χ:

$$\mathbf{P} = \varepsilon_0 \chi \mathbf{E} \tag{4.7}$$

which also yields $\varepsilon = 1 + \chi$. In general the dielectric function $\varepsilon(\omega) = \varepsilon_1(\omega) + i\varepsilon_2(\omega)$ is a complex function of the frequency linked to the complex refractive index $n(\omega) = n(\omega) + ik(\omega)$ of the medium through $n = \sqrt{\varepsilon}$ where k is the extinction coefficient and determines the optical absorption of the electromagnetic waves.

4.2.1 Drude-Lorentz model

A neutral gas of ions and electrons is called a *plasma* [1, 5]. Over a wide frequency range, the electrons of a metal behave like a plasma and can be

considered as essentially free electrons in the presence of periodic distributions of positive core atoms and this allows us to treat metals as plasmas. The electromagnetic field of an incoming light wave can induce polarization of the conduction electrons, i.e. the electrons are displaced with respect to the heavier positive core ions which in turn pull them back generating oscillations. Plasma oscillations (also called Langmuir waves or plasma waves) are periodic and coherent oscillations of charge density in conducting media (plasma or metals) and the quasi-particle resulting from the quantization of these oscillations is called a plasmon. They are damped via collisions occurring at a characteristic collision frequency $\Gamma = 1/\tau$, with τ the relaxation time of the free electron gas.

The linear response to electromagnetic waves is described by the dielectric function $\varepsilon(\omega) = \varepsilon_1(\omega) + i\varepsilon_2(\omega)$ which for free electron metals like the alkalis is mainly governed by transitions within the conduction band while for other metals substantial contributions due to interband transitions from lower to conduction bands and from conduction to higher unoccupied bands are present. The optical properties and the dielectric function can be approached by applying the Drude-Lorentz-Sommerfeld model, which combines the Drude model for free electron conductivity with the Lorentz model for dipole oscillators [5, 20, 21]. When an AC field is applied it generates an electron oscillatory motion and the displacement of an electron of mass m_e is described by superimposing the field drifted motion on the field-free case [11]:

$$m_e \frac{\delta^2 \mathbf{r}}{\delta t^2} + m_e \Gamma \frac{\delta \mathbf{r}}{\delta t} = e\mathbf{E}_0 e^{-i\omega t} \tag{4.8}$$

where Γ is a phenomenological damping constant.

The displaced electrons contribute to the macroscopic polarization $\mathbf{P}$ given by:

$$\mathbf{P} = -\frac{ne^2}{m_e(\omega^2 + i\Gamma\omega)}\mathbf{E} \tag{4.9}$$

In a system of n free electrons per unit volume, the dielectric function results to be:

$$\varepsilon(\omega) = 1 - \frac{ne^2}{\varepsilon_0 m_e}\frac{1}{\omega^2 + i\Gamma\omega} \tag{4.10}$$

where n is the electron density, ε_0 is the permittivity of free space, m_e the electron mass, ω the frequency of light. Fig.4.4 shows real and imaginary part of the dielectric function for silver metal.

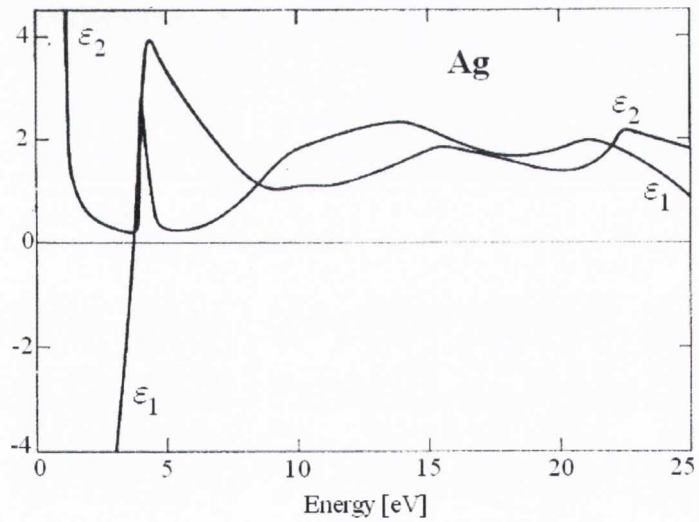

Figure 4.4: Real (ε_1) and imaginary (ε_2) dielectric functions for bulk solid silver (after[22])

By introducing the effective mass m_{eff} instead of the electron mass m_e of the conduction electrons the coupling of the electrons to the ion core can be described. Eq. 4.10 can be rewritten in the following form [11, 23]:

$$\varepsilon(\omega) = 1 - \frac{{\omega_p}^2}{\omega^2 + i\Gamma\omega} = 1 - \frac{{\omega_p}^2}{\omega^2 + \Gamma^2} + i\frac{{\omega_p}^2\Gamma}{\omega(\omega^2 + \Gamma^2)} \tag{4.11}$$

where

$$\omega_p = \frac{ne^2}{\varepsilon_0 m_e} \tag{4.12}$$

is known as the plasma frequency [11, 20]. For $\omega \gg \Gamma$ the dielectric function is predominantly real and it can be approximated to:

$$\varepsilon_1(\omega) \approx 1 - \frac{\omega_p^2}{\omega^2} \tag{4.13}$$

The behavior of noble metals in this region is altered by interband transitions, leading to an increase in the imaginary part of the dielectric function.

The complex refractive index of the metal is related to the complex dielectric constant by:

$$\tilde{n} = \sqrt{\varepsilon} \tag{4.14}$$

with $\varepsilon_1 = n^2 - k^2$ and $\varepsilon_2 = 2nk$.

So when the light frequency is below the plasma frequency the refractive index is imaginary, goes to zero when $\omega = \omega_p$ and becomes positive for higher frequencies. This in turn means that the reflectivity, calculated by the formula:

$$R = \left|\frac{\tilde{n} - 1}{\tilde{n} + 1}\right|^2 = \frac{(n-1)^2 + k^2}{(n+1)^2 + k^2} \tag{4.15}$$

is unity for frequencies lower than the plasma frequency and then decreases after $\omega = \omega_p$ approaching zero at infinity [20]. Metals usually have very large values of electron densities that lead to plasma frequencies in the ultraviolet region [24]. This explains the first property of metals, namely they are good reflectors at visible frequencies; a metal does not transmit light with frequencies below the volume plasmon frequency but becomes transparent for higher frequency radiation. Light of frequency below the plasma frequency is reflected because the electrons in the metal screen the electric field of the light while light of frequency above the plasma frequency is transmitted because the electrons cannot respond fast enough to screen it [20, 25]. This model describes quite well the situation but some discrepancies come out in the experimental results. In the free-electron model the dielectric functions tend to unity as the frequency is much higher than the plasmon frequency (eq.4.13) but for noble metals such as gold and silver, which play an important role in plasmonics, the model has to be modified since the d band close to the Fermi surface causes a highly polarized environment [1, 11]. This can be described by introducing the dielectric constant ε_∞:

$$\varepsilon(\omega) = \varepsilon_\infty - \frac{\omega_p^2}{\omega^2 + i\Gamma\omega} \tag{4.16}$$

the validity of the free-electron model breaks down at visible frequencies due to the presence of interband transitions.

Depending on the dimensionality of the metal body, different modes of plasmonic oscillations are possible. Volume plasmons are collective bulk excitations of valence electrons generated by high energy and fast electrons in

three-dimensional bodies. Surface plasmons are density oscillations confined to the surface or interfaces such as metal-dielectric interfaces and have a huge role in the increased interest towards this field. Finally nanoparticle plasmon resonances, also called Localized surface plasmonic resonances (LSPR), manifest in the optical spectra of metallic nanoparticles and their importance is constantly increasing in the field of plasmonics [26]. We will mainly focus on the latter type of plasmons.

4.3 SPPs at metal/dielectric interfaces

Coherent electron oscillations can be excited at flat interfaces such as metallic thin films [11]. A surface mode of plasmons is allowed by Maxwell's equations at the interface between a metal and a dielectric which can sustain a trapped SPPs in the form of coherent longitudinal charge oscillations of the conduction electrons, creating confined surface waves. These electromagnetic excitations propagating at the interface between a dielectric and a conductor are called surface plasmon polaritons and are essentially two-dimensional waves confined evanescently in the perpendicular direction to the interface traveling along the surface and decaying exponentially into both media. The field perpendicular to the surface decays exponentially with distance from the surface and it is said to be evanescent or near-field. It is a consequence of the bound, non-radiative nature of SPPs which prevents power from propagating away from the surface [1]. The interaction between the surface charge density and the electromagnetic field results in the momentum of the SP mode, $\hbar k_{SP}$, being

greater than that of a free space photon of the same frequency, $\hbar k_0$ ($k_0 = \omega/c$ is the free-space wavevector). Applying Maxwell's equations to the interface between a conductor and a dielectric allows the investigation of the physical properties of such systems [1]. A central relation is the dispersion relation of SPPs propagating at the interface given by:

$$\beta = k_0 c \sqrt{\frac{\varepsilon_{met}\varepsilon_{diel}}{\varepsilon_{met} + \varepsilon_{diel}}} \tag{4.17}$$

where β is the propagation constant of the traveling wave and corresponds to the component of the wave vector in the direction of propagation, ε_{met} and ε_{diel} are the dielectric functions of the two layers, respectively conductor and insulator.

The real part ε'_{met} is negative for visible light and in order for β to be real, the requirement for a propagating mode, is that $|\varepsilon_{met}| > \varepsilon_{diel}$.

Due to the fact that ε_{met} is frequency dependent the dispersion relation is not a straight line and the dispersion relation for SPPs always lies to the right of the respective light line (Fig.4.5).

The denominator in (4.17) can become very small (but not zero due to the finite imaginary part) and the condition $-\varepsilon'_{met} = \varepsilon_{diel}$ marks a resonance that occurs at a frequency to which the dispersion relation converges at large $k_{\|}$. The dispersion of the light in a dielectric medium is given by [1]:

$$\omega_{light} = \frac{c}{\sqrt{\varepsilon_{diel}}} \cdot k_{light} = \frac{c}{\sqrt{\varepsilon_{diel}} \cdot \sin\vartheta} \cdot k_{\|light} \tag{4.18}$$

Both dispersion relations do not intersect for any chosen angle θ with the

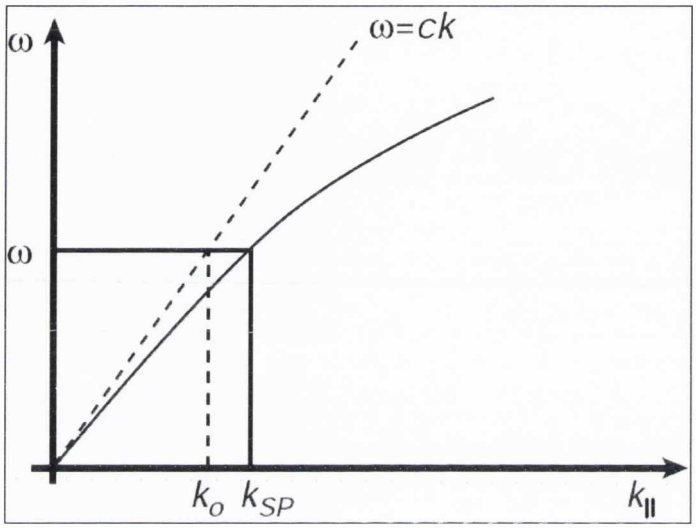

Figure 4.5: Dispersion relation for a surface plasmon (black solid line) and for a photon (dashed line).

consequence that SPPs on a flat metal/dielectric interface cannot be excited directly by light impinging from the side of the dielectric because of momentum mismatch. The propagation constant β is actually greater than the wave vector of the light k on the dielectric side of the interface and its projection along the interface k_x=k·sinθ is always smaller than β even at grazing incidence. The momentum mismatch (for example for Ag-air in the red part of the visible spectrum $k_{SP} \cong 1.03k_0$) is due to the binding of the SPPs to the surface and must be bridged if light is to be used to generate SPPs (Fig.4.6) [1].

Different techniques are adopted to supply the missing momentum. In the so-called attenuated total internal reflection, phase-matching can be achieved in a three-layer system with the metal inserted between two insulators, one layer being air for simplicity. The light is shone not from the side of the

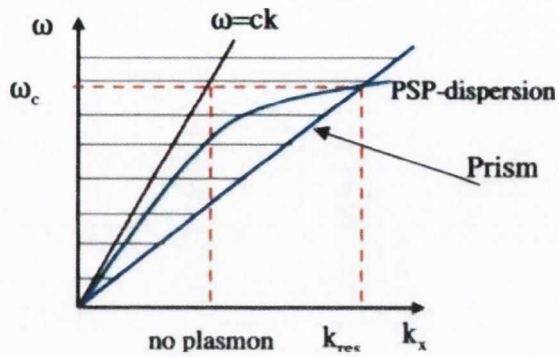

Figure 4.6: Prism coupling and SPP dispersion.

dielectric but from the rear side through the metal, requiring that the thickness of the film be in the range of the penetration depth of light into the metal (around tens of nm, depending on the metal) [20, 27]. The high dielectric constant insulator is usually a prism and a beam passing through it will have a momentum $k_x = k\sqrt{\varepsilon}\sin\theta$ sufficient to excite the SPPs at the metal/air interface. The excitation is visible through a minimum in the reflected intensity. The metal film is deposited onto a glass substrate with refractive index larger than the refractive index of the dielectric on top of the metal. Then $n_{glass} = \sqrt{\varepsilon_{glass}} > \sqrt{\varepsilon_{diel}} = n_{diel}$. This determines that light impinging at a certain angle ϑ with frequency ω_ϑ corresponding to the frequency where the SPR dispersion relations intersects will penetrate the metallic film exciting the surface plasmon modes on the upper metal-dielectric interface. The reflected light of frequency ω_ϑ will have reduced intensity because some incident power is used to excite the SPR at ω_ϑ.

Light of different frequencies but same angle is not able to excite the SPRs because the dispersion relations do not coincide for $\omega \neq \omega_\vartheta$ and therefore light

with $\omega \neq \omega_\vartheta$ will be reflected completely. Shining white light will therefore show a spectrum with an absorption peak at $\omega = \omega_\vartheta$ [1]. For this technique two different geometries are commonly used. In the Kretschmann method the thin film is deposited on top of the prism (Fig.4.7) while in the Otto configuration the prism is separated from the film by a thin air gap.

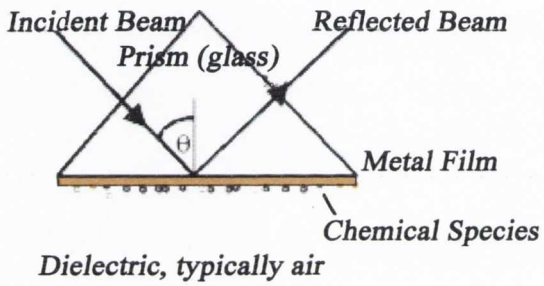

Figure 4.7: Kretschmann configuration.

Momentum mismatch can be overcome also by patterning the metal with a shallow grating of holes, using a microscope objective of high numerical aperture, or by near-field excitation using a small fiber probe [1].

4.4 Nanoparticle plasmons and Localized plasmon resonance

As previously discussed, SPPs are propagating, dispersive electromagnetic waves coupled to the electron plasma of a conductor at a dielectric interface. On the other hand, localized surface plasmons are non-propagating excitations of the conduction electrons in metals coupled to the electromagnetic field. Due

to the particle shape, the curved surface produces a restoring force on the electrons producing a resonance called a localized surface plasmon. Also the curved surface allows one to excite the plasmon by direct light illumination with no need of phase-matching techniques [1].

4.4.1 Optical properties of single metal nanoparticles

The strong interaction between light and nanoscale particles has been known for hundreds of years. Metal nanoparticles were used for the staining of glass windows and ceramic pottery as in the famous Lycurgus cup dating back to the 4th century A.D., in the Byzantine empire (Fig.4.8). This glass cup is on display in the British Museum and shows a red color when viewed in transmitted light while it appears green in reflection. The reason for this is the presence of Au nanoparticles embedded in the glass which show a strong optical absorption in the visible light.

Metal nanoparticles, especially for noble metals like Au, Ag and Cu, show very different optical response compared to bulk or thin films. Nanoparticles of noble metals show a strong absorption peak in the UV-Vis region that are not present in the bulk metal [4, 14, 19, 28, 29, 30, 31, 32, 33, 34, 35, 36]. Whereas films absorb light throughout the near-infrared and visible regions due to free-electron absorption, for nanoparticle this process is quenched for energies lower than the resonance peak (the dipolar surface-plasmon particle resonance). For higher energies, films and particles show a similar behaviour due to the dominance of *d-sp* electronic interband transitions which are prominent for Au and Cu in the vicinity of the dipole resonance peak, but less for

Figure 4.8: The Lycurgus glass cup appears green in reflected light and red in transmitted light due to dispersed gold nanocrystals.

Ag [1, 5, 20].

The resonant electromagnetic behaviour of metallic nanoparticles is due to the confinement of the electrons in a small volume. The nanoparticles are so small that the light can easily penetrate through them and grasp at all conduction band electrons moving them all in phase and leading to a buildup of polarization charges on the particle surface. When the electrons are displaced with respect to the positive ions, a Coulomb restoring force pulls them back allowing for the resonance to occur at a specific frequency where the electron response shows a $\pi/2$ phase lag with respect to the driving field; if the electrons are cold, the charge density oscillates at the plasma frequency given by Eq.4.12

[5, 33].

The plasmon energy is estimated in the free electron model as:

$$E_p = \hbar\sqrt{\frac{Ne^2}{m_e\varepsilon_0}} \tag{4.19}$$

The resulting electric dipole on the particle represents a restoring force and the nanoparticle can be considered as a harmonic oscillator driven by a light wave and damped by ohmic losses (production of heat) and radiative losses (scattering). The latter is equivalent to the re-emission of a photon at the expense of a nanoparticle plasmon (NPP) excitation. Only light with a wavelength in resonance with an eigenmode of the NPP oscillation is able to excite NPPRs. Therefore a NPPR manifests itself in two different ways in the optical spectra: first there is an extinction band in the extinction spectrum and second there is a substantial amount of scattered light, at least for larger particles; both effects can be used for detection. For larger particles, the spectral response is also modified due to retardation effects and excitation of higher order multipoles [5, 20].

4.4.2 Mie Theory and the quasistatic approximation

In general, spectral position, damping and dipole strength depend on several factors such as material [1, 19], size [5, 10, 37], shape [13, 33, 38, 39, 40, 41] and dielectric environment [17, 18, 19, 42, 43]. In order to construct a theoretical interpretation, particle shapes are approximated via spheres or spheroids for which analytical and exact solutions exist. Provided that the size r of the particles is much smaller than the wavelength of light, a quasi-static approach

can be used where the phase of the harmonically oscillating field is considered constant over the particle volume. Neglecting spatial retardation effects over the particle volume allows one to represent the particle as an ideal dipole. The harmonic time dependence is added to the solution when the field distributions are known. For a spherical particle of radius r$\ll \lambda$ in a non-adsorbing surrounding of dielectric constant ε_m the quasi-static particle polarizability α is [5]:

$$\alpha = 4\pi r^3 \frac{\varepsilon - \varepsilon_m}{\varepsilon_m + 2\varepsilon_m} \tag{4.20}$$

where ε is the frequency dependent dielectric response of the metal. The polarizability and thus the polarization inside the particle is resonantly enhanced when the denominator shows a minimum such as $\varepsilon = -2\varepsilon_m$, considering small Im[$\varepsilon$]. This relationship is called the "Frölich condition" and the associated mode is the dipole surface plasmon [44]. Increasing the medium dielectric constants produces a redshift of the peak due to the formation of polarization charges on the dielectric side of the interface weakening the total restoring force. The magnitude of the polarizability is limited by the incomplete vanishing of the denominator because the imaginary part of the dielectric constant is non-zero.

For ellipsoidal particles it is necessary to introduce a geometrical factor L_i [5]:

$$\alpha = \frac{4}{3}\pi abc \frac{\varepsilon - \varepsilon_m}{\varepsilon_m + L_i(\varepsilon - \varepsilon_m)} \tag{4.21}$$

and $\Sigma L_i = 1$. Spheroids are an important class of ellipsoids. From eq.4.21 spheroids show two separated plasmon resonances corresponding to oscillations of the electrons along the two different axes [45]. Larger particles show a red-shift and broadening of the peak due to retardation effects and the electrons do not move in phase anymore. Also radiative losses become dominant, damping the plasmons for particles larger than 100nm [5].

Since exact analytical solutions are not available for arbitrary shapes and sizes, numerical methods are often used to calculate the resonance frequencies and the field enhancement of particles with complicated shapes. T-matrix [46], discrete dipole approximation (DDA) [41, 47, 48] and finite-difference time-domain (FDTD) [45] simulations are the most used methods.

When the particle size is large the quasi-static approach is not valid anymore and a rigorous electrodynamic approach is required. Gustav Mie's paper on optical properties of metal nanoparticles represents a milestone in the history of optics and it is one of the most frequently cited paper in physics over the last decades [49]. Mie's theory has found wide applicability and has been successful in explaining optical absorption spectra of metal nanoparticles [5, 19, 50, 51, 52, 53]. In 1908 Mie solved the Maxwell's equations for an incoming plane wave interacting with a spherical particle developing a full theory of scattering and absorption of a spherical particle. For very small particles with a diameter d$\ll \lambda$ (where λ is the wavelength of light in the surrounding medium), only the first term of the expansion, the dipolar term, can be considered and corresponds to the quasi-static or Rayleigh limit.

In this approximation the scattering, extinction and absorption cross sec-

tions of a spherical nanoparticle are given by:

$$\sigma_{sca} = \frac{3}{2\pi}\left(\frac{\omega}{c}\right)^4 \varepsilon_{diel}^2 V^2 \frac{(\varepsilon_{met}^{'} - \varepsilon_{diel})^2 + (\varepsilon_{met}^{''})^2}{(\varepsilon_{met}^{'} + 2\varepsilon_{diel})^2 + (\varepsilon_{met}^{''})^2} \tag{4.22}$$

$$\sigma_{ext} = 9\frac{\omega}{c}(\varepsilon_{diel})^{3/2} V \frac{\varepsilon_{met}^{''}}{(\varepsilon_{met}^{'} + 2\varepsilon_{diel})^2 + (\varepsilon_{met}^{''})^2} \tag{4.23}$$

$$\sigma_{abs} = \sigma_{ext} - \sigma_{sca} \tag{4.24}$$

where ω is the light frequency, c is the speed of light in vacuum, V is the particle volume, ε_{diel} is the purely real dielectric constant of the surrounding medium and $\varepsilon_{met} = \varepsilon_{met}^{'} + i\varepsilon_{met}^{''}$ is the metallic nanoparticle dielectric constant. The denominators in the fractions of the equations can have a minimum if $\varepsilon_{met}^{'} + 2\varepsilon_{diel} = 0$ because the real part of the dielectric constant of the metal is negative in the visible range [1, 5]. In the limit of very small nanoparticles the spectral position of the resonance is independent of the shape of the nanoparticles because no geometric factors occur in the denominator apart from the volume which determines the magnitude of scattering and absorption cross sections but not the spectral position. Furthermore the volume enters quadratically in the scattering cross section equation but only linearly in the extinction cross section, which is the sum of absorption and scattering cross sections. For very small nanoparticles, below 20 nm, most of the light is absorbed and scattering is hard to see. If the nanoparticle size increases too much, the scattered spectrum becomes very broad [54, 55].

4.4.3 Interacting nanoparticles ensembles and arrays

Advances in particle synthesis have allowed for the production of ordered arrays of interacting nanoparticles that behave as an ensemble of electric dipoles interacting with each other [14, 16, 34, 56, 57]. Two different types of interaction can be identified depending on the distance d between the particles. For spacings of the order of the exciting wavelength far-field dipolar interactions, which show a d^{-1} dependence, are dominant. Variation of spectral position and bandwidth have been reported and attributed to the far-field dipolar interaction with increased plasmon damping for changes of grating order from evanescent to radiative [58]. When the particles are much closer to each other, $d \ll \lambda$, near-field dipolar interactions with a distance dependence of d^{-3}, dominate and lead to a polarization dependent splitting of the plasmon peak. This phenomenon, red- and blue-shift of the peak respectively for longitudinal and transversal light polarization with respect to the arrays, is due to Coulombic interactions between the charged particles [16, 59].

4.5 Applications

4.5.1 Detection and sensing

With regards to the biosensors field, there is increasing interest in the commercialization of optical biosensor systems [60, 61, 62, 63]. Surface plasmon resonance holds the potential for application in many important areas including medicine, environmental monitoring, biotechnology, drug and food monitoring [63, 64, 65, 66, 67]. Currently SPR devices compete with other types of biosen-

sors. The major competitors are immunoassays, commonly used in low cost tests due to their high specificity and sensitivity. The most popular detection scheme is based on the excitation of propagating plasmons in metallic thin films on a transparent substrate. Commercial instruments are available from Biacore and Texas Instruments (Fig.4.9) [68, 69].

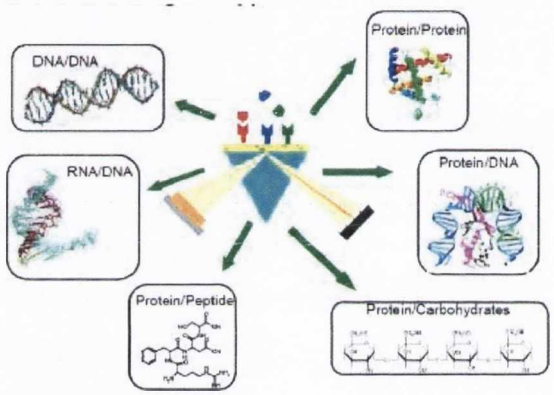

Figure 4.9: Biodetection by plasmon resonance.

As well as thin films, nanoparticle colloids have been explored for optical sensing in two different configurations. The first configuration involves individual nanoparticles: any variation of the refractive index of the surface layer will cause a change in the optical response. Based on this mechanism nanoparticles suspended in solution or supported on substrates have been investigated for label-free optical sensing [70, 71]. In the second detection mode the redshift following the coupling of aggregated nanoparticles was used to qualitatively detect DNA. The surface of gold and silver nanoparticles can be bioconjugated to several binding groups such as oligonucleotides, proteins and other biologically relevant molecules. This leads to the synthesis of nanoparticles

probes that can support biomolecular assays with numerous advantages over the conventional methods such as low cost and high sensitivity. It is believed that bioconjugated nanoparticles will be the centerpiece for several detection strategies [61].

Nowadays, the state-of-the art technique to determine parameters like kinetic rate constants, affinity, binding position, thermodynamic parameters etc. in biological systems relies on optically excited SPR sensors [72, 73, 74]. In fact, the SPR method is a mature biophysical technique; ever since the commercial introduction of SPR sensors in the 1990s, they belong to the standard instruments in research and industry [68]. SPR sensors possess detection limits which are low enough for a wide range of applications and are used for different biological molecules, e.g. proteins, oligonucleotides, oligosaccharides, lipids, small molecules, viral particles, cells as well as in different experimental contexts e.g. proteomics, genomics, drug discovery, and membrane studies [75]. One advantage of this method is its high sensitivity, enabling it to detect molecules at low concentrations, to monitor binding of small molecules, to measure weak binding constants, to analyse the kinetic off-rates of extremely strong interactions etc. [76]. The actual sensitivity corresponds to a detection limit of a few pg/mm^2. This level of sensitivity for a realtime, label-free optical biosensor system is still unmatched.

While there is theoretically no limit to their application, the need to improve SPR based sensors will drive research to focus primarily on some physical aspects. First, the decrease of the detection limits in order to increase the sensitivity. Furthermore, the application of SPR sensors to complex samples

such as blood needs systems that allow one to resolve the sensor response from non-specific background effects. This issue highlights the necessity of having a matrix where the plasmon resonance offers a clear and intense optical response in the form of well defined peak intensities and shifts. It is believed that SPR sensor technology will benefit from the use of optical waveguide technology which offers the potential for developing miniaturized sensing elements [1].

4.5.2 Biotechnology applications

The most recognizable effect of surface plasmon resonance is the pronounced absorption of light by small metal particles. Nanostructured materials, and particularly gold and silver nanoparticles, possess optical properties far superior to the molecular species such as organic chromophores. They offer scattering or absorbance cross sections up to 5-6 orders of magnitude higher, optical activity over more biocompatible wavelength regimes, and substantially greater chemical stability or stability against photobleaching [63]. These advantages make of them the ideal candidates to replace the typical chromophores and to be investigated as therapeutic agents for photothermal treatment and optical imaging of tumors [77, 78].

4.5.3 Enhancement of light transmission

Most of the research related to plasmon resonance focuses on subwavelength photonic devices [1, 2, 26]. The development of new patterning techniques allows one to study the science behind the SPP phenomenon and it has already led to experimental demonstrations of theoretical concepts. In relation

to photonics applications it is crucial to obtain a better understanding of the relationship between surface morphology and the activity of surface plasmons, about which much is still obscure. Investigations in this field are essentially based on using photon scanning tunneling microscopy (PSTM) to map the fields on the metal surface because the traditional far field techniques do not offer adequate response considering the subwavelength size of the structures and fields involved [79]. PSTM is essential for the development of waveguides and other components and it has recently been used to illustrate a new approach to guide light using linear arrays of metal nanoparticles [80]. One of the remaining major issues is how SPP beams can be focused. For plasmonics to be successful, scientists need to increase the propagation lengths of the plasmon waves. Propagation lengths must be improved in order to transport energy for longer distances than the few hundreds of nanometers reached nowadays. This requires a better control of the energy loss in the propagation, loss essentially due either to light absorption or to coupling with radiation [26]. Furthermore researchers need to tailor structures in such a way that they can launch and guide and focus SPP when and how desired. Chains of nanoparticles seem to be very promising in relation to the transfer of electromagnetic energy from one end of the chain to the other. In this direction much work is required in order to optimize the photon energy transport and localization as well as to engineer the plasmon coupling and interference between several resonant plasmonic particles [81].

4.5.4 Nanoscale waveguiding

One of the most attractive aspects of SPPs is the way they concentrate and channel the light using subwavelength structures [26]. This could lead to miniaturized photonic circuits with length scales smaller than those achieved nowadays. Such a circuit would first convert light into SPPs, which would then propagate and be processed by logic elements before being converted back into light (Fig.4.10).

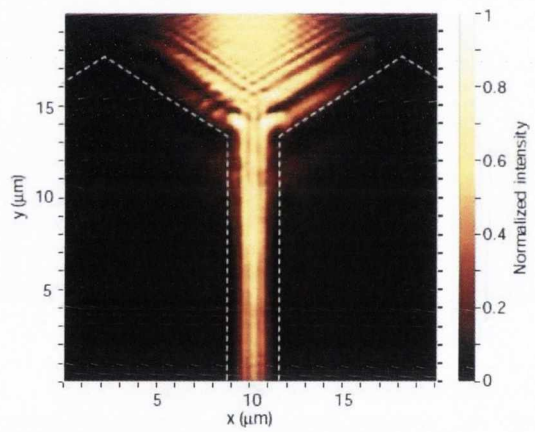

Figure 4.10: Light propagation in a plasmonic waveguide ([2]).

An appealing feature is that, when embedded in dielectric materials, the circuitry used to propagate the SPPs can also be used to carry electric signals (this is the base of a new branch of photonics, called plasmonics [1, 8]). Waveguides can be made of aligned metal nanoparticles. Photonic devices possess higher processing speed compared to actual electronic devices but their size is much larger due to the fact that the signal is transmitted in dielectric waveguides which cannot be smaller than half the wavelength because of the

diffraction limit. Overcoming this limit could lead to miniaturization of photonics circuits opening to a new generation of devices. Plasmonics is seen as very promising in this direction since it is thought to embody the strongest points of both optical and electronic data transfer (Fig.4.11).

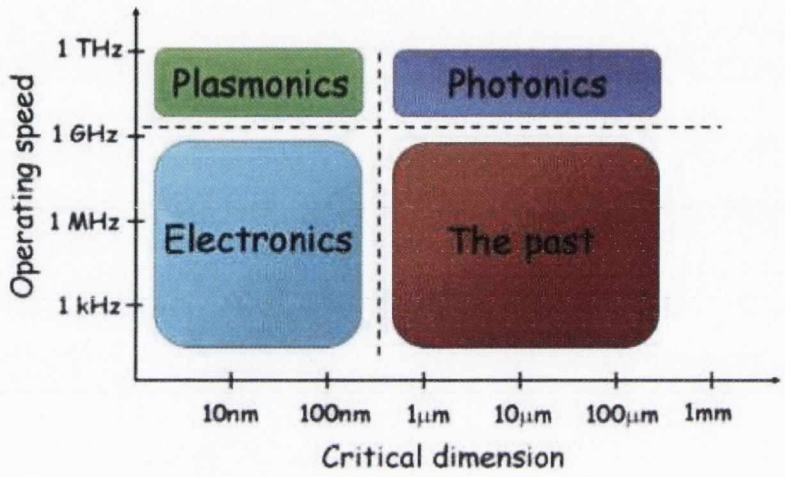

Figure 4.11: Plasmonics could lead to a whole new generation of photonics devices combining the strongest points of optical and electronic data transfer.

Plasmon waveguides utilize propagating subwavelength waves and their size is much smaller compared to normal dielectric waveguides. However, their propagation is too short so far. It has been suggested that electromagnetic energy can be guided below the diffraction limit along chains of closely spaced metal nanoparticles that convert the optical mode into non-radiating surface plasmons. Linear arrays of gold or silver nanoparticles can channel the electromagnetic energy over distances of a few hundreds of nanometers [80]. The main requirement is that the particles are very close to each other in order to enable the coupling between SPR modes. It is estimated that for visible

and near-infrared wavelengths propagation distances on the centimeter scale can be reached, leading to the realization of chip-scale integrated photonics and nanoscale all-optical networks [1]. Various components will be required to realize these circuits such as waveguides, switches, couplers etc. SPR coupling promises to become as important as p-n junctions in the new nanoscale photonics.

A number of fabrication methods are explored to produce plasmonic waveguides. E-beam writing can routinely generate ordered arrays of metallic nanoparticles but turning this technique into a fast and low cost fabrication method is out of reach. In contrast self-assembly provides appealing features in this sense. Recent developments in self-assembly techniques offer the promise of being able to easily produce photonic band gap (PBG) substrates to act as substrates on top of which the photonic circuits can be realized [2].

The attractive properties of SPPs have a major drawback: the high SPPs damping, due to ohmic losses in the metal, restricts the SPPs propagation lengths in the visible and near-infrared spectral range to about 10-100 μm.

4.5.5 Enhancement of electromagnetic fields

Scattering and absorption of light are not the only distinctive features for metal nanostructures. Concentrating light leads to an electric field enhancement that can be used to manipulate light-matter interactions and boost non-linear phenomena: for example, silver and gold nanoparticles show a substantial enhancement of local electromagnetic fields [63, 26]. The electric field of the plasmons can amplify the Raman signals of chemical species near the metal

surface leading to a new field known as surface-enhanced spectroscopy and a typical example is the surface-enhanced Raman scattering (SERS) [82]. The highest enhancements reported are of the order of 10^{14} [83], although it is believed that this increase comes from two separate mechanisms: electromagnetic enhancement and chemical enhancement [84]. When the incident light is in resonance with the SP modes of a metallic thin film or nanoparticles a local electromagnetic field enhancement occurs up to a factor of 1000 leading to a Raman enhancement of 10^{12}. Gold and silver nanoparticles with controllable shapes are excellent candidates for this application. Chemical enhancement is related to chemical interactions like charge transfer that may occur between adsorbed molecules and the surface and accounts for an additional factor of 100 in the total enhancement. Reproducible control of the degree of enhancement has been difficult and a precise control of the surface roughness allows one to better control the Raman enhancement due to the plasmon resonance. Patterned Ag substrates were used to detect an anthrax biomarker by SERS [85]. This method promises to detect very small amounts of spores down to four times lower than the infectious dose. As well as SERS, surface-enhanced fluorescence was reported on near metallic nanoparticles [86].

4.5.6 Photonic Band Gap (PBG) materials

One of the most important advances in photonics over the last decades has been that of photonic band gap (PBG) materials. PBG use wavelength-scale periodic structures to manipulate the interaction between light and matter so as to build new photonic structures (such as photonic crystal fibre) [2, 87].

They have been developed on periodically structured insulators and semiconductors but by exploiting SPPs metals also can be used as PBG materials, in the form of photonic surfaces [88].

The nature of SPPs changes when they propagate on metal surfaces that are periodically textured on the scale of the wavelength of light. When the period of the nanostructure is half that of the effective wavelength of the SP mode, scattering may lead to the formation of SP standing waves and the opening of an SP stop band [89]. When a surface is modulated in both in-plane directions SPPs modes may be prevented from travelling in any in-plane direction leading to full PBG for SPPs modes [88, 90]. Recent developments in the fabrication of nanostructures via self-assembly offer the prospect to easily produce SP-PBG substrates to act as photonic substrates on which to define photonic circuits. At frequencies within the bandgap, the density of SPPs modes is zero, no SPPs modes can be supported. However at band edges the SP mode dispersion is flat and the associated density of SP mode is high, corresponding to a high field enhancement close to the metal surface. Flat bands are also associated with the localized SP modes of metallic nanoparticles [5]. The frequency and width of these modes are determined by the particle's shape, material, size and environment [5, 91, 92], and for this reason they are being pursued as tags for biosensing [93] and as substrates for SERS [94] and potentially as aerials for fluorophores [95]. The interaction between two or more nanoparticles can lead to further levels of field enhancement with even more dramatic effects associated with hot spots in random structures [16, 96, 97].

4.5.7 Other applications

Interest in surface plasmons resonance covers many other fields such as microscopy [98], magneto-optic data storage [99] and clean energies [100]. For instance, plasmon resonance on silver nanoparticles was recently investigated as a means of improving the efficiency of silicon-based solar cells [101, 102]. Efficiency problems in organic light-emitting diodes could be overcome using periodic nanostructures in order to produce long life and high-efficiency devices [103].

4.5.8 Mapping surface plasmons

The properties of SPPs devices are linked to the activity and distribution of SPPs on the metal surface. Much is still not known about the relationship between surface topology and SPPs modes. Because of their confinement to the surface far field techniques are not reliable and near-field techniques, such as photon scanning tunneling spectroscopy (PSTM), are employed to map the fields on the metal surface like those of the SPPs waveguides [104, 105, 106]. PSTM is a collection mode scanning near-field optical microscope where the sample lies on a glass prism, which enables one to shine the light in total internal reflection [26]. The nanometre tip frustrates the total internal reflection when scanning close to the surface and thereby maps the near-field intensities [107, 108]. PSTM has been essential in the development of SPPs devices such as waveguides and other components [106].

References

[1] S.A. Maier. *Plasmonics.* Springer, Berlin, (2007).

[2] W.L. Barnes, A. Dereux, and T.W. Ebbesen. *Nature*, 424:824, (2003).

[3] J. Henzie, J. Lee, and M.H. Lee. *Ann.Rev.Phys.Chem.*, 60:147, (2009).

[4] E. Hutter and J.H. Fendler. *Adv.Mater.*, 16:1685, (2004).

[5] U. Kreibig and M. Vollmer. *Optical Properties of Metal Particles.* Springer, Berlin, (1995).

[6] B. Sepulveda, P.C. Angelome, L.M. Lechuga, and L.M. Liz-Marzan. *Nano Today*, 4:244, (2009).

[7] N.I. Cade, T. Ritman-Meer, K.A. Kwakwa, and D. Richards. *Nanotechnology*, 20:285201, (2009).

[8] S.A Maier, M.L. Brongersma, P.G. Kik, S. Meltzer, A.A.G. Requicha, and H.A. Atwater. *Adv. Mater.*, 13:1501, (2001).

[9] B.N. Khlebtsov and N.G. Khlebtsov. *J.Phys.Chem.C*, 111:11516, (2007).

[10] S. Berciaud, L. Cognet, P. Tamarat, and B. Lounis. *Nano Lett.*, 3:515, (2005).

[11] U. Kreibig and M. Volmer. *Optical Properties of Metal Clusters.* Springer, Berlin, 1995.

[12] Y.Y. Yu, S.S. Chang, C.L. Lee, and C.R.C. Wang. *J.Phys.Chem.B*, 34:6661, (1997).

[13] J.J. Mock, M. Barbic, D.R. Smith, and S. Schultz. *J.Chem.Phys.*, 116:6755, (2002).

[14] T. Atay, J.H. Song, and A.V. Nurmikko. *Nano Letters*, 4:1627, (2004).

[15] Z. Liu, H. Wang, H. Li, and X. Wang. *Appl.Phys.Lett.*, 72:1823, (1998).

[16] W. Rechberger, A. Hohenau, A. Leiner, J.R. Krenn, B. Lamprecht, and F.R. Ausseneg. *Opt.Comm.*, 220:137, (2003).

[17] G. Xu, M. Tazawa, P. Jin, S. Nakao, and K. Yoshimura. *Appl.Phys.Lett.*, 82:3811, (2003).

[18] J. Muller, C. Sonnichsen, H. von Poschinger, G. von Plessen, T.A. Klar, and J. Feldmann. *Appl.Phys.Lett.*, 81:171, (2002).

[19] P. Mulvaney. *Langmuir*, 12:788, (1996).

[20] M. Fox. *Optical properties of solids.* Oxford University Press, Oxford, (2001).

[21] P. Drude. *Ann.Phys.*, 1:566, (1900).

[22] H. Ehrenreich and H.R. Philipp. *Phys.Rev.*, 128:1622, (1958).

[23] E. Hecht. *Optics.* Pearson Education, UK, (2006).

[24] R.W.G. Wyckoff. *Crystal structures.* Interscience, New York, (1971).

[25] C. Kittel. *Introduction to solid state physics.* Wiley, New York, (1996).

[26] V.M. Shalaev and S. Kawata. *Nanophotonics with Surface Plasmons.* Elsevier, Oxford, UK, (2007).

[27] D. Griffiths. *Introduction to Electrodynamics.* Prentice Hall, New Jersey, (1999).

[28] Y. Xia, J.A. Rogers, K.E. Paul, and G.M. Whitesides. *Chem.Rev.*, 99:1823, 1999.

[29] B. Choi, H. Lee, S. Jin, S. Chun, and S. Kim. *Nanotech.*, 18:075706, (2007).

[30] J. Gonzalo, R. Serna, J. Solis, D. Babonneau, and C.N. Afonso. *J.Phys.: Condens.Matter*, 15:S3001, (2003).

[31] C. Sonnichsen, T. Franzl, T. Wilk, G. von Plessen, and J. Feldmann. *New J. of Phys.*, 4:931, (2002).

[32] A. Tao, P. Sinsermsuksakul, and P. Yang. *Nature*, 2:435, (2007).

[33] S. Link and M.A. El-Sayed. *J.Phys.Chem.B*, 103:8410, (1999).

[34] B.M. Reinhard, M. Siu, H. Agarwal, and A.P. Alivisatos. *Nano Letters*, 5:2246, (2005).

[35] S. Camelio, D. Babonneau, D. Lantia, and L. Simonot. *Europhy.Lett*, 79:47002, (2007).

[36] S. Eustis and M. El-Sayed. *Chem.Soc.Rev.*, 35:209, (2006).

[37] U Kreibig and U. Genzel. *Surf.Sci.*, 156:678, (1985).

[38] W. Gotschy, K. Vonmetz, A. Leitner, and F.R. Aussenegg. *Opt.Lett.*, 21:1099, (1996).

[39] K.L. Kelly, E. Coronado, L.L. Zhao, and G.C. Schatz. *J.Phys, Chem.B*, 107:668, (2003).

[40] R.C. Jin, Y.W. Cao, C.A. Mirkin, K.L. Kelly, G.C. Schatz, and J.G. Zheng. *Science*, 294:1901, (2001).

[41] I.O. Sosa, C. Noguez, and R.G. Barrera. *J.Phys.Chem.B*, 107:6269, (2003).

[42] A. Hilger, M. Tenfelde, and U. Kreibig. *Appl.Phys.B*, 73:361, (2001).

[43] P.A. Kossyrev, S.G. Yin, A. Cloutier, D. A. Cardimona, D. Huang, P.M. Alsing, and J.M. Xu. *Nano Lett.*, 5:1978, (2005).

[44] B.W. Van Der Meer, G. Coker III, and S.Y. Simon Chen. *Resonance Energy Transfer. Theory and Data.* Wiley, New York, (1994).

[45] J. Grand, P.M. Adam, A.S. Grimault, A. Vial, J.L. Lamy de la Chapelle, M. Bijeon, S. Kostcheev, and P. Royer. *Plasmonics*, 1:135, (2006).

[46] D.W. Mackowski and M.I. Mishchenko. *J.Opt.Soc.Am.A*, 13:2266, (1996).

[47] B.T. Draine and P.J. Flatau. *J.Opt.Soc.Am.A*, 11:1491, (1994).

[48] E. Hao, G. Schatz, and J. Hupp. *J.Fluoresc.*, 14:331, (2004).

[49] G. Mie. *Ann.Phys.*, 25:377, (1908).

[50] G.C. Papavassiliou. *Prog.Solid State Chem.*, 12:185, (1980).

[51] M. Kerker. *The scattering of light and other electromagentic radiation.* Academic Press, New York, (1969).

[52] C.F. Bohren and D.R. Huffman. *Absorption and scattering of light by small particles.* Wiley, New York, (1983).

[53] J.A. Creighton and D.G. Eadon. *J.chem.Soc.,Faraday Trans.*, 87:3881, (1991).

[54] C. Sonnichsen, T. Franzl, T. Wilk, G. von Plessen, J. Feldmann, O. Wilson, and P. Mulvaney. *Phys.Rev.Lett.*, 88:077402, (2002).

[55] A. Wokaun, J.P. Gordon, and P.F. Liao. *Phys.Rev.Lett.*, 48:957, (1982).

[56] Y. Lu, G.L. Liu, and L.P. Lee. *Nano Letters*, 5:5, (2005).

[57] R. elghanian, J.J. Storhoff, R.C. Mucis, R.L. Resringer, and C.A. Mirkin. *Science*, 277:1078, (1997).

[58] B. Lamprecht, A. Leitner, and F.R. Aussenegg. *Appl.Phys.B*, 64:269, (1997).

[59] S.A Maier, P.G. Kik, and H.A. Atwater. *Appl.Phys.Lett.*, 81:1714, (2002).

[60] P. Kvasnicka and J. Homola. *Biointerphases*, 3:FD4, (2009).

[61] J. Homola, S.S. Yee, and J. Gauglitz. *Sensors and Actuators B - Chemical*, 54:3, (1999).

[62] J. Homola, I. Koudela, and S.S. Yee. *Sensors and Actuators B - Chemical*, 54:16, (1999).

[63] R.B.M. Schasfoort and A.J. Tudos. *Handbook of Surface Plasmon Resonance.* Royal Society of Chemistry, Cambridge, UK, (2008).

[64] E. Boisselier and D. Astruc. *Chem.Soc.Rev.*, 38:1759, (2009).

[65] C. Wang and J. Irudayaraj. *Small*, 4:2204, (2008).

[66] V. Hodnik and G. Anderluh. *Sensors*, 9:1339, (2009).

[67] M. Rajarajan, T. Dar, C. Themistos, B.M.A. Rahman, K.T.V. Grattan, J. Homola, and J. Irudayaraj. *J.Modern Opt.*, 56:564, (2009).

[68] www.biacore.com.

[69] www.ti.com.

[70] N. Nath and A. Chilkoti. *Anal.Chem.*, 74:504, (2002).

[71] Y. Sun and Y. Xia. *Anal.Chem.*, 74:5297, (2002).

[72] B. Liedberg, C. Nylander, and I. Lundstrom. *Sensors and Actuators*, 4:299, (1983).

[73] M. Malmqvist and R. Karlsson. *Curr.Opin.Chem.Biol.*, 9:378, (1997).

[74] R. Karlsson, A. Michaelsson, and L. Mattson. *J.Immunol.Methods*, 145:229, (1991).

[75] R. Karlsson. *J.Mol.Recognit.*, 17:151, (2004).

[76] P.O. Markgren, M. Hamalainen, and U.H. Danielson. *Anal.Biochem.*, 279:71, (2000).

[77] C. Loo, A. Lowery, N. Halas, J. West, and R. Drezek. *Nano Lett.*, 5:709, (2005).

[78] L. Hirsch, R. Stafford, J. Bankson, S. Sershen, B. Rivera, R. Price, J. Hazle, N. Halas, and J. West. *Proc.Natl.Acad.Sci. USA*, 100:13549, (2003).

[79] J.C. Weeber, Y. Lacroute, and A. Dereux. *Phys.Rev.B*, 68:115401, (2003).

[80] S.A Maier, P.G. Kik, H.A. Atwater, S. Melyzer, Harel E., B. Koel, and A.A.G. Requicha. *Nature Mater.*, 2:229, (2003).

[81] R. de Waele, A.F. Koenderink, and A. Polman. *Nano Lett.*, 7:070807, (2007).

[82] K. Kneipp, H. Kneipp, I. Itzkan, R.R. Dasari, and M.S. Feld. *Chem.Rev.*, 99:2957, (1999).

[83] K. Kneipp, Y. Wang, H. Kneipp, L.T. Perelman, I. Itxkan, R.R. Dasari, and M.S. Feld. *Phys.Rev.Lett.*, 78:1667, (1997).

[84] M.M. Dvoynenko and J.K. Wang. *Opt.Lett.*, 32:3552, (2007).

[85] X. Zhang, M.A. Young, O. Lyandres, and R.P. Van Duyne. *J.Am.Chem.Soc.*, 127:4484, (2005).

[86] A. Parfenov, I. Gryczynski, J. Malicka, C.D. Geddes, and J.R. Lakowicz. *J.Phys.Chem.B*, 107:8829, (2003).

[87] R.F. Cregan, B.J. Mangan, J.C. Knight, T.A. Birks, P.S. Russell, P.J. Roberts, and D.C. Allan. *Science*, 285:1537, (1999).

[88] S.C. Kitson, W.L. Barnes, and J.R. Sambles. *Phys.Rev.Lett.*, 77:2670, (1996).

[89] W.L. Barnes, T.W. Preist, S.C. Kitson, and J.R. Sambles. *Phys.Rev.B*, 54:6227, (1996).

[90] W.L. Barnes, S.C. Kitson, T.W: Preist, and J.R. Sambles. *J.Opt.Soc.Am.*, 14:1654, (1997).

[91] C.L. Haynes and R.P. Van Duyne. *J.Phys.Chem.B*, 105:5599, (2001).

[92] C. Sonnichsen. *Appl.Phys.Lett.*, 77:2949, (2000).

[93] D.A. Schultz. *Curr.Opin.Biotechnol.*, 14:13, (2003).

[94] N. Felidj, J. Aubard, G. Levi, J.R. Krenn, A. Hohenau, G. Schider, A. Leitner, and F.R. Aussenegg. *Appl.Phys.Lett.*, 82:3095, (2003).

[95] S.A. Levi, A. Mourran, J.P. Spatz, F.C.J.M. van Veggel, D.N. Reinhoudt, and M. Moller. *Chem.A Eur.J.*, 8:3808, (2002).

[96] J.P. Kottmann and O.J.F. Martin. *Opt.Lett.*, 26:1096, (2001).

[97] F.J. Garcia-Vidal and J.B. Pendry. *Phys.Rev.Lett.*, 77:1163, (1996).

[98] I.I. Smolyaninov, J. Elliott, A.V. Zayats, and C.C. Davis. *Phys.Rev.Lett.*, 94:057401, (2005).

[99] C.C. Smolyaninonv II, Davis, V.N. Smolyaninova, D. Schaefer, J. Elliott, and A.V. Zayats. *Phys.Rev.B*, 71:035425, (2005).

[100] P.V. Kamat. *J.Phys.Chem.C*, 111:2834, (2007).

[101] S. Pillai, K.R. Catchpole, T. Trupke, and M.A. Green. *J.Appl.Phys.*, 101:093105, (2007).

[102] D. Derkacs, S.H. Lim, P. Matheu, W. Mar, and E.T. Yu. *Appl.Phys.Lett.*, 89:093103, (2006).

[103] P.A. Hobson, S. Wedge, J.A.E. Wasey, I. Sage, and W.L. Barnes. *Adv.Mat.*, 14:1393, (2002).

[104] B. Hecht, H. Bielefeldt, L. Novotny, Y. Inouye, and D.W. Pohl. *Phys.Rev.Lett*, 77:1889, (1996).

[105] J.C. Weeber, E. Bourillot, A. Dereux, J.P. Goudonnet, Y. Chen, and C. Girard. *Phys.Rev.Lett.*, 77:5332, (1996).

[106] Dereux A. Weeber J.C. Bourillot E. Lacroute Y. Goudonnet J.P. Schider G. Gotschy W. Leitner A. Aussenegg F.R. Girard C. Krenn, J.R. *Phys.Rev.Lett.*, 82:2590, (1999).

[107] M.Y. Mahmoud, G. Bassou, Z. Chekroun, and N. Djamai. *Mater.Sci.Eng.B:Solid State Mater.Adv.Tech.*, 142:37, (2007).

[108] M. Salerno, N. Felidj, J.R. Krenn, A. Leitner, and F.R. Aussenegg. *Phys.Rev.B*, 63:165422, (2001).

"≪ Guai a voi, anime prave!
Non isperate mai veder lo cielo:
i' vegno per menarvi a l'altra riva
ne le tenebre etterne, in caldo e 'n gelo.
E tu che se' costì, anima viva,
pàrtiti da cotesti che son morti≫.
Ma poi che vide ch'io non mi partiva,
disse: ≪Per altra via, per altri porti
verrai a piaggia, non qui, per passare:
più lieve legno convien che ti porti≫.
E 'l duca lui: ≪Caron, non ti crucciare:
vuolsi così colà dove si puote
ciò che si vuole, e più non dimandare≫."

D.Alighieri

(La Divina Commedia, Inferno III, 84-96)

Part II

Experimental Results and Discussion

Chapter 5

Instrumentation and Experimental Details

"Sir, you are drunk."
"And you, madam, are ugly.
But in the morning, I shall be sober."
W. Churchill

The Atomic Terrace Low Angle Shadowing (ATLAS) instrument has been designed and developed entirely in our laboratory. The idea of such a device has matured following the need to create a particular MBE system able to deposit a highly collimated flux onto a substrate at shallow angle.
In general, MBE involves the generation of fluxes of constituent matrix (molec-

ular beam) and their reaction at the substrate to form an ordered overlayer (epitaxy). Elemental or compound constituents are heated (if in the liquid or solid state) or introduced (if gaseous) to cause mass transfer from the flux generators to the substrate, via the vapor phase. To maintain the high purity and integrity of the deposit, stringent vacuum conditions are needed. The fluxes of constituents can be modulated either by altering the evaporation conditions, or by physically interrupting the beam.

Due to the shallow angle design, the main capability of the ATLAS device is the possibility to deposit nanowires of any evaporable material on a wide range of substrates, restricted only by the requirement that the latter forms ordered atomic or bunched terraces. As discussed, this property will be used to grow arrays of nanowires on vicinal substrates in a wide variety of different configurations [1].

Two separate systems have been designed and built. The first one is a prototype, or first generation instrument, used mainly to test the validity of the technique but which now actually works as a full time growth chamber. The second one is a more sophisticated and upgraded (second generation) instrument with more capabilities in terms of angle, temperature and deposition parameter control. A detailed description is reported in [2].

5.1 The Instrumentation - The first generation system: ATLASα

There are a series of key features that has to be considered in the design process associated with the MBE technology. First of all there are vacuum requirements which are essential to the technique. Also several MBE components have to be counted in such as sources, shutters, substrate heating and manipulation etc. In parallel, diagnostic and analytical tools are needed for the growth and post-growth analysis.

The first ATLAS system (ATLASα) built incorporates evaporation, substrate holder, thickness and pressure monitor equipment into a single stand-alone vacuum chamber. In particular, the system consists of a 6" diameter spherical stainless steel deposition chamber connected to a turbomolecular pump (Osaka TG550, pumping speed of 550 l/s) via a DN150 CF elbow, which maintains the chamber at pressures in the low 10^{-7}Torr. Turbomolecular pumps provide a fast and effective method for system pump-down. All the flanges use flat copper gaskets as a seal, into which knife-edges on the flanges bite (also known as Conflat seals).

There is no in-situ sample manipulation or loadlock, so that the chamber must be vented every time a new sample is loaded or removed. Aside from limiting throughput of samples, the air exposure of the system between each deposition run can compromise the material quality because system venting contaminates the sources. Also this implies that before a new deposition is carried out, a thorough outgassing of the sources procedure is needed, stretching out the

experimental time. A surface exposed to air accumulates several monolayers of chemisorbed and physisorbed gases which slowly de-gas, precluding rapid pump-down of the vacuum system. Several hours, or even days, may be necessary to achieve pressures below 10^{-7} mbar (depending on exposure history). Therefore, the ATLAS system has to be routinely baked after each air exposure to temperatures of about 250°C. Baking the system accelerates the desorption helping to reduce residual gases and provides near UHV conditions (10^{-8}Torr range). A two-stage rotary vane pump is used as a backing pump for the turbo. The top flange of the chamber is equipped with a quartz crystal monitor in order to check the deposition flux during the experiment. The pressure is monitored using a wide-range Bayard-Alpert ion gauge mounted on a DN38 CF side port. Transparent viewports allow for sample observation inside the chamber during the loading and deposition processes. On the bottom of the growth chamber a DN64 flange is connected via a set of extension tubes to a 10cc capacity high-temperature effusion cell. The distance between the source and the centre of the chamber, where the sample is placed, is approximately one meter so that the beam reaching the substrate surface is highly collimated. A shutter is mounted between the source and the growth chamber. When mounted, the sample sits in the center of the growth chamber on a DN63 CF flange, directly above the effusion cell. The usual sample size mounted on the holder is $1cm^2$ but bigger (or smaller) samples can be loaded with a suitable adapter. This system is pictured in Fig.5.1.

During the assembling phase, extensive care was exercised in handling the vacuum components to avoid contamination from oil, grease, or by human

contact.

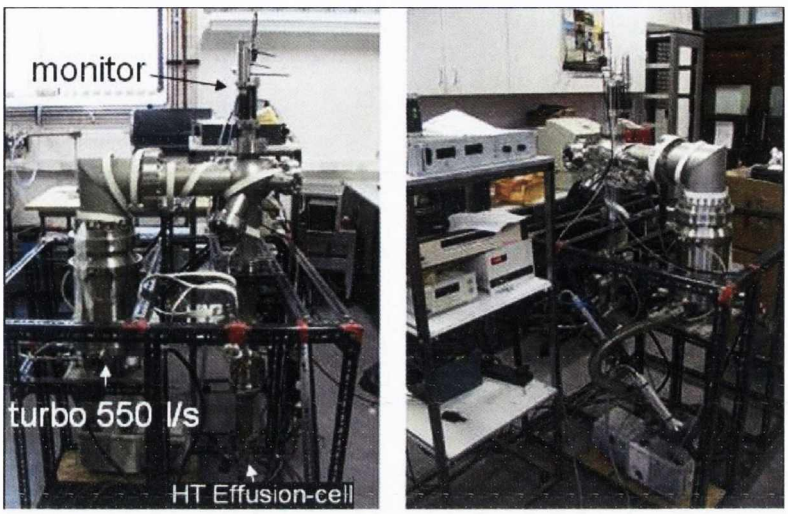

Figure 5.1: Pictures of the first generation ATLAS instrument: ATLASα.

5.2 The Instrumentation - The second generation system: ATLASβ

In the design of ATLASβ several implementations have been integrated to offer a higher level of accuracy and more flexibility. This chamber will be reserved for studies on semiconductor substrates.

The building of a UHV system requires employing suitable constructional materials and methods in order to avoid or minimize poor vacuum integrity due to leaks. Both ATLAS systems are made of stainless steel which nowadays is the most common material for UHV systems due to the capability of standing large stresses on chamber walls created by the pressure differential. Stainless

steel 304 minimizes chromium diffusion at welds.

The system, schematically shown and pictured in Fig.5.2 comprises a 8" diameter cylindrical stainless steel UHV deposition chamber which is kept under ultra-high vacuum conditions at all times by a 240 l/s starcell triode ion pump. Just like for the previous system, access into the chamber is facilitated by removable flanges (usually up to 300 mm port size) which use Conflat seals. Chamber and pump are interconnected by valves which permit isolation of the various sections of the system.

The deposition chamber is fitted with a 6" spherical fast-entry loadlock (FEL) for introduction of substrates into, and removal of processed samples from, the deposition region. The loadlock is pumped by a 260 l/s turbomolecular pump backed by an oil-free diaphragm pump and baking the system results in a base pressure in the 10^{-10}Torr range. A valve between the FEL and deposition chamber ensures high vacuum integrity in the deposition region while the FEL is vented to air. The presence of a FEL chamber greatly reduces the number of bakeout procedures required compared to the prototype system. Also, in addition to dramatically enhancing throughput and the convenience of system operation, the use of a FEL improves the material quality. The substrate manipulator, source cells and materials can be held under vacuum for extended time periods leading to thorough outgassing. Substrates are no longer subjected to extended bake-out periods, since they are introduced into the clean deposition area as required.

The transfer of the sample from the load lock into the main chamber is performed by using a magnetically coupled linear shift mechanism system. Sample

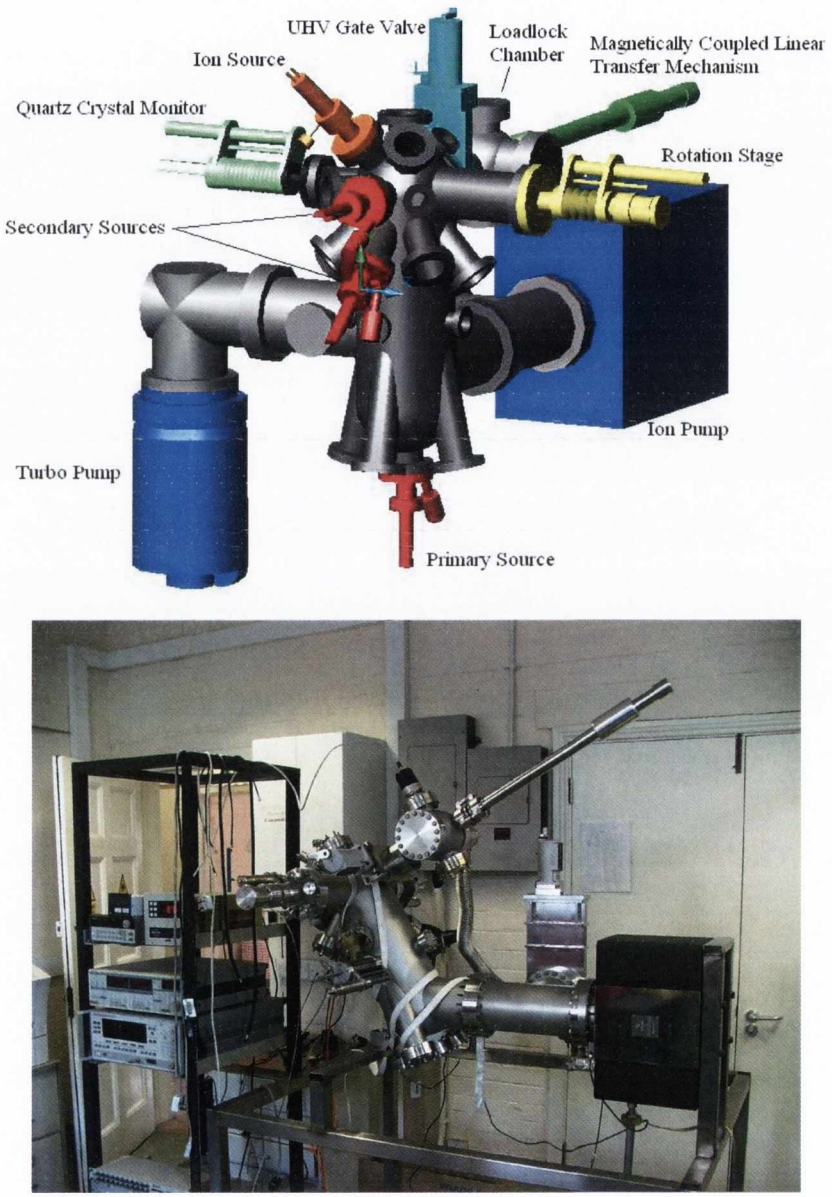

Figure 5.2: Schematic 3D representation (top) and photography (bottom) of the ATLASβ system.

pass off is achieved by means of a spring loaded transfer fork and docking stage. The springs on the docking stage also double as terminals to drive current for either direct or resistive heating of the sample. The sample is mounted at the main focal point of the chamber and can be tilted through 200° with a precision of 0.5°. This allows for both sample transfer and alignment relative to the primary and secondary sources. The deposition chamber is tilted by 30° off normal to allow one to maximize the full capacity of secondary effusion cells mounted at the front of the chamber. These latter sources are used to form capping layers on top of the nanowire arrays produced using the primary source. The primary source is either a 10 cc high-temperature effusion cell or an electron beam evaporator both from MBE-Komponenten. The effusion cell is used to evaporate metals while the e-beam evaporator together with a P-doping source is used to grow Si nanowires. The docking stage is mounted on a rotary drive mechanism to allow the sample to be aligned with respect to either the primary or the secondary sources. In the case of the primary source, the sample is aligned almost parallel to the flux direction, while for secondary sources it is aligned normal to the flux direction. Both the primary and secondary sources have their own dedicated quartz crystal monitors.

An Ar^+ cold cathode ion source is also mounted on a CF114 (DN63, 4.5in) and oriented toward the sample for in situ cleaning of the substrates prior to the film deposition process. Initially three effusion cells, loaded with different materials, will be mounted on CF114 (DN63, 4.5in) as secondary sources. Additional ports are provided for future upgrades of the system.

During the assembling the vacuum components were handled with care to

avoid contamination. During the leak testing phase, all ports were fitted with blank flanges with the exception of ion gauges. The system was baked several times at 250°C in order to achieve satisfactory UHV conditions. The procedure was repeated after loading the components along with the outgassing of the effusion cell (with and without crucible) until acceptable vacuum conditions were achieved.

5.3 Atomic Force Microscopy (AFM)

Atomic Force Microscopy (AFM) provides a powerful technique to study the surface morphology and its evolution upon annealing [3, 4, 5, 6, 7, 8, 9, 10, 11]. The Atomic Force Microscope was developed to overcome a basic drawback with the Scanneling Tunneling Microscope (STM): with STM one can investigate only conductive or conductive-coated samples. This disadvantage was overcomed with the invention of atomic force microscope by Binnig, Quate, and Gerber [12, 13]. Under the interaction with a sample surface macroscopic cantilever provided with sharp tip can be bended by atomic forces to sufficiently large amount to be measured by the common facilities, e.g. laser deflection. Their original AFM consisted of a diamond shard attached to a strip of gold foil [12]. Detection of the cantilevers vertical movement was done with a second tip: an STM placed above the cantilever. Today, most AFMs use a laser beam deflection system, introduced by Meyer and Amer, where a laser is reflected from the back of the reflective AFM lever and onto a position-sensitive detector, preferably a bicell (Fig.5.3) [14, 15, 16]. The output of the bicell is provided to a computer for processing of the data for providing a topographical

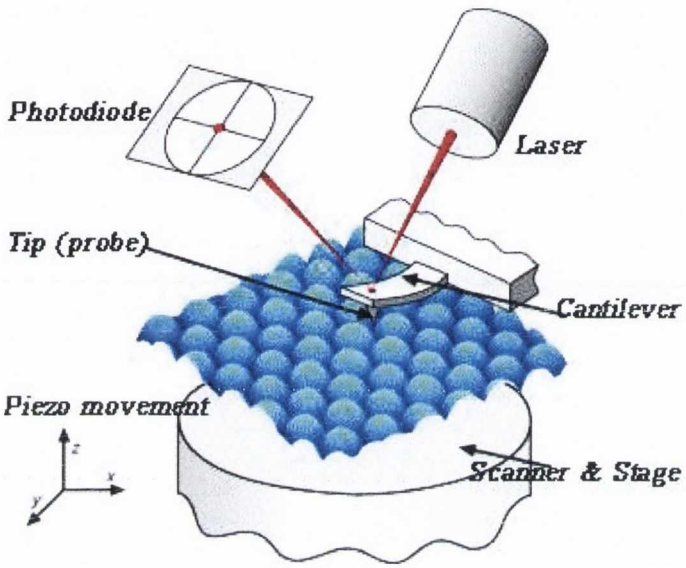

Figure 5.3: Schematic illustration of AFM. The tip is attached to a cantilever, and is raster-scanned over a surface. The cantilever deflection due to tip-surface interactions is monitored by a photodiode sensitive to laser light reflected from the backside of the cantilever.

image of the surface. AFM tips and cantilevers are microfabricated from Si or Si_3N_4. Typical tip radii are of the order of a few to tens of nm [17, 18].

The principles on how the AFM works are very simple [17]. An atomically sharp tip is scanned over a surface with feedback mechanisms that enable the piezo-electric scanners to maintain the tip at a constant force (to obtain height information), or height (to obtain force information) above the sample surface. As the tip scans the surface of the sample, moving up and down with the contour of the surface, the laser beam is deflected off the attached cantilever into a dual element photodiode. The photodetector measures the difference in light intensities between the upper and lower photodetectors, and then converts them to a voltage. Feedback from the photodiode difference sig-

nal, through software control from the computer, enables the tip to maintain either a constant force or constant height above the sample. In the constant force mode the piezo-electric transducer monitors real time height deviation. In the constant height mode the deflection force on the sample is recorded. The latter mode of operation requires calibration parameters of the scanning tip to be inserted in the sensitivity of the AFM head during force calibration of the microscope [17].

AFM is being used to solve processing and materials problems in a wide range of technologies affecting the electronics, telecommunications, biological, chemical, automotive, aerospace, and energy industries. The materials being investigating include thin and thick film coatings, ceramics, composites, glasses, synthetic and biological membranes, metals, polymers, and semiconductors. AFM is being applied to studies of phenomena such as abrasion, adhesion, cleaning, corrosion, etching, friction, lubrication, plating, and polishing. By using AFM one can not only image the surface in atomic resolution but also measure the force at nano-newton scale [17, 19, 20, 21, 22].

All the AFM images presented in this work were obtained with a NT-MDT Solver Pro scanning probe microscope [23].

5.3.1 Scanning modes

According to the interaction of the tip and the sample surface, the AFM can be classified as repulsive or Contact mode and attractive or Noncontact mode. Tapping mode is a third possible scanning mode [17, 23].

Contact Mode The contact mode where the tip scans the sample in close contact with the surface is the common mode used in the force microscope [12, 13, 24, 25]. In the contact mode of operation the cantilever deflection under scanning is sensed and compared to some desired value of deflection to generate an image of the sample surface profile. If the measured deflection is different from the desired value the feedback amplifier applies a voltage to the piezo to raise or lower the sample relative to the cantilever to restore the desired value of deflection. The voltage that the feedback amplifier applies to the piezo is a measure of the height of features on the sample surface. It is displayed as a function of the lateral position of the sample. A few instruments operate in UHV but the majority operate in ambient atmosphere, or in liquids. In idealized experimental conditions (e.g. in ultrahigh vacuum) when the cantilever tip approaches the sample surface long-range Van der Waals forces start acting upon it at a distance of a few tens of angstroms. When the tip-sample separation is reduced to a distance of several angstroms repulsive forces become dominant. Under ambient conditions, practically always some humidity is presented in air and a water layer is adsorbed on the sample and tip surfaces. When the cantilever approaches the sample surface capillary forces hold the tip in contact with the surface and increases the minimum achievable interaction force.

Problems with contact mode are caused by excessive tracking forces applied by the probe to the sample. The effects can be reduced by minimizing the tracking force of the probe on the sample, but there are practical limits to the magnitude of the force that can be controlled by the user during operation in

ambient environments [17].

Simultaneously with topography acquisition under scanning one can imagine some other characteristics of the investigated sample. If the cantilever and tip are conductive one can image the spreading resistance of the sample. If scanning is carried out in the direction perpendicular to the longitudinal axis of cantilever (lateral direction) the friction force causes cantilever twisting. By measuring this twisting using a position-sensitive four-sectional detector one can image, simultaneously with topography, the friction force distribution throughout sample surface [26].

Non-contact Mode The non-contact mode is used in situations where tip contact might alter the sample in subtle ways [27, 28, 29]. In this mode the tip hovers 50 - 150 $\mathring{A}$ above the sample surface. Attractive Van der Waals forces acting between the tip and the sample are detected, and topographic images are constructed by scanning the tip above the surface. Since the attractive forces from the sample are substantially weaker than the forces used by contact mode, the tip must be given a small oscillation so that AC detection methods can be used to detect the small forces. The change in amplitude, phase, or frequency of the oscillating cantilever is then measured in response to force gradients from the sample. For highest resolution, it is necessary to measure force gradients from Van der Waals forces which may extend only a nanometer from the sample surface. In general, the fluid contaminant layer is substantially thicker than the range of the Van der Waals force gradient and therefore, attempts to image the true surface with non-contact AFM fail as the oscillating probe becomes trapped in the fluid layer or hovers beyond the

effective range of the forces it attempts to measure [17].

Tapping Mode Tapping mode is a powerful technique which overcomes problems associated with friction, adhesion, electrostatic forces, and other difficulties associated with conventional AFM scanning methods [30, 31]. This is done by alternately placing the tip in contact with the surface to provide high resolution and then lifting the tip off the surface to avoid dragging it across the surface [32, 33, 34]. Tapping mode imaging is implemented in ambient air by oscillating the cantilever assembly at or near the cantilever's resonant frequency using a piezoelectric crystal. The piezo motion causes the cantilever to oscillate with a high amplitude (typically greater than 20nm) when the tip is not in contact with the surface. The oscillating tip is then moved toward the surface until it begins to tap the surface. During scanning, the vertically oscillating tip alternately contacts the surface and lifts off. The intermittent contact with the surface reduces the cantilever oscillation due to energy loss caused by the tip contacting the surface. The reduction in oscillation amplitude is used to identify and measure surface features. The cantilever oscillation amplitude is maintained constant by a feedback loop. Selection of the optimal oscillation frequency is software-assisted and the force on the sample is automatically set and maintained at the lowest possible level. When the tip passes over a bump on the surface, the cantilever has less room to oscillate and the amplitude of oscillation decreases. Conversely, when the tip passes over a depression, the cantilever has more room to oscillate and the amplitude increases (approaching the maximum free air amplitude). The digital feedback loop then adjusts the tip-sample separation to maintain a constant amplitude

and force on the sample.

Tapping Mode inherently prevents the tip from sticking to the surface and causing damage during scanning. Unlike contact and non-contact modes, when the tip contacts the surface, it has sufficient oscillation amplitude to overcome the tip-sample adhesion forces. Also, the surface material is not pulled sideways by shear forces since the applied force is always vertical. Another advantage of the Tapping Mode technique is its large, linear operating range. This makes the vertical feedback system highly stable, allowing routine reproducible sample measurements [17, 35].

5.3.2 Phase Imaging: Beyond Topography

Phase Imaging is a powerful feature that provides nanometer-scale information about surface structure often not revealed by other SPM techniques [17, 30, 31]. By mapping the phase of the cantilever oscillation during the tapping mode scan, phase imaging is able to detect variations in composition, adhesion, friction, viscoelasticity etc. Applications include identification of contaminants, mapping of different components in composite materials, and differentiating regions of high and low surface adhesion or hardness [36, 37, 38]. In many cases, phase imaging complements lateral force microscopy (LFM) and force modulation techniques, often providing additional information more rapidly and with higher resolution.

5.4 Ultraviolet-Visible (UV-VIS) Spectroscopy

Ultraviolet-visible spectroscopy is the measurement of the wavelength and intensity of absorption of near-ultraviolet and visible light by a sample in the UV-visible, adjacent near-ultraviolet (UV) and near-infrared (NIR) ranges. Ultraviolet and visible light are energetic enough to promote outer electrons to higher energy levels. UV-VIS spectroscopy is usually applied to molecules and inorganic ions or complexes in solution that undergo electronic transitions. This technique is complementary to fluorescence spectroscopy, in that fluorescence deals with transitions from the excited state to the ground state, while absorption measures transitions from the ground state to the excited state. The concentration of an analyte in solution can be determined by measuring the absorbance at some wavelength and applying the Beer-Lambert Law which states that the absorbance of a solution is directly proportional to the solution's concentration:

$$A = -log_{10}\frac{I}{I_0} = \epsilon cL \tag{5.1}$$

where A is the measured absorbance, I is the transmitted intensity, I_0 is the intensity of the incident light at a given wavelength, L the pathlength through the sample, and c the concentration of the absorbing species. For each species and wavelength, ϵ is a constant known as the molar absorptivity or extinction coefficient. The absorbance and extinction ϵ are sometimes defined in terms of the natural logarithm instead of the base-10 logarithm.

5.4.1 The UV-VIS spectrophotometer

The instrument used in ultraviolet-visible spectroscopy is called a UV-VIS spectrophotometer (Fig.5.4) [39]. It measures the intensity of light passing through a sample (I), and compares it to the intensity of light before it passes through the sample (I_o). The ratio I/I_0 is called the transmittance, and is usually expressed as a percentage. The absorbance, A, is based on the transmittance: A = - log(%T).

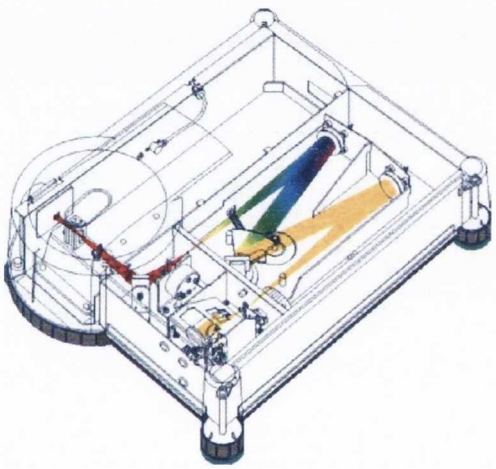

Figure 5.4: Schematic illustration of UV-VIS spectrophotometer.

The basic parts of a spectrophotometer are a light source (often an incandescent bulb for the visible wavelengths, or a deuterium arc lamp in the ultraviolet), a holder for the sample, a diffraction grating or monochromator to separate the different wavelengths of light, and a detector, typically a photodiode or a CCD [39]. A spectrophotometer can be either single beam or double beam. The earliest design is based on a single beam where all the light passes through the sample cell and I_0 must be measured by removing the sample. In

a double-beam instrument, the light is split into two beams before it reaches the sample. One beam is used as the reference; the other beam passes through the sample. Samples for UV/Vis spectrophotometry are most often liquids, although the absorbance of gases and even of solids can also be measured.

5.5 Transmission Electron Microscopy (TEM)

TEM and HRTEM (High Resolution TEM) offer the possibility to acquire images of nanostructures at the atomic scale [17, 40]. The main parts of TEM are a vacuum system, a high voltage source and a column that consists of an electron gun, a condenser lens and apertures, a specimen holder, an objective lens system, an objective aperture intermediate, a projector lens system and an image recording facility. The vacuum in the column is maintained below 10^{-6} mbar using various pumps. The electrons emitted from a tungsten Zr-coated Field Emission Gun (FEG) are accelerated by the high voltage source to an energy range of 200KeV. Then they are collected and focused onto the sample by the condenser lens system which provides control over the brightness and controls the size of the beam hitting the specimen. The focused electrons pass through the sample which is held in a holder capable of providing specific diffraction conditions by tilting the sample around two axes. The transmitted electrons then pass through the objective lens. The objective lens is the key lens system which determines the ultimate resolution of the instrument. All the lens systems used are electro-magnetic and are subject to aberrations. The electrons transmitted through the sample can either be diffracted or scattered in the forward direction. This facilitates two modes of imaging by selecting

which electrons are used to make up the image and are called diffraction mode and image mode (Fig.(5.5).

In diffraction mode the diffracted electrons from the sample pass through the objective lens and are focused in the back focal plane producing the diffraction pattern [17, 40, 41, 42]. A selected area diffraction (SAD) aperture is used to select electrons from a certain region such that the diffraction pattern can be related to a specific area. In the case of convergent electron diffraction or nano beam diffraction no apertures are used. Further magnification occurs in the intermediate and projector lens system which determine whether a diffraction pattern or an image is formed. The diffraction pattern formed in the back focal plane of the objective lens becomes the object plane of the intermediate lens which further magnifies the diffraction pattern. The back focal plane of the intermediate lens becomes the object plane of the projector lens and the final pattern is formed on a screen or photographic plate placed at the back focal plane of the projector lens. In the image mode electrons from the objective lens pass through an objective aperture and the image formed at the image plane of objective lens becomes the object plane of the intermediate lens and further magnification is achieved. The image plane of the intermediate lens forms the object plane for the projector lens and the final image is formed on a screen or photographic plate placed at the image plane of the projector lens. There are several modes of imaging, such as bright field imaging, dark field (DF) imaging and high resolution imaging (Fig.5.6).

In bright field imaging crystallites or defects in the sample will scatter the direct beam and will appear as dark features in the image. In dark field

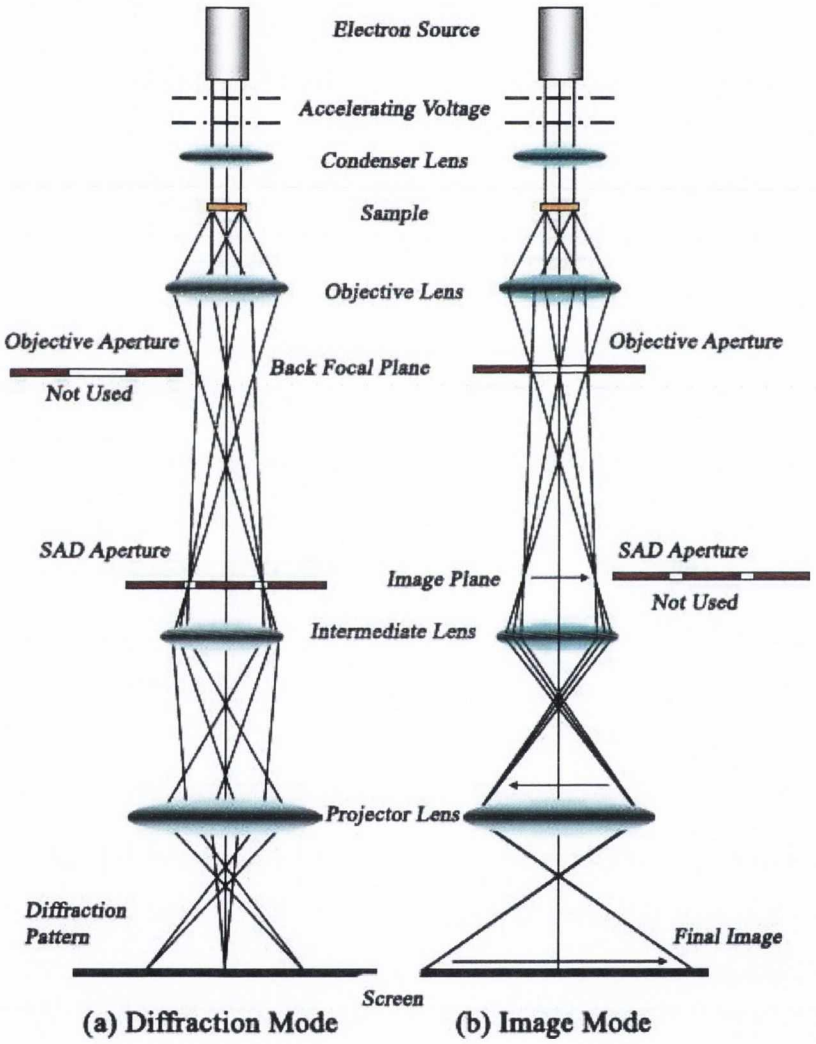

Figure 5.5: Schematic of the operation of a transmission electron microscope in (a) diffraction mode and (b) image mode.

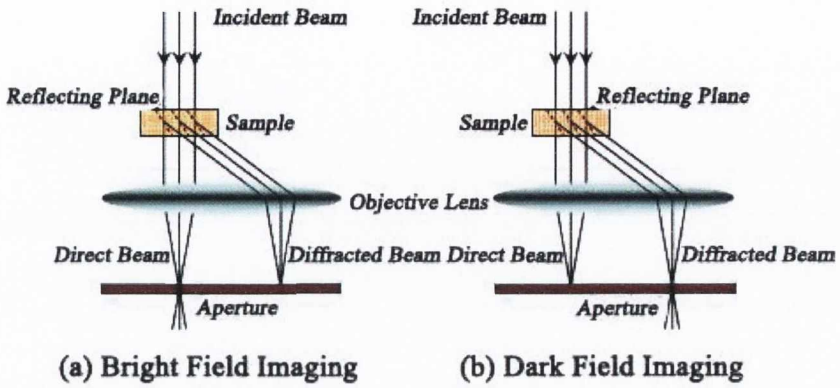

Figure 5.6: Schematic of the two imaging modes (a) bright field imaging and (b) dark field imaging.

imaging, a diffracted beam is used. This is shown in Figure 5.6. The dark field imaging procedure shown is called low resolution dark field; a second approach can be used to acquire a DF image: the diffracted beam chosen can be tilted to bring it to the optical axis of the column, so that an high resolution DF image can be recorded. In both cases the features will be bright in the image, while everything else will be dark. In High Resolution imaging amplitudes are not used for image formation. Indeed contrast comes from the interference in the image plane of the electron wave. Despite the impossibility to record the phase of the electron wave, it still carries the information about the sample and generates contrast in the image, thus the name phase-contrast imaging [17, 40, 41, 42].

5.5.1 Instrumentation details

All TEM measurements of Al_2O_3 presented in this work were performed at National Centre for High Resolution Microscopy, Technical University of Delft, The Netherlands. All the experiments were carried out in a FEI Tecnai F20, equipped with a FE gun and operated at 200 kV. This machine is fitted with a post-column GIF system to collect EELS spectra and EFTEM images. The specimen was produced according to the conventional procedure used to prepare TEM cross sections.

5.6 High Temperature Tube Furnace

The sample preparation requires the annealing of sapphire substrates at high temperature in order to obtain step bunching. All the experiments were performed using a Pyro Therm tube furnace which has a maximum temperature of 1200°. The furnace can be equipped with quartz tubes inside the heating ceramic tube in order to anneal samples in a selected atmosphere. It is equipped with a PID controller to control the temperature.

References

[1] I.V. Shvets, H.C. Wu, V. Usov, F. Cuccureddu, S.K. Arora, and S. Murphy. *Appl.Phys.Lett.*, 92:023106, (2008).

[2] F. Cuccureddu, V. Usov, S. Murphy, C. O'Coileain, and I.V. Shvets. *Rev.Sci.Inst.*, 79:053907, (2008).

[3] J.R. Heffelfinger, M.W. Bench, and C.B. Carter. *Surf.Sci.*, 370:L168, (1997).

[4] J.R. Heffelfinger and C.B. Carter. *Surf.Sci.*, 389:188, (1997).

[5] L. Pham Van, O. Kurnosikov, and J. Cousty. *Surf.Sci.*, 411:263, (1998).

[6] O. Kurnosikov, L. Pham Van, and J. Cousty. *Surf.Interface Anal.*, 29:608, (2000).

[7] O. Kurnosikov, L. Pham Van, and J. Cousty. *Surf.Sci.*, 459:256, (2000).

[8] P.R. Ribic and G. Bratina. *Surf. Sci.*, 109:13138, (2006).

[9] M. Yoshimoto, T. Maeda, T. Ohnishi, H. Koinuma, O. Ishiyama, M. hinohara, M. Kubo, R. Miura, and A. Miyamoto. *Appl.Phys.Lett.*, 67:2615, (1995).

[10] R.C. Barrett and C.F. Quate. *J.Vac.Sci.Technol.A*, 83:400, (1990).

[11] T. Suetsugu, T.and Yamazaki, S. Tomabechi, K. Wada, K. Masu, and Tsubouchi K. *Appl.Surf.Sci*, 117:540, (1997).

[12] G. Binnig, C.F. Quate, and C. Gerber. *Phys.Rev.Lett.*, 56:930, (1986).

[13] G. Binnig, C. Gerber, E. Stoll, T.R. Albrecht, and C.F. Quate. *Europhys.Lett.*, 3:1281, (1987).

[14] G. Meyer and N.M. Amer. *Appl.Phys.Lett.*, 53:1045, (1988).

[15] G. Meyer and N.M. Amer. *Appl.Phys.Lett.*, 57:2089, (1990).

[16] G. Meyer and N.M. Amer. *Appl.Phys.Lett.*, 56:2100, (1990).

[17] B. Bhushan. *Springer Handbook of Nanotechnology.* Springer, Berlin, (2004).

[18] T.R. Albrecht, S. Akamine, T.E. Carver, and c.F. Quate. *J.Vac.Sci.A*, 8:3386, (1990).

[19] N.A. Burnham, D.D. Domiguez, R.L. Mowery, and R.J. Colton. *Phys.Rev.Lett.*, 63:1931, (1990).

[20] N.A. Burnham, R.J. Colton, and H.M. Pollock. *J.Vac.Sci.Tech.A*, 9:2548, (1991).

[21] V. Scherer, W. Arnold, and B. Bhushan. *Surf.Inter.Anal.*, 27:578, (1999).

[22] B. Bhushan and C. Dandavate. *J.Appl.Phys.*, 87:1201, (2000).

[23] www.ntmdt.com.

[24] O. Marti, B. Drake, and P.K. Hansma. *Appl.Phys.Lett.*, 51:484, (1987).

[25] T.R. Albrecht and C.F. quate. *J.Appl.Phys.*, 62:2599, (1987).

[26] S. Stiess, A. Richter, B.V. King, M. Reitsma, and R. Smith. *Surf.Interf.Anal.*, 36:1246, (2004).

[27] S. Morita, R. Wiesendanger, and E. Meyer. *Non-Contact Atomic Force Microscopy.* Springer, Berlin, (2002).

[28] R. Garcia and R. Perez. *Surf.Sci.Rep.*, 47:197, (2002).

[29] F.J. Giessibl. *Rev.Mod.Phys.*, 75:949, (2003).

[30] W.N. Sharpe. *Springer Handbook of Experimental Solid Mechanics.* Springer, Berlin, (2008).

[31] E. Meyer, H.J. Hug, and R. Bennewitz. *Scanning Probe Microscopy: the lab on a tip.* Springer, Berlin, (2004).

[32] Y. Martin, C.C. Williams, and H.K. Wickramasinghe. *J.Appl.Phys.*, 61:4723, (1987).

[33] T.R. Albrecht, T.R. Grutter, H.K. Horne, and D. Rugar. *J.Appl.Phys.*, 69:668, (1991).

[34] F.J. Giessibl. *Science*, 267:68, (1995).

[35] C. Barth and M. Reichling. *Nature*, 414:54, (2001).

[36] I. Schmitz, M. Schreiner, G. Friedbacher, and M. Grasserbauer. *Appl.Surf.Sci.*, 115:190, (1997).

[37] D.P. Ames and S.J. Chelli. *Surf.Coat.Tech.*, 187:199, (2004).

[38] S. Magonov and M.G. Heaton. *Am.Lab.*, 30:9, (1998).

[39] M. Bass. *Handbook of Optics, vol.II.* McGraw-Hill, USA, (1995).

[40] D.B. Williams and C.B. Carter. *Transmission Electron Spectroscopy.* Cambridge University Press, Cambridge, UK, (1996).

[41] L. Reimer and H. Kohl. *Transmission electron Spectroscopy.* Springer, USA, (2008).

[42] M. De Graef. *Introducion to Conventional Transmission electron Spectroscopy.* Cambridge University Press, Cambridge, UK, (2003).

Chapter 6

Annealing of α-alumina

Maledetta sie tu, antica lupa,
che più di tutte l'altre bestie hai preda
per la tua fame sanza fine cupa!
D.Alighieri (La Divina Commedia, Purgatorio XX, 82-84)

In the last few years nanowires and nanoparticles have received a great deal of attention. The fabrication of these structures can be realized utilizing substrates which offer a step and terrace morphology. Controlling the surface evolution of the substrate by annealing allows to prepare appropriate templates for the fabrication of nanostructures [1, 2, 3, 4, 5, 6].

The (0001)α-alumina surface is an attractive substrate for the growth of thin-film materials [6, 7, 8, 9, 10, 11, 12, 13, 14, 15, 16, 17, 18]. Annealing α-Al_2O_3

samples for several hours at high temperatures in air is known to produce a terrace-and-step morphology [19, 20, 21, 22, 23, 24, 25, 26, 27, 28]. In this chapter, the results of an investigation carried out on flat and vicinal sapphire samples with a miscut angle of 3 degrees will be presented [29]. The flat samples were studied in collaboration with Dr. S.I.Bozhko, Institute of Solid State Physics RAS, Chernogolovka, Moscow district, 142432 Russia.

6.1 Low-index Sapphire

In order to study the surface evolution of flat sapphire, substrates from "MTI Corporation" were annealed for different times at different temperatures [30]. By "flat" substrate we mean a substrate with a negligibly small miscut angle (less than 0.5 degrees or even 0.1 degrees). Figure 6.1 shows the surface of a sapphire substrate after six hours of annealing at 1100°C in air. All the annealing experiments have been carried out in air as sapphire is known to produce step and terrace under normal atmosphere.

The surface shows a clear stepped morphology but the terrace edges are poorly defined and the steps are quite low: around 0.2 nm high. This is actually the distance between two consecutive oxygen [0001] atomic planes of the alumina cell [31].

Increasing the annealing up to twelve hours shows no change in the surface morphology and step height. At this stage the temperature is probably not high enough for the step bunching to happen; reported step bunching usually happens at higher temperature where the surface atoms have enough energy to rearrange in a different and stable configuration [21, 23]. This is confirmed

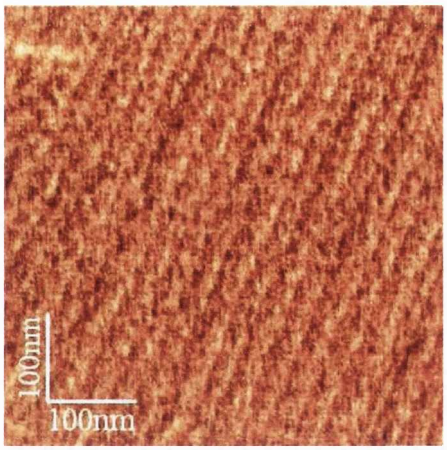

Figure 6.1: AFM flat sapphire after six hours at 1100°C.

when the flat substrates are annealed at higher temperature. Fig. 6.2 shows a flat sapphire sample after annealing for (a) 6 hours and (b) 12 hours at 1350°C. A stepped surface is clearly visible.

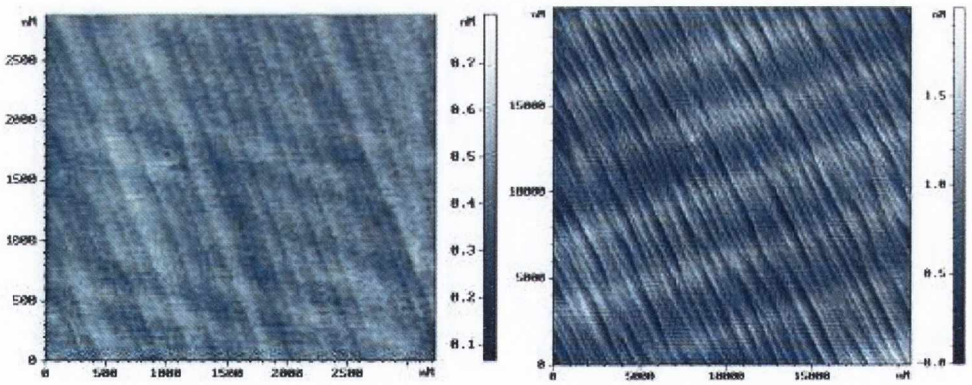

(a) α-Al_2O_3 ann.6hrs. at 1350°C

(b) α-Al_2O_3 ann.12 hrs at 1350°C

Figure 6.2: (0001) Flat Sapphire surface morphology after 6h and 12h annealing at 1350°C.

Faceting of the surface, i.e. the transformation of a planar surface into two or more surfaces, is commonly observed and has been explained assuming

that the decomposition of the surface structure is due to the minimization of the overall surface free energy. The faceting process is thought to occur as a surface evolution through a series of distinct stages, beginning with the nucleation and growth of individual facets, formation of facet domains and coalescence of domains and single facets [20, 32, 33]. The type of structure developed is dependent on the material and orientation of the surface. The widespread results in the literature on the crystallographic orientation of the steps, stress the complexity of sapphire surface evolution. The (0001) surface of sapphire was found to facet into a terrace-and-step morphology consisting of (0001) terraces and steps attributed to the gathering of several c/6 steps, where c=1.3nm is the parameter of the alumina unit cell along the c-axis: the hexagonal unit cell of alumina along the c-axis comprises six layers of oxygen divided by double layers of aluminum [19, 21]. The dimension of the unit cell along the c-axis is 1.30nm so that the height of a c/6 monostep is 0.2 nm. The steps in Fig.6.2(a) are therefore single-atomic steps 0.2nm high, corresponding to $c/6$. The periodic step structure corresponds to a miscut of 0.15°. Increasing the annealing time, the steps are observed to bunch together and form facets of c-height and larger, e.g. 12 hours annealing at the same temperature produces a step bunched surface clearly visible in Fig.6.2(b). Presumably the initial formation of monoatomic steps as well as their gathering into higher steps provides a means of lowering the overall surface energy by creating low-energy inclined facets.

6.2 Vicinal sapphire

In order to better control the formation of bunched and higher steps we decided to investigate the surface evolution of miscut sapphire substrates. Samples of c-plane Sapphire with 3° miscut along the (1-210) direction (Fig.6.3), 10mm x 10mm x 0.5mm in dimension, were cleaned with isopropanol, methanol and acetone and then annealed in a tube furnace under ambient atmosphere at 1100°C for different timescales, ranging from 6 to 12 hours.

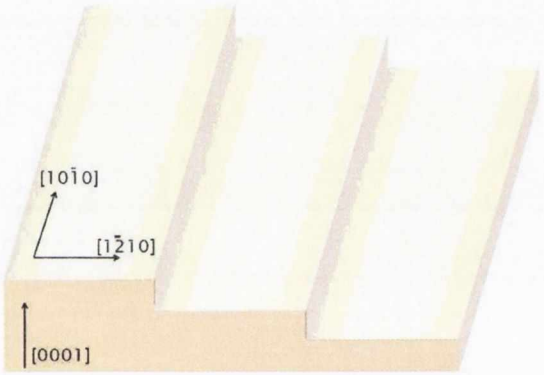

Figure 6.3: Sketch of c-plane vicinal Sapphire used for experiments

Special precautions were taken to minimize the exposure of the surface to any contamination from the furnace environment by annealing the samples inside an alumina crucible. To maximize the temperature uniformity the furnace ends were closed with thermal insulating bricks. The cooling down time of the furnace is relatively short at high temperature (100°C/min) meaning that the morphology of the surfaces measured corresponds to those formed at high temperature.

From the AFM pictures in Fig.6.4 and 6.5 the stepped structure of the sub-

strate after 6 hours of annealing at 1100°C is clearly visible. Analysis of the AFM images showed that the surface is covered with terraces separated by steps whose height ranges from 0.2 nm for a monoatomic step to a higher value where monosteps bunch together, running straight and regular all over the entire surface. They run parallel to the $[10\bar{1}0]$ direction and perpendicular to the original miscut direction, $[1\bar{2}10]$.

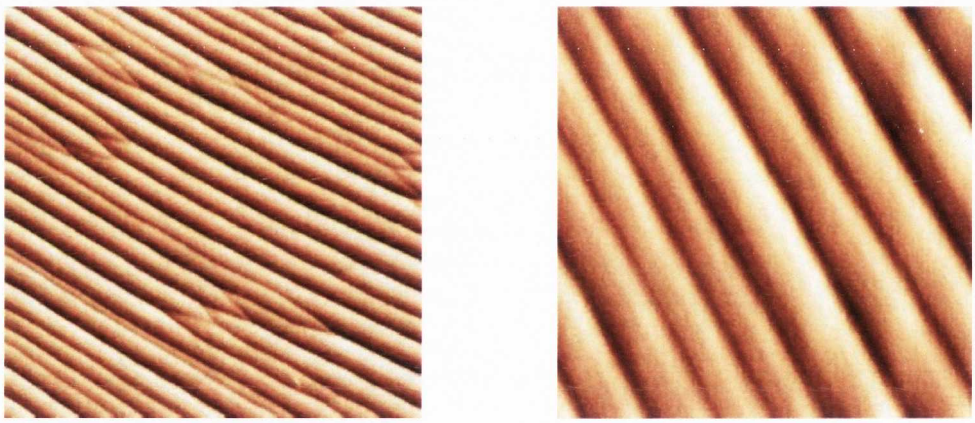

(a) 1μmx1μm (b) 180nmx180nm

Figure 6.4: (0001) Sapphire surface morphology after 6 hrs annealing at 1100°C.

The stepped structure as shown in these picture is quite typical and routinely repeatable. Figure 6.6 shows three rotated scans obtained a three different scanning directions for a Sapphire sample annealed at 1100°C for 6 hours.

A statistical analysis of the step width distribution was carried out considering a conspicuous number of steps from several samples. The results are reported in Fig.6.7 for both 6 hours and 12 hours annealed samples. The annealing process produces, whenever performed for 6 hours at 1100°C, a step and terrace morphology with an average step height of 1.5 $\pm$ 0.5nm and an

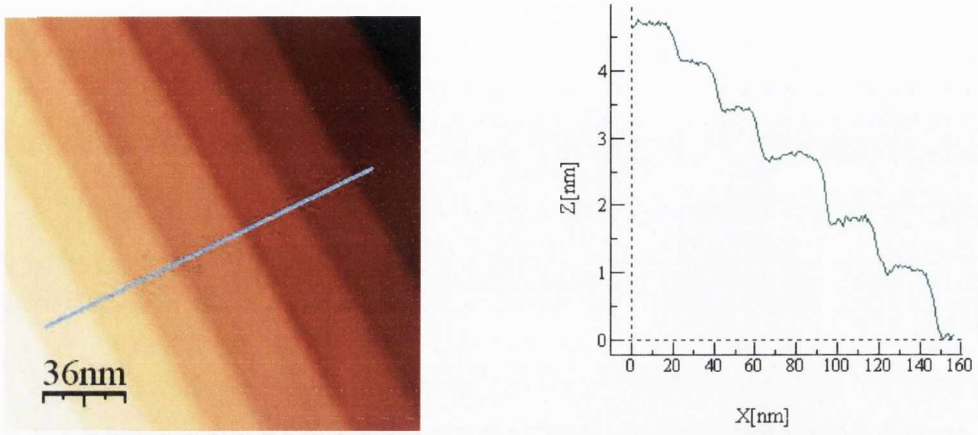

(a) 180nmx180nm

(b) Step profile

Figure 6.5: (0001) Sapphire step profile after 6 hrs annealing at 1100°C in air.

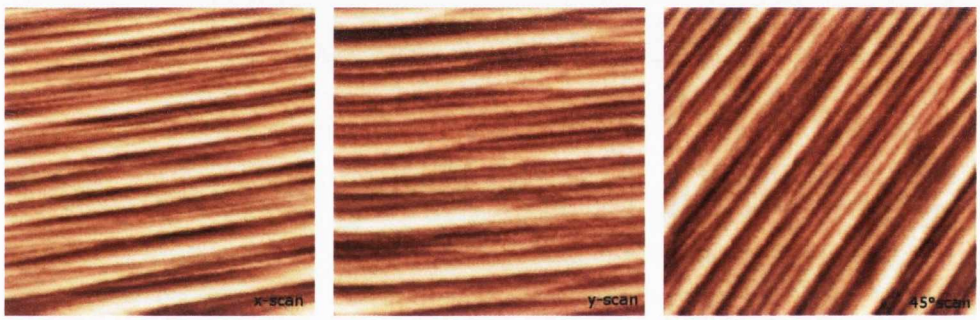

Figure 6.6: Rotated AFM scans obtained at three different scanning directions for a Sapphire sample annealed at 1100°C for 6 hours. The x-scan line direction is aligned with the steps. Scanning area is 1μm X 1μm.

average terrace width of 44.2 $\pm$ 13.7nm.

However, the symmetry is broken by the number of junctions, i.e. local areas where two steps merge and form one higher step. At these junctions the steps "zip" together leading to the formation of double, triple or multiple steps from the coalescence of monosteps and providing a mechanism of facet coarsening.

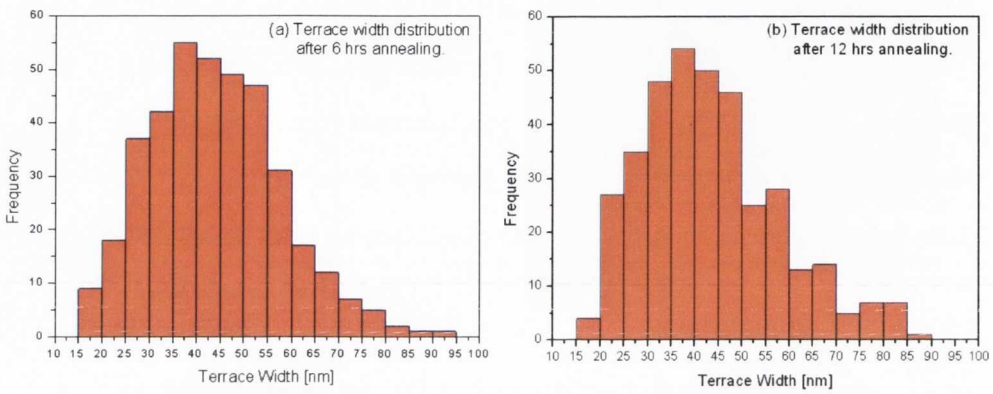

(a) 6 hrs annealing

(b) 12 hrs annealing

Figure 6.7: Terrace width distributions after (a) 6 hours and (b) 12 hours annealing at 1100°C.

Some studies reported that there is not correspondence between the step direction and the low index crystallographic direction [21] while other studies showed that the annealing of c-plane sapphire produces a step-and-terrace morphology where the steps follow low index directions [34]. The misorientation in our samples was chosen in such a way that the steps follow low index directions, i.e. parallel to $[10\bar{1}0]$.

In the proximity of the merging areas, parallel steps actually change direction generating some faceting. From analysis of the AFM scans (Fig.6.8) the angle between the different directions turns out to be around 150° which corresponds to the angle between the $[1\bar{2}10]$ and the $[1\bar{1}00]$(Fig.6.8(b)). The steps edge are oriented along $[1\bar{2}10]$ but in correspondence of the junctions they change direction and run along a different, but energetically favorable, low index direction $[1\bar{1}00]$ (equivalent to $[10\bar{1}0]$).

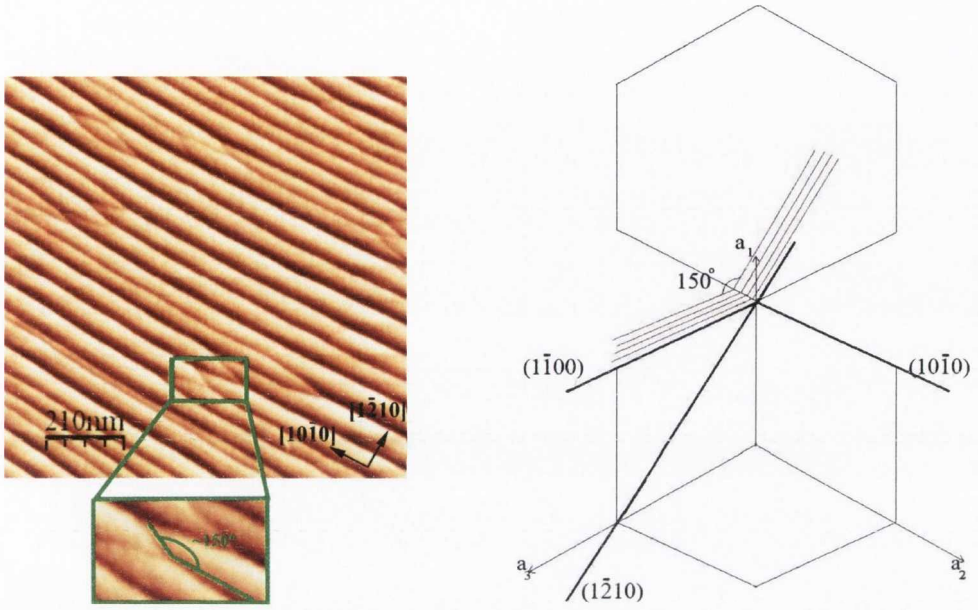

Figure 6.8: Sapphire substrate after annealing. The angle between the facets corresponds to the angle between two low-index directions.

In order to have a full insight into the surface morphology, TEM analysis was carried out in collaboration with the NCHREM group of the Prof. Zandbergen of TUDelft, Delft, Netherlands to closely analyze the surface steps. TEM micrographs confirm the step-and-terrace structure of the samples. In Fig.6.9 a cross section view of the sample is shown, with the α-Al_2O_3 represented by the dark part while the brighter area is the glue used to prepare the sample for the TEM analysis. The width of the terraces obtained from the analysis of the TEM micrographs matches the results from the AFM scans. Fig.6.10 is a high resolution micrograph of the alumina sample viewed along [10$\bar{1}$0] with the linear arrays of oxygen atoms in evidence. The crystal structure of alumina is clearly visible and it is possible to investigate the morphology of a single

step. The micrograph shows that the macrostep is formed by the bunching of several monosteps, attesting that the annealing causes a step bunching process on the surface. In this case the gathering of 10 monosteps by step bunching leads to the formation of a 2 nm high macrostep.

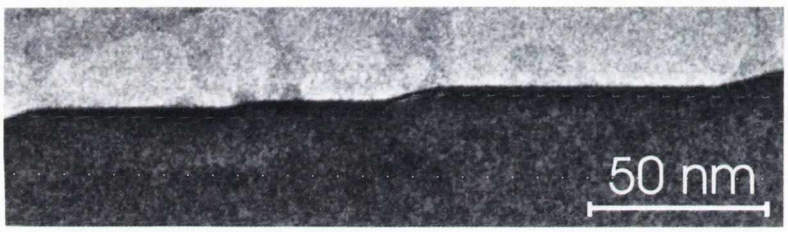

Figure 6.9: Low magnification micrograph of the alumina sample viewed along [10$\bar{1}$0].

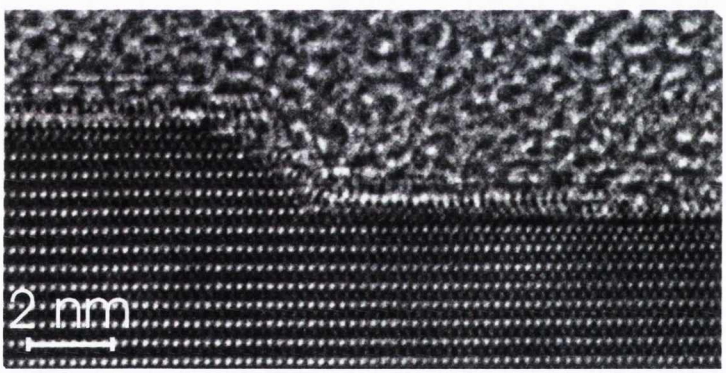

Figure 6.10: High resolution micrograph of the alumina sample viewed along [10$\bar{1}$0].

Increasing the annealing time does not seem to produce any further substantial changes in the average step height or the average terrace width. Fig.6.11 shows AFM images of vicinal sapphire samples annealed in air at 1100°C for 12 hours (6+6 hours).

The samples annealed for 12 hours show a slightly higher average step height of 1.8 $\pm$ 0.7 nm while the average terrace width does not change substantially,

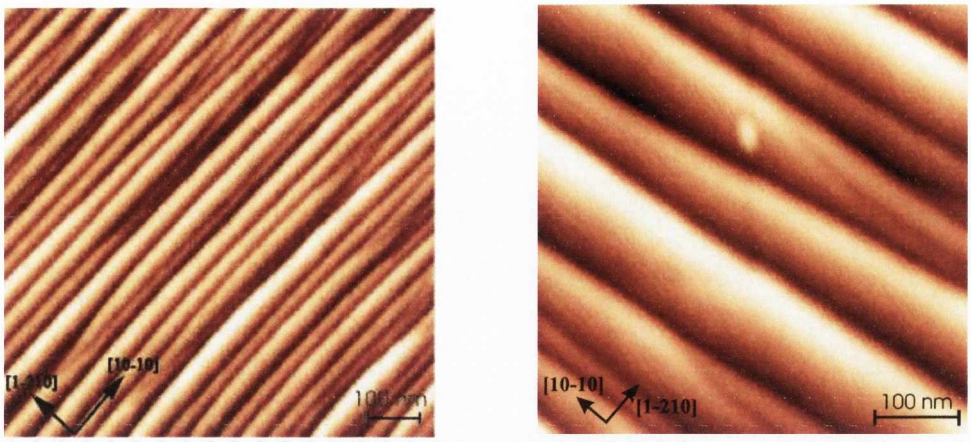

Figure 6.11: Sapphire surface morphology after 12 hrs annealing at 1100°C.

going from 44.2 ± 13.7 nm for the 6 hours annealed samples to 43.6±14.7 nm for the 12 hours annealed samples (Fig.6.7(b)).

Preliminary annealing studies on different crystallographic sapphire planes (r- and a-plane) have been performed in collaboration with Dr. S.Bohzko. They show that r-plane possess a noticeable uniformity in step height and terrace width which could make them more attractive candidates as templates for growing nanowires.

For the aim of this project, the shallow angle deposition, the best surface structure possible is represented by a terrace-and-step morphology with uniformly high steps and a narrow distribution of terrace widths in order to enhance the shadowing effect and favor the alignment of the deposited material along the steps. In the next chapter the deposition experiments performed on these samples will be discussed.

6.3 Conclusions

The morphological surface evolution of c-plane alumina samples upon annealing was investigated for flat and vicinal substrates. The annealing temperature was set at 1100°C since lower temperatures did not produce any satisfactory results on any of the samples. The samples were annealed for different times. Flat samples did not show any step bunching even for long annealing times, probably due to the fact that the temperature represents the limiting factor being too low for the surface atoms to rearrange. This is actually confirmed when the flat substrates are annealed at higher temperature.

Conversely, vicinal samples provided good results since the high temperature annealing process was able to trigger the step bunching process. The surface morphology presents a number of coalescence points, i.e. local areas where two steps merge and form a higher step. Close to the merging areas, parallel steps change direction running along a different, but energetically favorable, low index direction.

References

[1] C. Barth and M. Reichling. *Nature*, 414:54, (2001).

[2] H.R. Lim, I.S. Kim, D.H. Kim, Y.K. Park, and J.C. Park. *Prog. Supercond.*, 1:146, (2000).

[3] M. Huth, K.A. Ritley, J. Oster, H. Dosch, and H. Adrian. *Adv.Funct.Mater.*, 12, No.5:333, (2002).

[4] B. Wolfing, K. Theis-Brohl, C. Sutter, and H. Zabel. *J.Phys.: Condens.Matter*, 11:2669, (1999).

[5] X.R. Huang, J. Bai, M. Dudley, R.D. Dupuis, and U. Chowdhury. *Appl.Phys.Lett.*, 86:211916, (2005).

[6] T. Suetsugu, T.and Yamazaki, S. Tomabechi, K. Wada, K. Masu, and Tsubouchi K. *Appl.Surf.Sci*, 117:540, (1997).

[7] T.J. Minvielle, R.L. White, M.L. Hildner, and R.J. Wilson. *Surf.Sci.*, 366:L755, (1996).

[8] P.E. Dyer, S.R. Jackson, P.H. Key, W.J. Metheringham, and M.J.J. Schmidt. *Appl.Surf.Sci.*, 96-98:849, (1996).

[9] I. Stara, V. Nehasil, and V. Matolin. *Surf.Sci.*, 365:69, (1996).

[10] D. Wang, B.A. Sheriff, M. McAlpine, and J.R. Heath. *Nano Res.*, 1:9, (2008).

[11] L.J. Singh, Z.H. Barber, Y. Miyoshi, Y. Bugoslavky, W.R. Branford, and L.F. Cohen. *Appl. Phys. Lett.*, 84:2367, (2004).

[12] M. Shirakawa, M. Miura, T. Ohazama, Y. Shingai, A. Saito, M. Mukaida, and S. Ohshima. *Physica C*, 412-414:1277, (2004).

[13] J. Grabowska, K.K. Nanda, E. McGlynn, J.P. Mosnier, and M.O. Henry. *Surf.Coat.Tech*, 200:1093, (2005).

[14] C.L. Pang, H. Raza, S.A. Haycock, and G. Thornton. *Surf.Sci.*, 460:L510, (2000).

[15] J. Feng, W. Zhang, and W. Jiang. *Phys.Rev.B*, 72:115423, (2005).

[16] K. Luo, X. Lai, C.W. Yi, K.A. Davis, K.K. Gath, and Goodman D.W. *J.Phys.Chem.B*, 109:4064, (2005).

[17] D.G. Van Campen and J. Hrbej. *J.Phys.Chem.*, 99:16389, (1995).

[18] F.X. Bock, T.M. Christensen, S.B. Rivers, L.B. Doucette, and R.J. Lad. *Thin Solid Films*, 468:57, 2004.

[19] J.R. Heffelfinger, M.W. Bench, and C.B. Carter. *Surf.Sci.*, 370:L168, (1997).

[20] J.R. Heffelfinger and C.B. Carter. *Surf.Sci.*, 389:188, (1997).

[21] L. Pham Van, O. Kurnosikov, and J. Cousty. *Surf.Sci.*, 411:263, (1998).

[22] O. Kurnosikov, L. Pham Van, and J. Cousty. *Surf.Sci.*, 459:256, (2000).

[23] O. Kurnosikov, L. Pham Van, and J. Cousty. *Surf.Interface Anal.*, 29:608, (2000).

[24] R.L. Schwoebel and E.J. Shipsey. *J.Appl.Phys.*, 37:3682, (1966).

[25] M. Sato and M. Uwaha. *Phys.Rev.B*, 51:11172, (1995).

[26] N. Ravishankar and C.B. Carter. *J.Mater.Res.*, 17:98, (2002).

[27] P.R. Ribic and G. Bratina. *Surf. Sci.*, 109:13138, (2006).

[28] M. Yoshimoto, T. Maeda, T. Ohnishi, H. Koinuma, O. Ishiyama, M. hinohara, M. Kubo, R. Miura, and A. Miyamoto. *Appl.Phys.Lett.*, 67:2615, (1995).

[29] F. Cuccureddu, S. Murphy, I.V. Shvets, M. Porcu, H.W. Zandbergen, N.S. Sidorov, and S.I. Bohzko. *In Preparation.*

[30] www.mticrystal.com.

[31] W.E. Lee and K.P.D. Lagerlof. Structural and electron diffraction data for sapphire (α-al$_2$o$_3$). *J.Electron Microsc.Technol.*, 2:247, (1985).

[32] S.R. Gilliss, A. Altay, J. Reisterer, N. Ravishankar, and C.B. Carter. *Mat.Res.Bull.*, 750:379, (2002).

[33] C.B. Carter, J.R. Heffelfinger, and M.W. Bench. *Surf.Sci.*, 343:1161, (1995).

[34] D.W. Susnitzky and C.B. Carter. *J.Am.Ceram.Soc.*, 75:2463, (1992).

Chapter 7

Deposition and growth of metal nanowires

Quo usque tandem abutere, Catilina, patientia nostra?
Quam diu etiam furor iste tuus nos eludet?
Quem ad finem sese effrenata iactabit audacia?
M.T.Cicero (Orationes in Catilinam I)

The ATLAS system has been used to perform depositions on the stepped samples previously described. One of the main features of the ATLAS technique is its own universal applicability to any kind of material. The geometrical considerations which are the foundation of the technique do not exclude the use of any type of material [1]. In order to demonstrate this point samples

of silver, iron and cobalt nanowires were deposited by means of the ATLAS technique.

7.1 Geometrical considerations

As previously said, the technique is based on shallow angle deposition and on the exploitation of the shadowing effect provided by vicinal substrates. The quality of the stepped surface is critical since it will affect the shadowing and overall growth of the nanostructures. Ideally, high steps would be desirable because they can provide a degree of shadowing which can be more easily controlled by changing the deposition angle. Furthermore, uniformity of steps is an important parameter because, as already discussed, affects the proximity of the nanowires to each other and their extension along a single step. In the previous chapter it was shown in Fig.6.7 that the terrace width distribution is fairly narrow with an average width of 44.2 $\pm$ 13.7 nm for the 6 hours annealed samples and 43.6$\pm$14.7 nm for the 12 hours annealed samples. This figures are quite good and make the stepped alumina a suitable template for the growth of nanostructures by means of ATLAS. In fact, as it will be shown in this chapter, silver nanoparticles arrays were successfully and routinely produced. In order to predict how the material will grow on the substrates a few geometrical considerations must be done. In principle, on the basis of the substrate position and the staircase orientation, two different configurations can be realized: they will be called mode1 and mode2 and are schematically illustrated in Fig.7.1.

In mode1 the sample is mounted such a way that the upcoming flux strikes

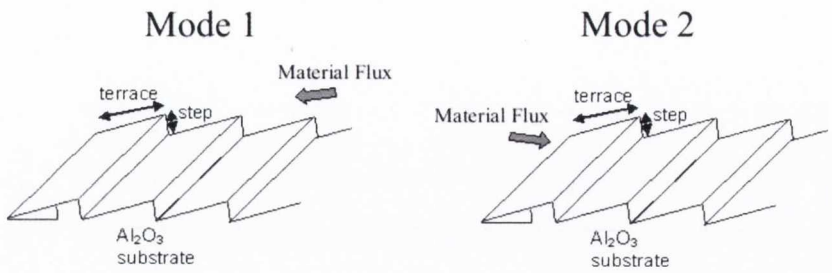

Figure 7.1: The two possible deposition configurations for a collimated beam impinging on a vicinal substrate.

the substrates along the ascending step orientation. This configuration does not provide a proper shadowing by the steps but the material placement is however affected by the step-and-terrace morphology with the growth confined to selected areas. The growth of the material in a perpendicular direction with respect to the terrace is related to the sine of the angle between the collimated beam and the terrace itself while the growth perpendicular to the step edge is proportional to the cosine of the same angle. Since at small angle the cosine is much larger than the sine function one can expect a strong accumulation of material in the proximity of the step edge all along the step length. Although in this configuration the steps do not offer any sort of screening, still from geometrical considerations it arises that the sample will not be completely and uniformly covered by a film. Furthermore by changing the angle one can consequently change the sine and cosine values experimentally achieving a good degree of control on the growth.

In mode2 the sample is mounted with descending steps with respect to the beam. As Fig.7.1 shows, the steps provide a shadowing effect leaving exposed only selected areas of the terraces. Since the atomic beam strikes the terraces

for their whole length the material deposited will decorate the step edges in the form of nanowires. The anisotropy and the width of the nanowires strongly depends on the deposition angle and substrate miscut. Assuming only pure geometrical considerations the flux direction in relation to the step edges determines what areas of the atomic terrace are exposed or shadowed. The width of the nanowires is defined by [1]:

$$w = a\left(\frac{1}{\alpha} - \frac{1}{\alpha + \theta}\right) \tag{7.1}$$

where w is a nanowire width, a is a step height, α is a miscut angle, and θ is a deposition angle. Both α and θ are assumed to be small. The percentage of terrace covered by the material can be expressed also by ([2]):

$$P_{tc} = 1 - \frac{tan(\alpha_m)}{tan(\alpha_m + \theta)} \tag{7.2}$$

The percentage of terrace covered, and then the width of the nanowires can be tuned and controlled by changing the deposition angle or choosing substrates with different miscut. This whole construction is based on pure geometrical factors discarding any other effects. New features might enter the discussion such as atom diffusion due to the atom concentration gradient or substrate temperature.

In terms of deposition angle, it is necessary to specify what the deposition angle refers to. The use of a vicinal substrate requires that the angle is defined clearly since the terraces have a different orientation with respect to the substrate surface. In principle there are two ways to define the angle: it can be considered

as the angle formed between the beam and the terraces or between the beam and the overall substrate surface. The miscut angle needs to be specified for each sample. From now on the angle between the beam and the overall surface will be adopted as reference and indicated with θ.

7.2 Deposition of silver nanowires

Silver nanowires receive great attention as building blocks for nanoscale electronics and photonics nanostructures because they exhibit the highest electrical conductivity among all metals (63.01x10^6 S/m) [3, 4, 5, 6, 7, 8, 9, 10]. Silver nanoparticles have many important applications that range from catalysis [11] to biolabelling and have proven to be useful in surface plasmon resonance analysis, an optical technique that is widely gaining recognition to investigate biological interactions [12, 13, 14].

Silver depositions were performed at an effusion cell temperature of 1056°C (17.1V, 6.0A), about one hundred degrees celsius above the melting point (961°C). In the experimental configuration used, i.e. near high vacuum, and a throw distance of approximately 1 meter, a deposition flux rate of 3.6 $\mathring{A}$/min was obtained. The nominal thickness of each film depends then on the deposition time.

7.2.1 Configuration dependence

As previously explained the vicinal samples can be mounted in two different modes according to the ascending or descending direction of the staircase with respect to the beam and two different outcomes are expected (Fig.7.2).

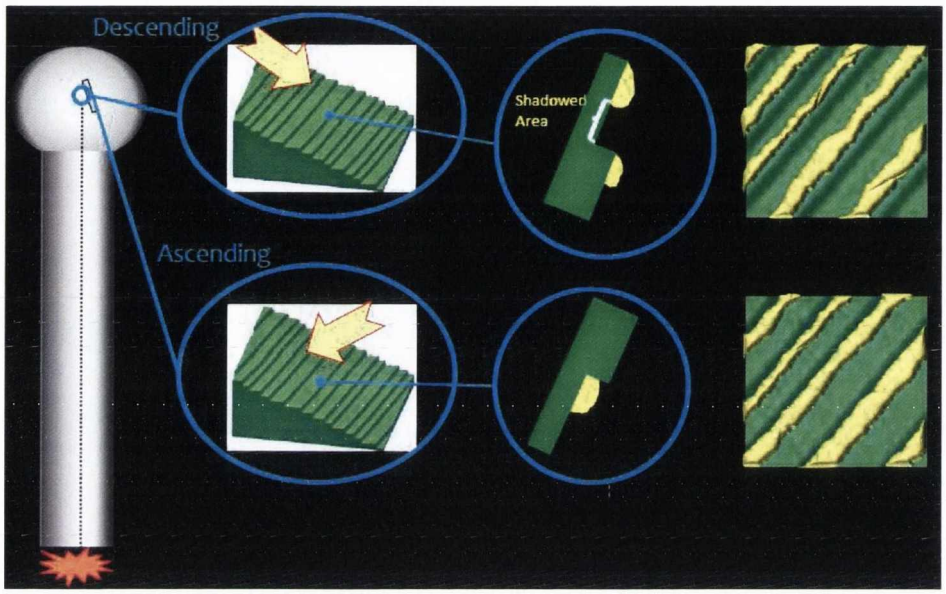

Figure 7.2: Expected growth of the nanostructures on the terraced surface depending of the flux direction.

Figure 7.3 shows two AFM scans of two different samples grown using the same deposition conditions. The only difference between them is the orientation with respect to the incoming flux: Fig.7.3(a) shows the substrate loaded with ascending steps oriented with respect to the beam while in Fig.7.3(b) the steps are descending.

These two samples were produced by deposition of silver for 27 minutes at 3.6 $\mathring{A}$/min with an incident angle of 6°. The AFM shows in both cases a similar morphology: the nanoparticle seem to be closely connected to each other creating arrays of nanowires that run all along the step. For the sample in Fig.7.3(a) the islands forming the nanowire seem to be more discrete while the second sample shows larger islands that seem to cover the whole step.

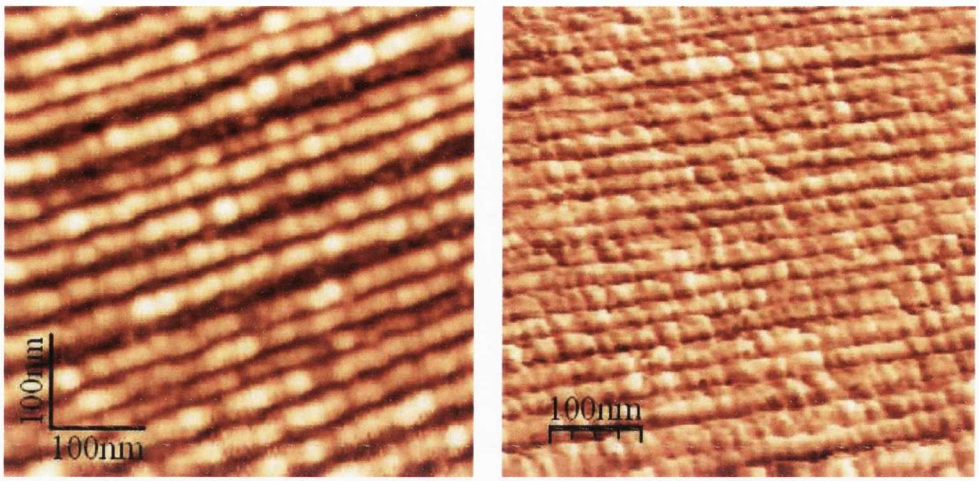

Figure 7.3: AFM images of sapphire substrate after silver deposition on (a) ascending and (b) descending steps.

In the latter case the self-shadowing of the steps seems to be limited and the nanoparticles/nanowires spread out to fill the the terrace. This might be partially due to the exposure angle which leaves over the 50% of the terrace exposed to the beam but other factors can play a role, such as some degree of diffusion and especially the relatively low height of the steps. In order to master a full control of the deposition higher steps are desirable since they allow more freedom with the deposition angle. In any case both configuration modes demonstrate that the ATLAS technique can be used to grow linear and ordered arrays of material.

Figure 7.4 shows three rotated AFM scans of the same sample relative to three different scanning directions, confirming the ordered morphology of the nanostructures.

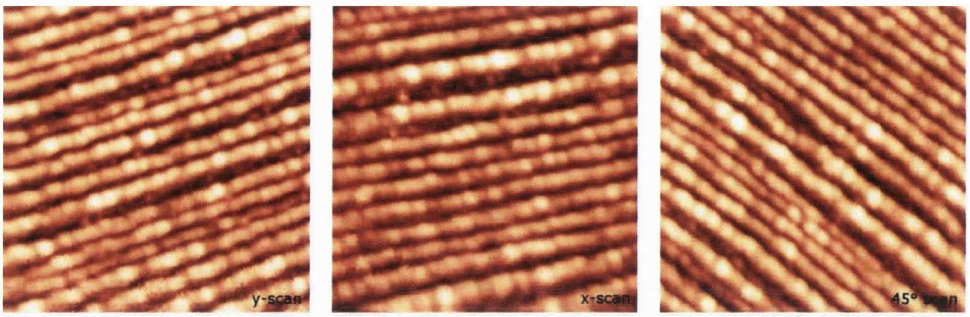

Figure 7.4: AFM rotated images (500nm X 500nm) of sapphire substrate after silver deposition for 27 minutes. The three scans refer to three different scanning directions.

7.2.2 Nanoparticles placement - Steering effect

An interesting aspect of the shallow angle growth is investigating on which particular areas of the terraces the nanostructures tend to grow in relation to the substrate orientation. When the sample is mounted in configuration Mode2, one can expect the particles to grow on the outer edge of the terrace since the inner region is shadowed by the steps. This is what actually happens in general. However, for our samples, the wide angle and especially the low average step height allow for a significant part of the terrace to be covered, minimizing this effect.

The situation is less straightforward when the sample is mounted following the configuration Mode1. In this case one would expect for the islands to grow on the inner side of the step since that region offers an energetically more favorable condition. Although atoms strongly prefer to bind to the bottom edge of the steps, the geometrical proximity of top edges of the steps can lead to atoms landing there instead, significantly altering film morphology. The AFM images in Fig.7.5 shows a sample after silver deposition for 23 minutes

at 3.6$\AA$/min with the corresponding three-dimensional picture in Fig.7.6. The profile analysis in Fig.7.7 clearly reveals that the nanoparticles grow on the outer step edge, conversely to what is expected.

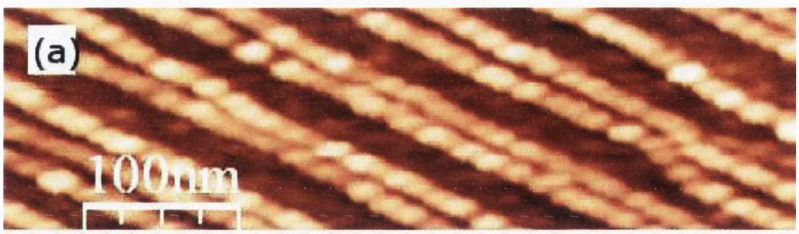

Figure 7.5: AFM scan of silver nanoparticles arrays grown in Model (deposition for 23 minutes at 3.6 $\AA$/min).

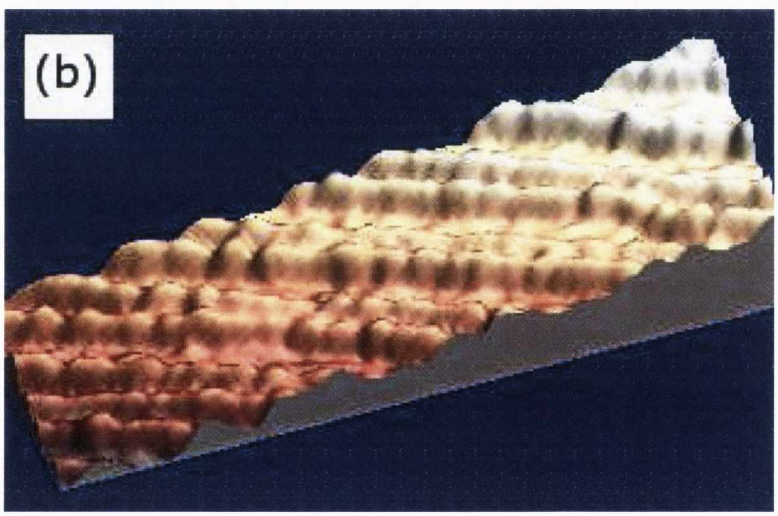

Figure 7.6: 3D image relative to the same sample as Fig.7.5.

This striking results is quite counterintuitive since the outer step-edge does not appear the most favorable nucleation area on the terrace. One possible reason could be the diffusion of adatoms to the outer edge where they can-

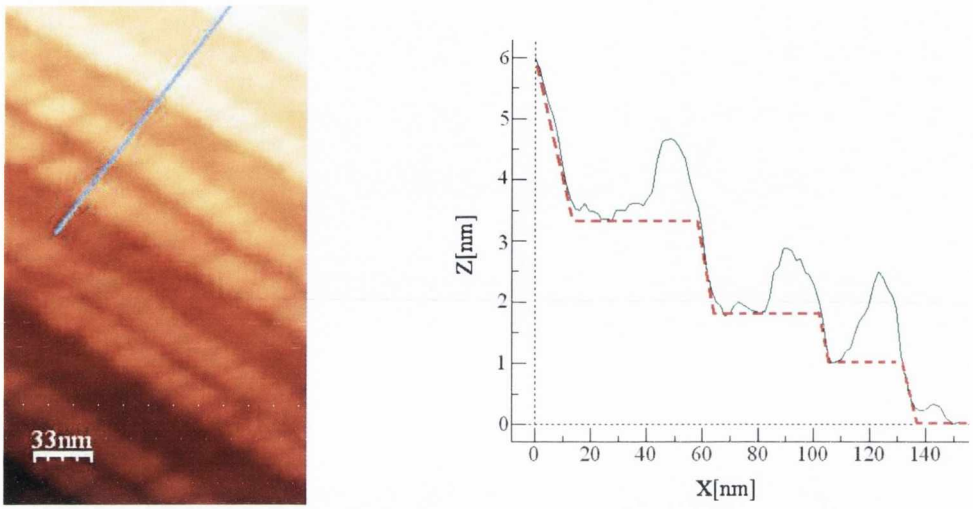

Figure 7.7: AFM images showing the line profile across a sapphire substrate after silver deposition.

not overcome the Ehrlich-Schwoebel barrier and start nucleating. However, the growth is performed at room temperature and one does not expect that adatoms diffuse for long distances. On the other hand, the temperature inside the chamber and on the substrate was not measured in real time and it could be higher than expected. However, similar phenomena have been reported in literature and a possible explanation was offered [15, 16, 17, 18]. In order to explain this apparent anomaly, the so-called "*steering effect*" phenomenon was introduced. When an atom from the impinging flux is approaching a surface at a low incidence angle, it feels a strong interaction force (attractive) that leads to a significant change of trajectory deflecting the atom itself towards the surface normal. This phenomenon is related to the presence of a stepped surface that induces lateral inhomogeneities in the deposition flux affecting the growth morphology. Long-range attractive forces between flux atoms and

substrate atoms lead to substantial deflection of grazing-incident atoms. Flat surfaces are not concerned by this effect which appears to be relevant in metal homoepitaxy at low temperatures: the refraction of the approaching atoms is the same for all atoms and the incident flux remain homogeneously distributed. However, as soon as adatom islands grow, morphology-dependent atom trajectories give rise to a redistribution of the incident atoms, i.e., the incident atom flux depends on the local surface morphology. Fig.7.8 shows evidence of the steering effect: an enhanced flux on the top of the outer step edge results in the preferential growth of the nanoislands on this region.

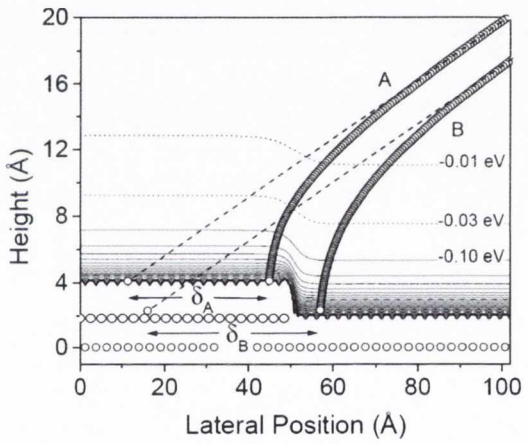

Figure 7.8: Two atom trajectories for a surface with a step edge in the direction perpendicular to the plane of incidence. From [15].

The steering effect is different from a geometrical shadowing effect since in the latter case the flux enhancement would occur on the lower inner step edge and not on the top. Furthermore, the progressive growth of the islands triggers a self-shadowing effect where the nanoparticles screen the area of the terrace behind them further affecting the morphology of the film. This effect is also

strongly dependent on the angle as will be explained in the next section.
Apart from the various speculations, these results seem very interesting and require further investigation in order to be fully understood.
Finally, from the analysis of the samples it seems that there is not straight relation between the terrace width and the nanostructures size. In fact, as it will be clarified in the following sections, the nanoparticles size is governed by other critical parameters such as the deposition angle and the amount of material deposited which is, in turn, determined by the deposition time.

7.2.3 Angular dependence

The deposition angle is a critical parameter since it affects the nanostructure features, such as width and height. The angle determines what portion of substrate is exposed to the beam and consequently the percentage of each terrace subject to be covered by the incoming material (at least within pure geometrical considerations). When the sample is mounted following the Mode2 configuration, the sample area exposed to the flux changes by modulating the angle since the steps cast an angle-dependent shadow on the terraces. At shallow angle the shadowing is significant and the surface area exposed is small. By increasing the angle the screening is reduced and the beam can access a larger area.
In configuration Mode1 the situation appears less straightforward. Apparently the beam can access every part of the substrate but in reality the growth of the nanostructures is confined only to selected areas and it is angle dependent. The AFM images shown in Fig.7.9 illustrate the angle dependence of two silver

nanoparticle films deposited on sapphire samples. The deposition conditions used are the same for both (23 minutes at 3.6 $\AA$/min and 3° miscut sapphire), apart from the deposition angle. Fig.7.9(a) shows the sample after deposition with θ at 3° whilst the sample in Fig.7.9(b) is obtained with θ at 6°.

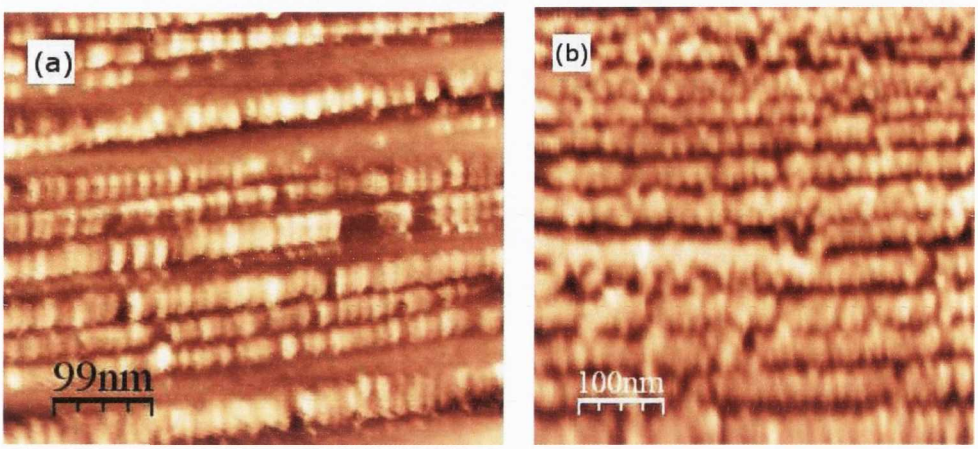

Figure 7.9: AFM images of sapphire substrate after silver deposition showing angular dependence. Depositions were carried out at (a) $\theta = 3°$ and (b) $\theta = 6°$.

At first sight the sample deposited at 6° appears to have a more regular and uniform displacement of nanoislands compared to the sample deposited at 3° where some areas seem uncovered along the terraces. It must be recalled that the nanostructure morphology is strongly influenced by the underlying substrate topography which can actually give rise to such irregular arrangements. The substrate surface topography is critical for the ATLAS technique for which long, regular and straight steps with no merging points are desirable. This implies that the techniques for obtaining regularly faceted surfaces are to be further mastered.

A statistical analysis on a significant number of nanoparticles reveals that the

deposition angle affects the size. The particles on the sample deposited at 3° are 12±2.4 nm wide and 1.8±0.6 nm high but when the angle is increased to 6° the particles become wider, 14.7±3.7 nm, and lower in height, 1.3±0.5 nm. As previously explained, there is no apparent shadowing from the steps but rather a steering effect responsible for the fact that the nanoparticles tend to grow on the upper terrace near the front edge of the step. Whenever the deposition angle is shallow the degree of shadowing provided by the growing islands sitting on the up-step is higher than the case with a wider angle. This results in the atoms accumulating on the top of the islands instead of the terrace nearby with an increase in nanoparticles height. When the angle is wider the overcast/screened region in the terrace in smaller and the atoms can spread out with a consequent lateral growth of the nanoparticles.

7.2.4 Deposition time dependence

By changing the deposition time the amount of material deposited on the substrates increases or decreases. In order to investigate the effects of this dependence on the nanoparticle/nanowire shape several samples were deposited keeping the deposition rate, angle, temperature etc. fixed and changing only the deposition time. Figure 7.10 shows the raising trend of the nanoparticle size as the deposition time increases. The height of the particles seems to be constant around 1.5 nm on average. However, the determination of the height obtained by processing the AFM pictures is quite complicated because of the film morphology and offers only a rough estimate.

Fig.7.11 shows AFM scans of three different sapphire samples after silver

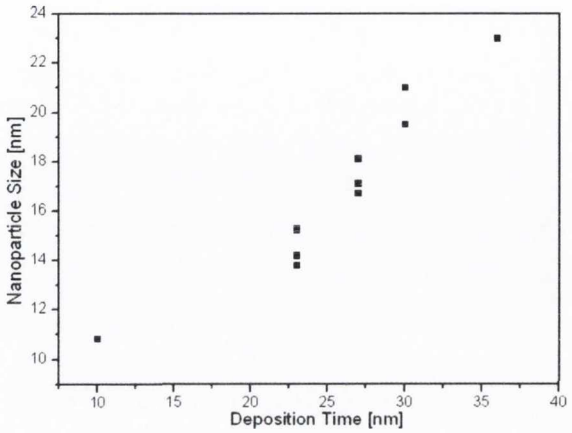

Figure 7.10: Nanoparticle size dependence as a function of the deposition time. All the other parameters are kept fixed.

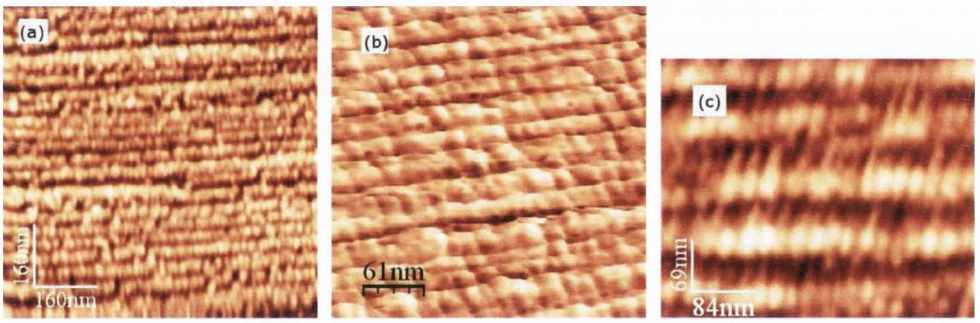

Figure 7.11: AFM images of sapphire substrate after silver deposition for successively higher doses of silver: (a)23, (b)27 and (c)30 minutes.

deposition at 3.6 $\AA$/min for (a)23, (b)27 and (c)30 minutes. The nominal thickness for these samples can be worked out from the deposition rate and amounts to 8.28 nm for the 23 minutes sample, 9.72 nm for the 27 minutes sample and 10.8 nm for the 30 minutes sample. However, these values refer to the substrate mounted in a normal configuration where the beam is at 90° with the substrate plane. The estimated thickness value for the configuration adopted, substrate at 6° with respect to the flux, can be guessed by taking

into account the sine dependence. Since the sample is mounted 6° off the beam axis the predicted values will be respectively around 0.87 nm, 1.02 nm and 1.13 nm. Obviously these thickness values represent only a rough estimate for a planar film deposited onto a planar substrate and do not account for the particular morphology that actually grows on the vicinal substrates. Having said that, the nanoparticles follow the expected trend showing larger sizes for higher deposition time. The shortest deposition time produced nanoparticles of 14.7±3.7 nm in lateral size, increasing to 18.4±4.4 nm for the 27 minutes sample and finally to 20.6±3.7 nm for the last sample.

The island size is also strongly affected by the morphology of the film. The substrate topography influences heavily the way the islands will be distributed on the surface and a regular and uniform step-and-terrace morphology of the substrate is desired to exploit the potential of the ATLAS technique. Anyway this requires a considerable control on the surface preparation which is not always achievable. Previously, the evolution of the sapphire morphology upon annealing was analyzed and it was pointed out that sapphire provides a favorable template but it is also characterized by the presence of coalescing steps. An example is presented in Fig.7.12 where silver was deposited for 15 minutes at 3.6 $\mathring{A}$/min. Despite the small amount of material deposited, the nanoparticles show a fairly large lateral size, around 31.4±5.6 nm, due to the lack of uniformity. The nanoparticles seem to gather on some specific areas of the substrate terraces, where they assume a nanowire-like configuration, with wide gaps in between. This is in turn due to the lack of uniformity of the underlying substrate which is rich in coalescence points. As result the inter-

particle peak to peak spacing is quite high, 55,1 nm, and the irregularity of the morphology emerges also in the deviation standard which has a value of 22.3 nm. As will be more extensively shown in the next chapters, the surface morphology affects the optical properties of the samples.

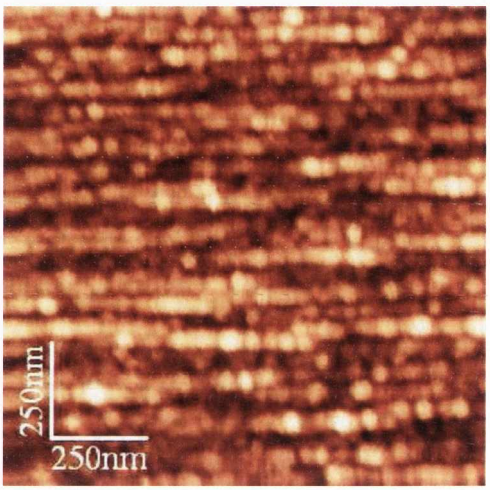

Figure 7.12: AFM images of sapphire substrate after silver deposition for 15 minutes on irregular substrate.

7.2.5 Post-annealing

In order to study the thermal stability of the silver nanoparticles, the effects of annealing in air were investigated. The annealing time was 30 minutes and the annealing temperature was in the range from 200°C to 800°C. The annealing causes aggregations of the particles with progressive loss of the ordered nanostructures. These observations are confirmed by the AFM analysis reported in Fig.7.13

After 30 minutes at 200°C (Fig.7.13(b)) the nanoparticles start to coalesce and overcome the steps creating a slight loss of asymmetry. Further annealing

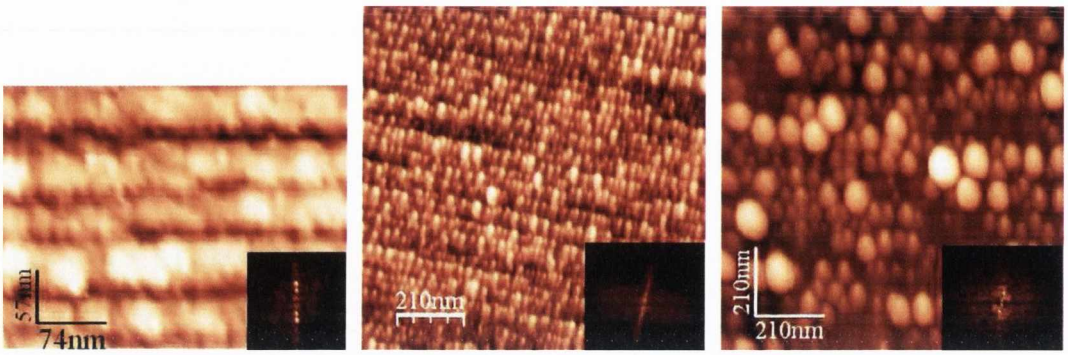

Figure 7.13: AFM images of silver nanoarrays (a) before and after post annealing for 30 minutes at (b)200°C and (c) 400C°C. The Fourier transform highlights the loss of asymmetry and particle alignment.

at 400°C causes the formation of particle agglomerates larger than 100 nm with almost complete loss of any ordered structure. Increasing the temperature to 600°C and finally 800°C results in the complete oxidation of the Ag film.

7.3 Iron and Cobalt nanowires

One of the main advantages of the ATLAS technique is its universality. In order to prove this point, films of cobalt and iron nanowires were deposited on vicinal sapphire. Figures 7.14 and 7.15 show AFM scans of a sample with iron nanowires deposited on vicinal sapphire. In the first case iron was deposited for 35 minutes at 1478°C with a deposition rate of 2.9$\mathring{A}$/min. Discrete islands are visible on the smaller scale (Fig.7.14(a) but they seem to closely connect together towards a nanowire-like configuration. The width of the wire in a direction perpendicular to the steps is 27.5±3.1 nm.

By decreasing the deposition time, nanostructures like the one shown in Fig.7.15 are obtained. The nanowires are now narrower: consistently with the

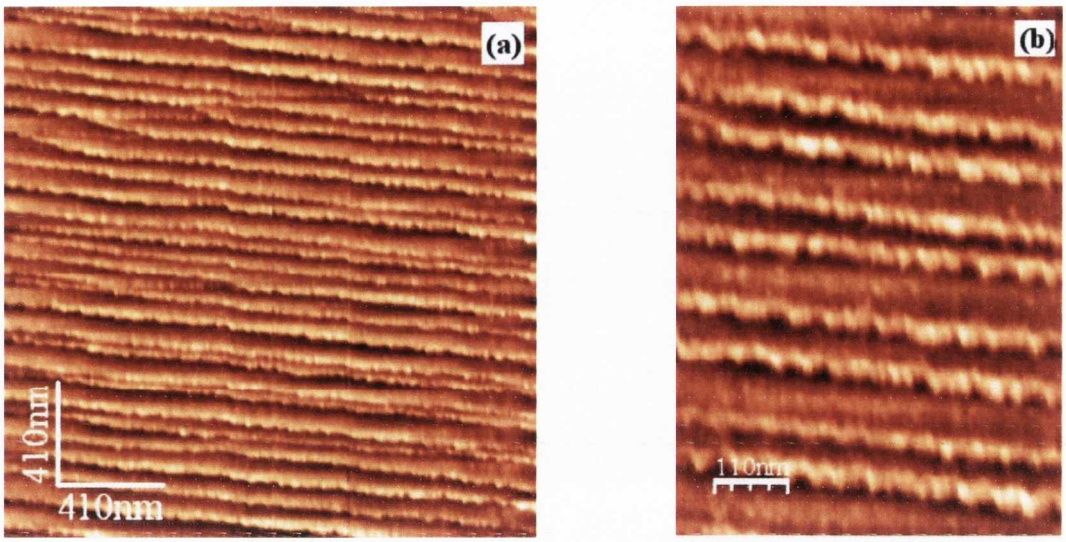

Figure 7.14: AFM images of iron nanoarrays at two different scales for a sample deposited at 1478°C with a rate of 2.94 Å/min.

results obtained for the silver nanoparticles the width is strictly related to the amount of material deposited and it is now 15±2.5 nm.

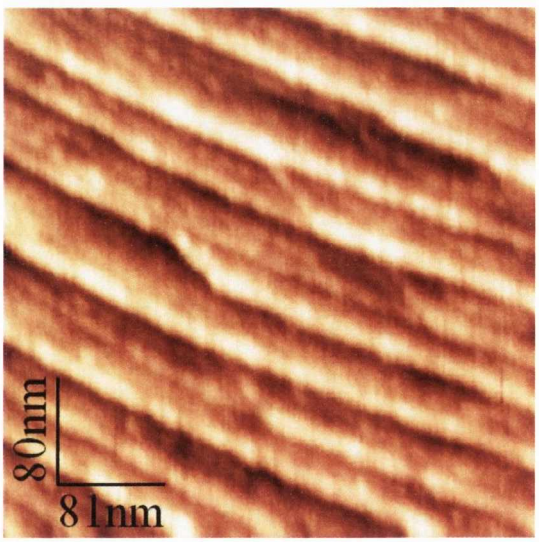

Figure 7.15: AFM images of iron nanowires grown after 18 minutes deposition time at 2.94 Å/min.

Table 7.1 shows the trend of the wires width as a function of the deposition time. The higher the amount of material deposited, the larger the nanowire width. For the longest deposition time the nanowires almost cover the whole terrace and their width approaches the step width.

Table 7.1: Iron nanoparticles average size for the samples considered.

Sample	Dep.Time (min)	Width (nm)	Dev.Standard (nm)
Sa18	18	15	2.5
Sa24	24	17.8	2.4
Sa35	35	27.5	3.1
Sa40	40	39.2	4.3

Cobalt was also deposited on sapphire in order to grow nanowires. Fig.7.16 shows two samples deposited at 1549°C for 24 min(Fig.7.16(a)) and 32 min (Fig.7.16(b)) with a deposition rate of 3.3 $\mathring{A}/min$.

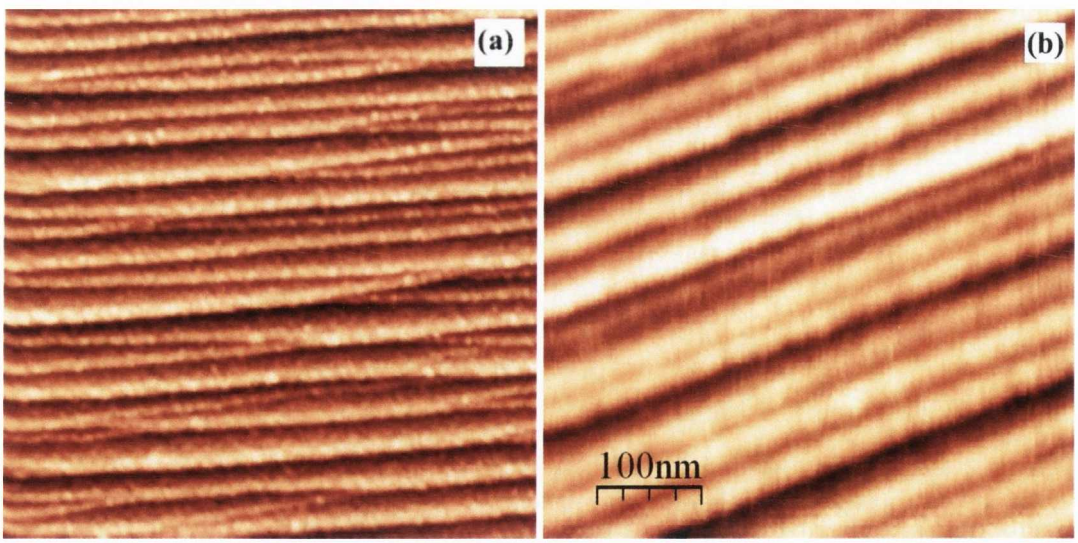

Figure 7.16: AFM images of cobalt nanoarrays at two different scales for a sample deposited at 1549°C for 24 min with a rate of 3.3$\mathring{A}$/min

Fig.7.17 shows a profile of the surface morphology for the sample shown in

Fig.7.16(a).

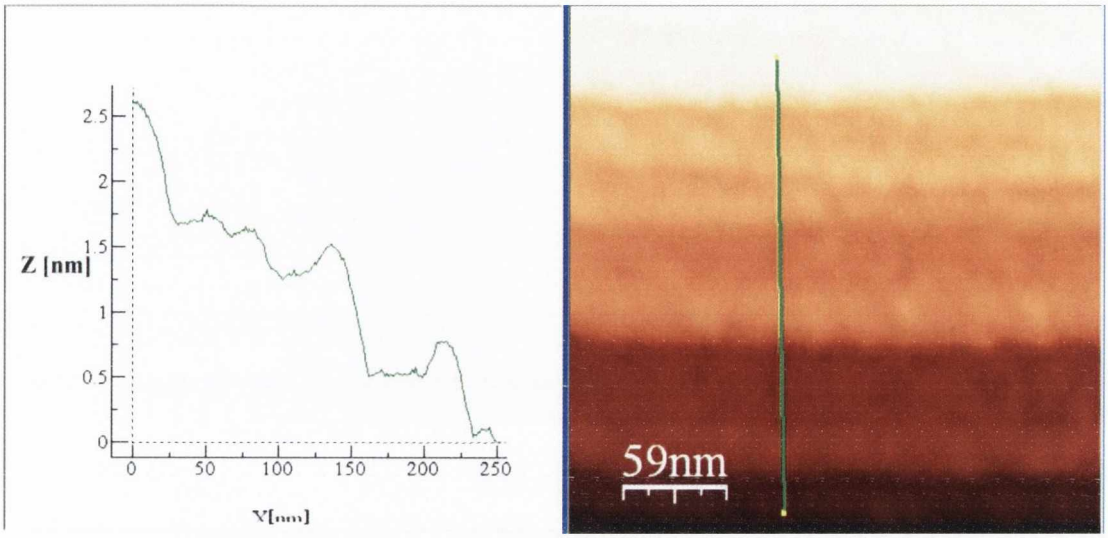

Figure 7.17: Surface profile for the same Cobalt nanowires sample as Fig.7.16.

It can be noticed that the cobalt islands grow on the outer edge of the terrace, similarly to the case observed for silver when deposited in Mode1. This is again due to the steering effect which has a significant importance for the morphology of the growth front. The long-range Van der Waals attraction of the surface to incoming atoms can lead to 'steering' effects which dramatically alter the surface morphology regardless of the materials used [15, 16].

7.4 Conclusions

Since the ATLAS technique is based on geometrical considerations, the orientation of the steps and the angle at which the sample is mounted with respect to the beam are key parameters affecting the final outcome. The deposition angle influences the amount of terrace exposed to the atomic flux and its

modification generates different morphologies. A critical parameter is also the ascending or descending step direction since this can change the exposure angle and leave more or less of the terrace exposed to the beam. It must be said that atom diffusion and the low height of the steps can also affect the morphology. Higher steps are desirable since they allow more freedom with respect to the deposition angle. The morphology of the nanoparticles can be also altered by the long range Van Der Waals interaction between the atomic flux and the vicinal substrate surface. Particularly in the case of ascending step direction, the atoms undergo steering effects which favor the formation of islands on the outer step edge. As can be intuitively understood, the particle size is related to the deposition time and increases with it. Post-annealing of the nanoparticle samples induces a reorganization and gradually destroys the long-range order.

As the ATLAS technique is not material dependent, nanowires of iron and cobalt were routinely produced as well as silver. They show the same parameters dependence as observed for silver but they also show an increased wetting forming nanowires more than nanoparticles arrays.

References

[1] I.V. Shvets, H.C. Wu, V. Usov, F. Cuccureddu, S.K. Arora, and S. Murphy. *Appl.Phys.Lett.*, 92:023106, (2008).

[2] S. Camelio, D. Babonneau, D. Lantia, and L. Simonot. *Europhy.Lett*, 79:47002, (2007).

[3] Y. Cao, W. Liu, J. Sun, Y. Han, J. Zhang, S. Liu, H. Sun, and Guo J. *Nanotechnology*, 17:2378, (2006).

[4] G. Erdelyi, M. Barkoczi, E. Moya, H. Giordano, I. Beszeda, B. Aufray, and D.L. Beke. *J.Appl.Phys.*, 80:1474, (1996).

[5] L.H. Chan and E.I. Altman. *Phys.Rev.B*, 66:155339, (2002).

[6] K.R. Roos, K.L. Roos, M. Horn-von Hoegen, and F.J. Meyer zu Heringdorf. *J.Phys.: Condens. Matter*, 17:S1407, (2005).

[7] Y.P. Zhang, Z.Y. znd Zhao. *Appl.Phys.Lett.*, 89:023110, (2006).

[8] R.A. Zhachuk, S.A. Teys, A.E. Dolbak, and B.Z. Olshanetsky. *Surf.Sci.*, 565:37, (2004).

[9] K. Luo, X. Lai, C.W. Yi, K.A. Davis, K.K. Gath, and Goodman D.W. *J.Phys.Chem.B*, 109:4064, (2005).

[10] K Robbie and M.J. Brett. *J.Vac.Surf.Films*, 15:1460, (1997).

[11] J. Shen, W. Shan, Y. Zhang, J. Du, H. Xu, K. Fan, W. Shen, and Y. Tang. *Chem. Commun.*, 24, (2004).

[12] T. Yamamoto, K. Machi, S. Nagare, K. Hamada, and M. Senna. *Sol.St.Ion.*, 172:299, 2004.

[13] T. Donnelly, B. Doggett, and J.G. Lunney. *Appl.Surf.Sci.*, 252, (2006).

[14] c.H. Liu, Z.P. Li, B.A. Du, X.R. Duan, and Y.C. Wang. *Anal.Chem.*, 78:3738, (2006).

[15] S. Van Dijken, L.C. Jorritsma, and B. Poelsema. *Phys.Rev.Lett.*, 82:4038, (1999).

[16] S. Van Dijken, L.C. Jorritsma, and B. Poelsema. *Phys.Rev.B*, 61:14047, (2000).

[17] J. Amar and J. Yu. *Proc.Int.Conf.Comp.Nanosci.Nanotech*, 8:163, (2002).

[18] J. Seo, S.M. Kwon, H.Y. Kim, and J.S. Kim. *Phys.Rev.B*, 67:121402R, (2003).

Chapter 8

Plasmon Resonance on silver nanoparticle arrays

μῆνιν αειδε θεὰ Πηληϊάδεω 'Αχιλῆος
ουλομένην, η μυρί 'Αχαιοῖς αλγε' εθηκεν
(Sing, goddess, the rage of Achilles the son of Peleus,
the destructive rage that sent countless ills on the Achaeans...)
Homer (Iliad, I)

8.1 Introduction

Silver nanoparticle arrays were grown by means of the ATLAS technique. The details of the technique and of the growth have already been presented in

the previous chapters. This chapter will focus on the characterization of the nanoarrays by means of optical analysis [1, 2, 3, 4, 5, 6, 7]. In order to highlight the dependence of the optical response on the nanoarrays peculiarity, three different samples will be compared. They were all grown in the same system at the same room temperature, using the same deposition rate (3.6 $\AA$/min) and deposition angle (6°). The first sample, Sa15, was grown by depositing silver for 15 minutes; the second, Sa23, was grown with a deposition time of 23 minutes and finally the third, Sa30, was produced with a 30 minutes deposition. The growth parameters are reported in Table 8.1 while Table 8.2 reports the nanoparticles features.

Table 8.1: Growth parameters for the three samples considered.

Sample	Dep.time[min]	Nom.th.at 3°[nm]	Dep.angle[deg]	Dep.temp.[°K]
Sa15	15	0.29	3	298
Sa23	23	0.45	3	298
Sa30	30	0.58	3	298

Table 8.2: Nanoparticles features for the three samples considered.

Sample	Avg width[nm]	Avg height[nm]	Avg spacing(peaktopeak)[nm]
Sa15	31.4±5.6	2±0.5	55.1±22.3
Sa23	14.7±3.7	2.2±0.3	18.8±5.8
Sa30	20.6±3.7	2±0.5	25.4±5

The samples were characterized by Atomic Force Microscopy (AFM) in tapping mode and by UV-vis optical absorption. In order to highlight the anisotropy of the nanoarrays the light was shone in the normal direction with respect to the sample and two different experiments were carried out on each sample. In one of them the light was linearly polarized with the polarization direction longitudinal with respect to the nanoarrays. In the second case the

polarization direction was transversal. Characterization was performed in the first few minutes after the sample was taken out of the chamber.

8.2 Results and discussion

8.2.1 Dipole-dipole interactions in silver nanoparticles arrays

In Fig.8.1 AFM pictures, on a different scale, of the sample Sa15 are reported. It can clearly be seen that the nanoparticles are well aligned along the steps. Nevertheless the sample shows also some lack of uniformity in the way the particles are distributed along the steps. Some areas seem to have a higher concentration where the nanoparticles merge together in groups of three or four; while at the same time gaps within the same nanoarray appear, showing discontinuity. The lack of uniformity is also highlighted by the statistical properties of the nanoparticles since the high standard deviation of the nanoparticle distance is due to the presence of discontinuities.

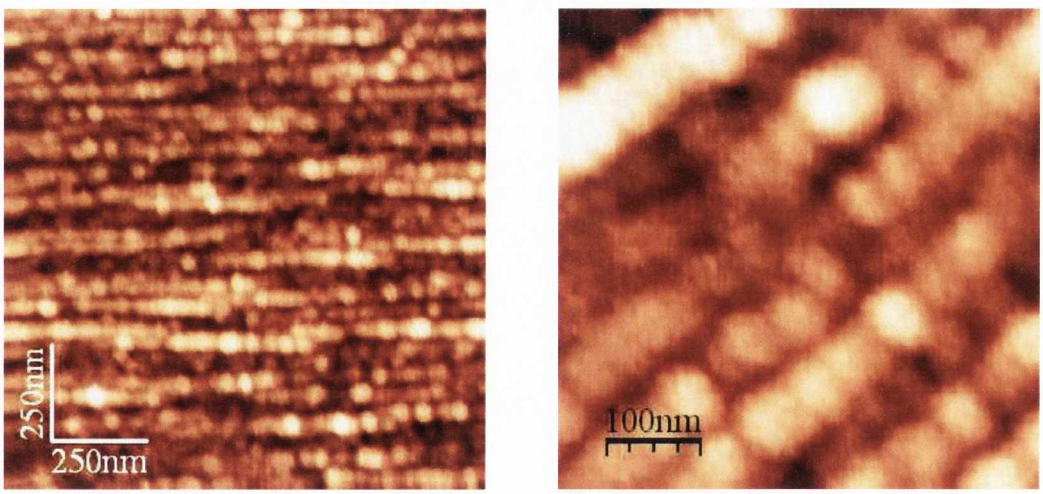

Figure 8.1: AFM image Ag nanoparticles arrays on Sa15 sample.

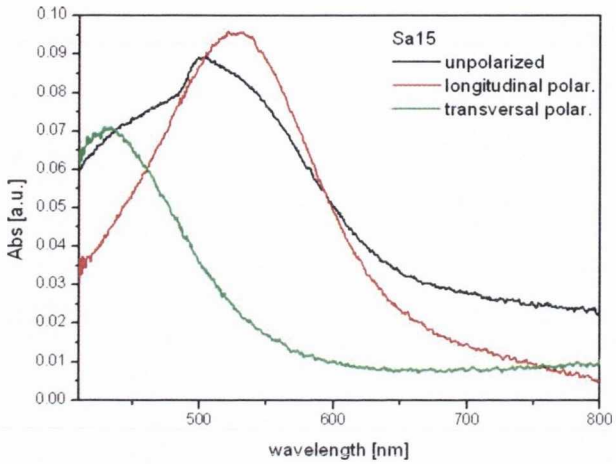

Figure 8.2: UV-Vis of sample Sa15.

The optical response given by this sample is shown in Fig.8.2. As already mentioned, silver and gold are known to give a strong absorption peak in the visible range due to plasmon resonance. The black curve shows the nanoparticles absorption with a peak at around 502 nm. This curve is related to the unpolarized light and presents a pronounced shoulder on its left side. Such asymmetry is related to the intrinsic anisotropy of the sample and it is basically due to the sharing of two different contributions. The use of polarized light makes possible to separate the two contributions which are also shown in the graph: the red curve (peak at 526 nm) refers to the longitudinal polarization of the light while the green one (peak at 432 nm) refers to the transversal polarization.

The observed effect can be interpreted in terms of dipole-dipole interaction [2, 8, 7]. The presence of an electric field causes the confined electrons of the single nanoparticle to be displaced from their equilibrium position with respect to the positive ion core. The surface charge distribution generated

feels repulsive forces due to the localization of the charge. In the case of closely interacting nanoparticles additional forces come into play. When the driving field is parallel to the nanoparticles array there is a weakening of the repulsive force inside each nanoparticle because the positive charge of one nanoparticle will face the negative charge of the neighboring one as shown in Fig.8.3(a). This attractive Coulomb force will lead to a lower resonant frequency resulting in a redshift of the resonance peak. When the driving field is normal to the nanoparticle arrays the charge distribution is such that neighboring nanoparticles will have the same kind of charge on same side giving rise to an additional interparticle repulsive interaction which enhances the resonant frequency and blueshifts the resonance peak to lower wavelengths (Fig.8.3(b)).

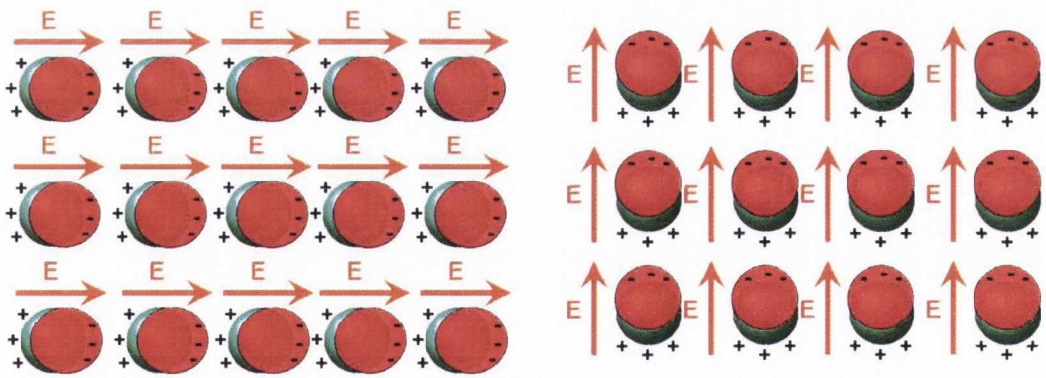

(a) Longitudinal dipole-dipole interaction

(b) Transversal dipole-dipole interaction

Figure 8.3: Dipole-dipole interaction in Ag nanoparticles arrays.

The plasmon resonance in nanoparticle arrays is thus related to the interaction between the nanoparticles and depends in turn on the morphology and distribution of the islands on the substrate.

Fig.8.4 shows a comparison of optical spectra belonging to three different samples. The black curve refers to the sample previously discussed and shown in Fig.8.1(a). The red curve belongs to the sample Sa23 shown in Fig.8.5.

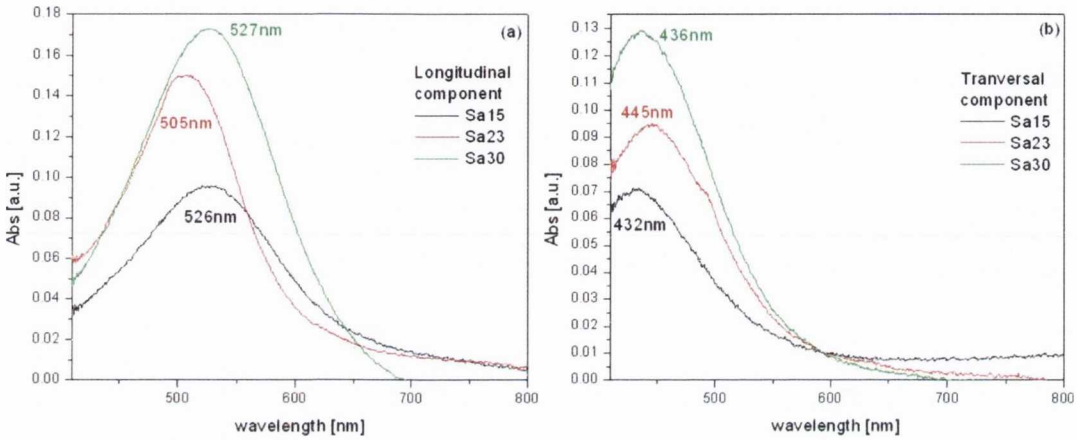

(a) Longitudinal polarization.

(b) Transversal polarization.

Figure 8.4: Optical absorption spectra of Ag nanoparticles arrays.

Sa23 shows a better general uniformity. The nanoparticles homogeneously decorate the steps without gaps and their size seems to be very regular. This is actually confirmed by the small standard deviation of 3.7 nm. Although the quantity of material deposited is larger than for Sa15, the resulting particles are smaller as result of the more regular morphology they assume on the surface. This is reflected in the overall shift of the plasmon resonance peak. The smaller size influences actively the optical response and its contribution affects it more than the peak to peak distance. In fact, the peak to peak distance accounts for the distance between the peak of the islands but, due to the conical shape of the nanoparticles, the distance at the base is related to the particle lateral size as seen from AFM. The smaller particles are actually further from each other and this ends up in a reduced interaction. The absorption spectrum highlights

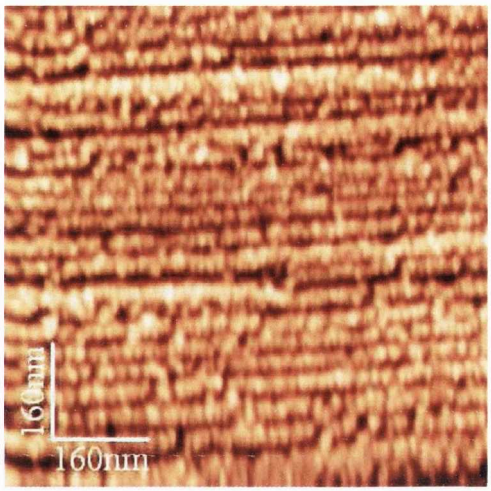

Figure 8.5: AFM image of sample Sa23, 800nmx800nm

this situation: longitudinal and transversal resonance peaks are less shifted as results of a decreased interaction.

An increase in deposition time generates larger nanoparticles (Fig.8.6).

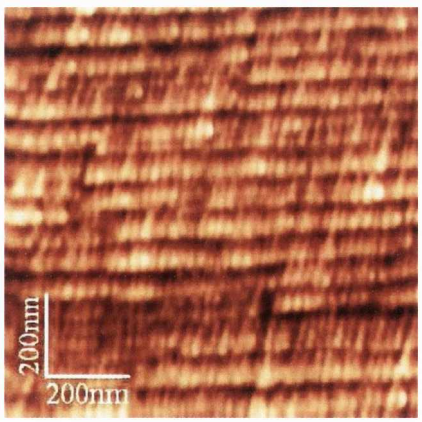

(a) AFM image 1μmx1μm

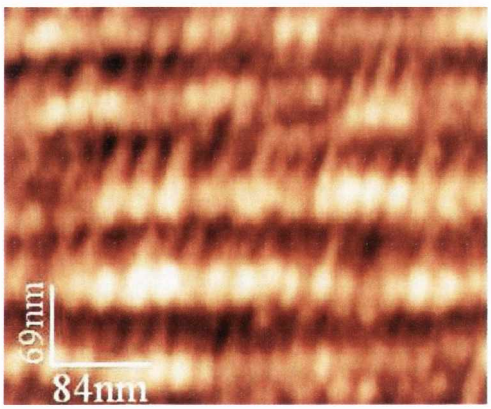

(b) AFM image 420nmx350nm

Figure 8.6: AFM image of Ag nanoparticles arrays on Sa30 sample.

In terms of surface morphology Sa30 resembles closely Sa23. The nanoparticles are regularly sized and spaced and their distribution is uniform. There

are no large gaps between them or between the arrays (the deviation standard is actually small). The interaction between the particles within each array is enhanced and this causes the resonance peaks to be further shifted. The longitudinal component red-shifts from 505 nm to 527 nm while the transversal one blue-shifts at higher frequencies, from 445 nm to 436 nm.
A closer look reveals that the resonance peaks of the last sample, Sa30, are very close to the ones belonging to Sa15. This fact is an example of how the morphology of the sample can heavily affect the optical response. These two samples have different features, nanoparticles size, distance etc. so one would expect two significantly different spectra. However, their resonance curves are very similar and this is due to the fact that the optical response is an average response coming from the whole sample and the overall response of a very uniform sample could be the same as a very irregular one. In the latter the high concentration areas have an enhanced interaction so that the local contribution given by them can account for the empty areas and the overall response is comparable with the one given by a uniform sample.

Fig.8.7 summarizes the information obtained for the considered samples. The resonance peak frequency shifts to lower values, and so redshifts, for the longitudinal component but increases, blueshifts, for the transversal component (Fig.8.7(a)). The difference between the peaks increases with the size of the nanoparticles since the interaction is enhanced and the shifts more pronounced. It reaches a plateau at some stage but it is necessary to remember that when the nanoparticles are too large, presumably over 30-40 nm, addi-

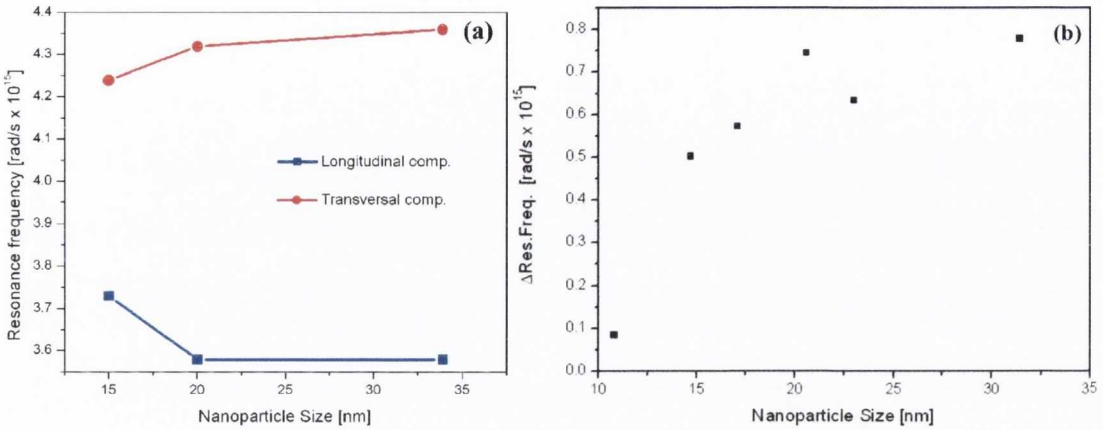

Figure 8.7: Resonance frequency trend versus the particle size. The shifts are due to an increased interparticle interaction, particularly visible in (b).

tional effects come into play. First, the oscillation of the free electron cloud are not necessarily coherent along the array and the phase lag can create retardation effects and modify the optical behavior. At the same time larger particles can be characterized by the presence of higher multiple excitations such as quadrupole, octupole etc. Figure 8.7b shows the difference between the two resonance polarizations as a function of the nanoparticle size for several samples. The trend is clearly ascending since a larger difference corresponds an enhanced interaction.

Integrated optics and photonics can take advantage from linear arrays of closely spaced nanoparticles which can transport electromagnetic energy below the diffraction limit [2, 7, 9, 10, 11, 12, 13]. The guiding and the amplification of the light can be realized at smaller scale compared with normal optical waveguides, due to the near-field coupling between the metal nanoparticles. The oscillating dipole field can be expressed through the three terms [14]:

$$\mathbf{E}_D = \mathbf{E}_F + \mathbf{E}_M + \mathbf{E}_R \tag{8.1}$$

In the quasistatic limit, R<< λ, the Förster field $\mathbf{E}_F$, which has a d^{-3} distance dependence, is dominant and represents the interaction between two close dipoles [15]. Due to the coupling, the nanoparticle arrays support one longitudinal and two transversal modes of propagating waves. Estimates of the energy propagation length were analyzed starting from approximations [9] while other studies concentrated on dispersion properties, showing that the group velocity for energy transport is the highest for excitation at the single particle plasmon frequency. Brongersma et al. developed an analytical model that describes these interactions in the dipole limit showing the dispersion relation for coupled plasmon modes and the propagation of electromagnetic energy through corners and tees [10]. Every oscillating dipole in the chain produces an electric field $E_{i,m}(t)$ at neighboring locations given by:

$$E_{i,m}(t) = \frac{\gamma_i p_{i,m}(t)}{4\pi\varepsilon_0 n^2 d^3} \tag{8.2}$$

where γ_i is a polarization dependent constant, $p_{i,m}$ is the magnitude of the induced dipole, ε_0 is the free space permittivity, n the refractive index of the medium and d is the center to center distance between the particles. For a chain of Hertzian dipoles, where $p_{i,m}=qx_{i,m}$ with q the charge and $x_{i,m}$ the distance from equilibrium at the point m in the chain, the equation of motion is:

$$\ddot{p}_{i,m} = \omega_0^2 p_{i,m} - \Gamma_I \dot{p}_{i,m} + \frac{\Gamma_R}{\omega_0^2}\dddot{p}_{i,m} - \gamma_i \omega_1^2 (p_{i,m} + p_{i,m+1}) \tag{8.3}$$

The first term is the dipole eigenmotion at angular resonant frequency ω_0 while the second and third term are related to the plasmon damping along the chain. Γ_I is a constant accounting for the electron relaxation frequency due to interaction with phonons, electrons, lattice defects and impurities while Γ_R is due to radiation into the far field. The last term accounts for the electrodynamic interaction between dipoles at neighboring positions, m-1 and m+1, and is responsible for the propagation wave solutions. The coupling strength is given by the factor:

$$\omega_1^2 = \frac{qe}{4\pi m^* \varepsilon_0 n^2 d^3} \tag{8.4}$$

In this equation q is the oscillating charge, m^* is the optical effective electron mass and e the electron charge. Solutions to eq.8.3 for a propagating wave assume the form:

$$p_{i,m} = P_{i,0} exp[-\alpha m d + i(\omega t \pm k m d)] \tag{8.5}$$

where the minus signs refers to a situation where phase and group velocity are parallel while the opposite is valid for the plus sign. $P_{i,0}$ is the dipole magnitude at the m=0 point in the direction i while α is the attenuation coefficient which provides the plasmon damping per unit length. From here a dispersion relation can be derived:

$$\omega^2 = \omega_0^2 + 2\gamma_i\omega_1^2 cos(kd)cosh(\alpha d) \tag{8.6}$$

and for small damping αd$\ll$1:

$$\omega^2 = \omega_0^2 + 2\gamma_i\omega_1^2 cos(kd) \tag{8.7}$$

Through the model an estimate of the group velocity v_g and the attenuation coefficient α can be obtained. The group velocity is equal to:

$$v_{g,i} = \frac{d\omega}{dk} = \frac{\frac{d\omega^2}{dk}}{\frac{d\omega^2}{d\omega}} = \frac{\gamma_i\omega_1^2 dsin(kd)}{\omega} \tag{8.8}$$

where ω_1^2 determines the coupling strength and ω is the resonance frequency. In the regime of small damping the attenuation coefficient is:

$$\alpha = \frac{\Gamma_I + (\omega^2/\omega_0^2)\Gamma_R}{2v_g} \tag{8.9}$$

where Γ_I is the electronic relaxation frequency due to interactions with electrons, phonons, defects, impurities etc. Its magnitude is related to the mean free path of the electrons in the metal nanoparticles which is reduced to the bulk value because of inelastic collisions with the particle surface.

The application of this model to our nanostructures, linear arrays of 15nm large particles with a center-to-center distance of 20nm, provides an estimate of the group velocity for the longitudinal plasmon equal to 1.3x10^{9}m/s. The attenuation coefficient for the propagating wave in the same direction is then 4.3x10^{4}m^{-1} corresponding to a decay length of 25μm. This value is in the same

range as reported for metal nanowires with propagation distances that go over 10 μm and increase to 20μm at a wavelength of 500 nm [16, 17]. In reality, although silver is the metal with the lowest losses in the visible spectrum, the decay length could be lower since the small volumes of the particles and the surface roughness can give rise to a higher scattering probability and defects which result in an increased damping of the plasma oscillation and greater energy losses [9, 18]. On the other hand, the high proximity of the nanoparticles to each other could give rise to a better coupling and a stronger near-field interaction with enhanced propagation. Also, the ratio of interparticle distance over the particle radius is 2.7, close to the optimum value of 3 for which the minimum transmission loss is observed according to Quinten et al. [9].
Unfortunately, an exact quantitative comparison with the experimental results cannot be done for various reasons. First, in order to verify the propagation length of the plasmon only the first particle of the chain should be irradiated by the light field with the coupling being responsible for the oscillation of the rest of the chain. The experimental spectra we show are obtained by irradiating all the particles at the same time and cannot offer experimental evidence for transporting energy. Nevertheless, the shift of the resonance peak proves that strong near-field coupling, which in turn is the mechanism for energy transport, is present. Assuming the validity of the model we propose an effective way to realize aligned nanostructures which can operate as transmission lines of electromagnetic energy. Second, in the real experimental case the inter-arrays distance is smaller than the wavelength of light and this could give rise to crosstalk between adjacent arrays. In any case, even considering the interplay

between parallel arrays as a near-field interaction, the interparticle distance inside the same array is much lower than the distance between different arrays and since the near-field shows a d^{-3} dependence the particle-particle interaction inside the array is expected to be dominating. Finally, a quick estimate of the attenuation coefficient and the related signal loss can be obtained from far-field measurements evaluating the peak splitting and the linewidth [19]. However, the experimental spectra do not allow an estimate of the oscillation decay time since statistical effects play a substantial role with the particle size distribution responsible for generating an inhomogeneous broadening of the absorption line.

Previously the effect of the morphology on the optical response was mentioned. In order to clarify the concept two samples with the same features and grown with the same parameters were compared. Silver was deposited on vicinal sapphire for 23 minutes at 3.75 $\AA$/min producing arrays of nanoparticles with comparable size, distance and array interspacing.
From analysis of AFM pictures (Fig.8.8), the nanoparticles show a different morphology. There is a lack of uniformity with an abundance of merging points and gaps for the first sample in contrast with the second which displays a regular alignment of the nanoislands. The reason for this is in the different step-and-terrace morphology of the underlying substrate.

The optical analysis performed on this sample and shown in Fig.8.9 confirms that morphology plays an important role in determining the collective

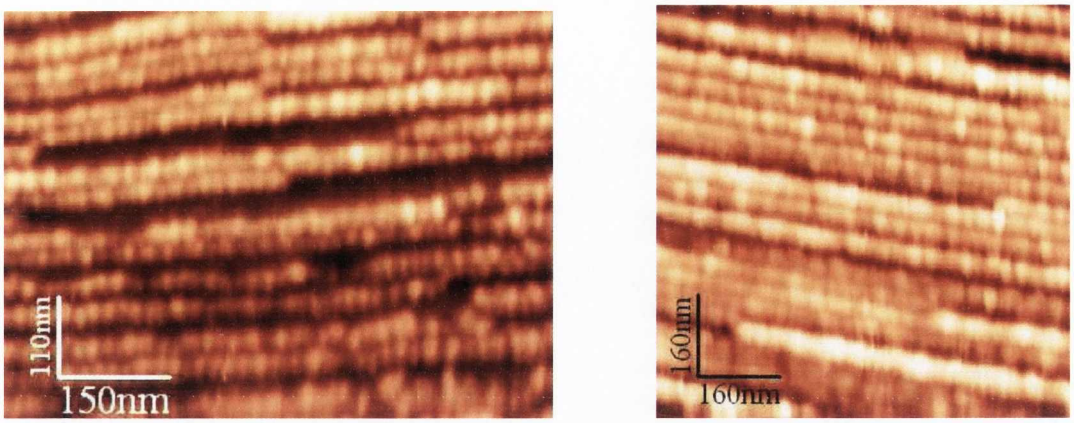

(a) AFM image 750nmx550nm

(b) AFM image 790nmx790nm

Figure 8.8: AFM image Ag nanoparticles arrays grown on a)irregular and b)regular substrates.

response of the sample to the light electric field. Despite having comparable characteristics there is a significant 15 nm difference in the response of the transversal component. The reason for this could be due to an enhanced interaction in some areas of the sample, likely the steps merging points where the nanoarrays join together creating an unpredictable situation.

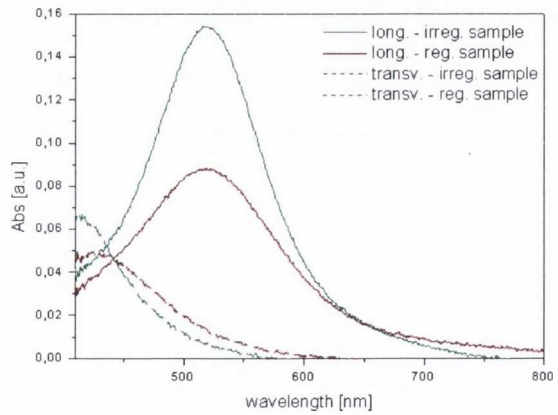

Figure 8.9: UV-Vis of Ag nanoparticle arrays grown on substrates with different step-and-terrace morphology.

8.2.2 Annealing

In the previous chapter, the surface evolution of the metal nanoparticles due to the post-annealing in air was shown (Figure 7.13). It is expected that the optical response will also show a dependence and change related to such evolution. Figure 8.10 reports the optical spectra recorded after each annealing stage.

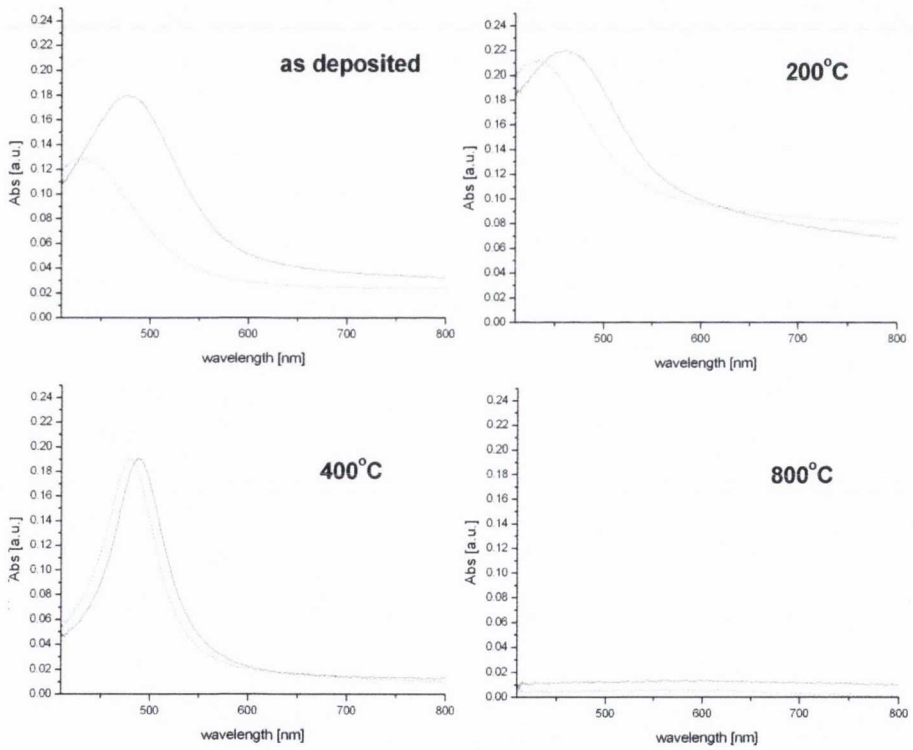

Figure 8.10: Uv-Vis spectra of silver nanoparticles on a sapphire sample as-deposited (a) and after annealing at (b)200°C, (c)400°C and (d)800°C.

After 30 minutes at 200°C the nanoparticles start to coalesce and overcome the steps creating a slight loss of anisotropy. This process drives to less ordered morphology where the arrays are partially losing their order. From an optical

point of view, this condition manifests as a reduced splitting of the peaks. Since the difference between the longitudinal and transversal component is due to the presence of an inhomogeneous morphology, a partial homogeneous reorganization starts to minimize the difference, resulting in a less pronounced peak shift. At 400°C anneal temperature, the particles become larger than 100nm and are no longer ordered along the arrays: the sample becomes more isotropic as confirmed by the near absence of peak splitting. Above this temperature, i.e. increasing up to 600°C, the resonance peaks are leveled and no apparent splitting is visible due to the complete loss of anisotropy. The plasmon resonance eventually disappears after annealing at 800°C with the silver film being completely oxidized.

8.3 Conclusions

The optical properties of silver nanoparticles arrays were investigated by means of UV-vis spectroscopy. Silver gives a strong absorption peak in the visible range due to plasmon resonance. Due to the intrinsic anisotropy of the nanoarrays, the samples respond in a different way to the longitudinal and transversal polarization and the use of polarized light makes possible to explicit the two contributions. The peak is then split and the observed effect can be interpreted in terms of dipole-dipole interaction. The electric field causes the confined electrons of the single nanoparticle to be displaced from their equilibrium position with respect to the positive ion core. The surface charge distribution generated feels repulsive forces due to the localization of the charge. Since the particles in the array are closely interacting additional forces have to be considered.

When the driving field is parallel to the nanoparticles array the repulsive force is weakened inside each nanoparticle (the positive charge of one nanoparticle faces the negative charge of the neighboring one) and the attractive Coulomb force lowers the resonance frequency. The opposite happens for the case of a driving field normal to the nanoparticle arrays. In the latter case, an additional interparticle repulsive interaction enhances the resonant frequency and blueshifts the resonance peak.

The surface morphology plays a significant role and affects the overall optical response of the samples. Samples with different nanoparticle sizes, separations etc. can show similar resonance curves due to the fact that the optical response is an overall average response [2]. A very uniform and an irregular sample can give the same response: the areas with high concentration of nanoparticles in the irregular morphology have an enhanced interaction so that the local contribution given by them can account for the empty areas and the overall response is comparable with the one given by a uniform sample.

The aligned nanostructures produced can find applications in integrated photonics as transmission lines of electromagnetic energy since the shift of the resonance peak proves that strong near-field coupling, which in turn is the mechanism for energy transport, is present [7].

It is worth reminding that this chapters and this thesis introduce the optical work on plasmonic "ab initio" in the group since it was never handled before as the group work focuses on different subjects.

References

[1] F. Cuccureddu, S. Murphy, I.V. Shvets, M. Porcu, and H.W. Zandbergen. *Nano Lett.*, 8:3248–3256, (2008).

[2] U. Kreibig and M. Vollmer. *Optical Properties of Metal Particles.* Springer, Berlin, (1995).

[3] B. Choi, H. Lee, S. Jin, S. Chun, and S. Kim. *Nanotech.*, 18:075706, (2007).

[4] E. Fort, C. Ricolleau, and J. Sau-Pueyo. *Nanolett.*, 3:65, (2003).

[5] E. Hutter and J.H. Fendler. *Adv.Mater.*, 16:1685, (2004).

[6] J. Gonzalo, R. Serna, J. Solis, D. Babonneau, and C.N. Afonso. *J.Phys.: Condens.Matter*, 15:S3001, (2003).

[7] S.A. Maier. *Plasmonics.* Springer, Berlin, (2007).

[8] W. Rechberger, A. Hohenau, A. Leiner, J.R. Krenn, B. Lamprecht, and F.R. Ausseneg. *Opt.Comm.*, 220:137, (2003).

[9] M. Quinten, A. Leitner, J.R. Krenn, and F.R. Ausseneg. *Opt.Lett.*, 23:1331, (1998).

[10] M.L. Brongersma, J.W. Hartman, and H.A. Atwater. *Phys.Rev.B*, 62:R16356, (2000).

[11] J.R. Krenn, J.C. Weeber, A. Dereux, E. Bourillot, J.P. Goudonnet, B. Schider, A. Leitner, F.R. Aussenegg, and C. Girard. *Phys.Rev.B*, 99:5029, (2000).

[12] J. Yan, Z. Yuan, and S. Gao. *Phys.Rev.Lett.*, 98:216602, (2007).

[13] K.B. Crozier, E. Togan, E. Simsek, and T. Yang. *Opt.Exp.*, 15:17482, (2007).

[14] B.W. van der Meer, G. Coker III, and S.-T.S. Chen. *Resonance Energy Transfer.* Wiley, New York, (1994).

[15] B.W. Van Der Meer, G. Coker III, and S.Y. Simon Chen. *Resonance Energy Transfer. Theory and Data.* Wiley, New York, (1994).

[16] W.L. Barnes, A. Dereux, and T.W. Ebbesen. *Nature*, 424:824, (2003).

[17] H. Ditlbacher, A. Hohenau, D. Wagner, U. Kreibig, M. Rogers, F. Hofer, F.R. Aussenegg, and J.R. Krenn. *Phys.Rev.Lett.*, 95:257403, (2005).

[18] B. Lamprecht, A. Leitner, and F.R. Aussenegg. *Appl.Phys.B*, 64:269, (1997).

[19] S.A Maier, P.G. Kik, and H.A. Atwater. *Appl.Phys.Lett.*, 81:1714, (2002).

Chapter 9

Discrete Dipole Approximation (DDA)

And since you know you cannot see yourself,
so well as by reflection, I, your glass,
will modestly discover to yourself,
that of yourself which you yet know not of.
W.Shakespeare (Julius Caesar)

As previously stated in the introduction, since exact solutions to the Maxwell's equations are known only for special geometries such as spheres, spheroids, infinite cylinders etc., it is necessary to use numerical approximate methods [1]. The discrete dipole approximation DDA is a powerful numerical method for

calculating the interaction between electromagnetic radiation and objects of arbitrary geometry [2, 3, 4, 5, 6, 7, 8, 9, 10]. In the DDA the optical properties are obtained by discretizing and approximating the target by a finite three-dimensional lattice of polarizable points which acquire dipole moments in response to the external and local electric field. Each dipole may be thought of as representing the polarizability of a subvolume of the target material. The accuracy is strictly related to the number of dipoles used to describe the target. The main drawback is the significant computational time required when the number of dipoles increases. As a solid can be represented by a continuum on a length scale which is large compared to the interatomic spacing, in the same way a continuum target can be represented by an array of polarizable points on length scales that are large compared to the interdipole separation. In response to the electric field they acquire dipole moments which interact each other via their electric fields. One of the main advantages is the flexibility to study objects of complex geometries and also complex composition. The solid object is then approximated by N point dipoles at positions $\mathbf{r}_i$ and polarizabilities α_i with the dipole-dipole distance small compared to the wavelength. The dipole moment is $\mathbf{P}_i = \alpha_i \cdot \mathbf{E}_{ext}(\mathbf{r}_i)$ with $\mathbf{E}_{ext}(\mathbf{r}_i)$ the electric field at $\mathbf{r}_i$ due to the incident wave $\mathbf{E}_{inc,i} = \mathbf{E}_0 \cdot exp(i\mathbf{k} \cdot \mathbf{r}\text{-}i\omega t)$ plus the contribution of the other dipoles:

$$\mathbf{E}_i = \mathbf{E}_{inc,i} - \sum_{i \neq j} \mathbf{A}_{ij} \mathbf{P}_j \tag{9.1}$$

where the second term on the right side of the equation is due to the dipole interaction and $\mathbf{A}_{ij}$ is a 3x3 matrix. The dipole moments $\mathbf{P}_i$ are solved for all

dipoles and scattering and absorption cross sections are then computed.

9.1 Shape and volume effects

9.1.1 Shape effects: oblate and prolate spheroids

We performed computer simulation using a free software called DDSCAT [11, 12, 13]. In order to have an acceptable compromise we used a number of dipoles higher than 15000 for each simulation with a wavelength resolution of 0.5 nm. From AFM analysis the nanoparticles appear much wider than their height with a height/width ratio of around 0.1. Such a shape cannot therefore be suitably represented either by a sphere or an ellipsoid and the most appropriate shape to consider is a spheroid [14]. Geometrically two kinds of spheroids can be identified: prolate spheroids have two short and one long axes and the revolution axis is parallel to one of the major axes while oblate spheroids have two long and one short axes with the revolution axis along the short axis. Since oblate spheroids recall more closely the shape of the experimental nanoparticles, we tried to simulate the absorption spectra of silver oblate and non interacting nanoparticles through DDA. For all the calculations the bulk dielectric constant for silver as measured by Johnson and Christy was used [15]. The effective radius, the radius of a sphere of equal volume, is 3.8. nm. The results for different ratios are reported in Fig.9.1.

It can be seen that when the ratio is increased the particle is ideally deflattened and the peak blue-shifts to higher frequencies. As previously said, the experimental axes ratio resulting from AFM analysis corresponds to 0,1

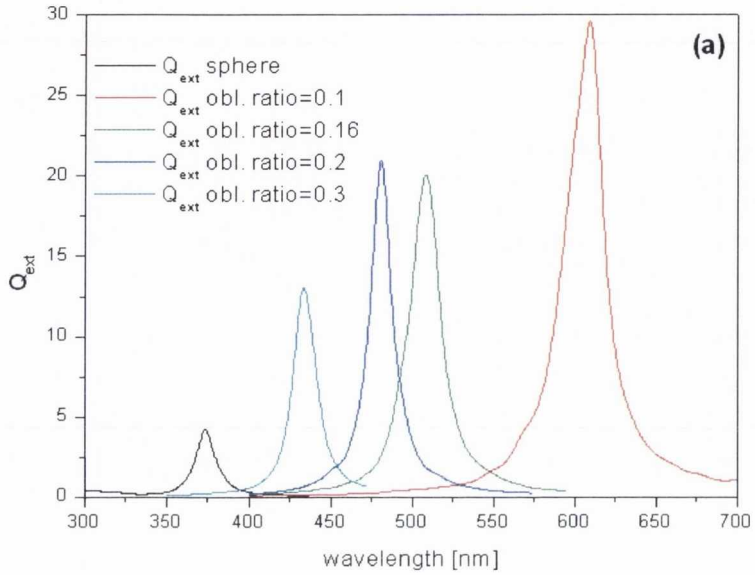

Figure 9.1: DDA optical spectra calculations for oblate spheroids with different axis ratios. Q_{ext} is the extinction factor equal to $C_{ext}/\pi a_{eff}^2$ where C_{ext} is the extinction cross section and a_{eff} is defined through the effective volume: $4\pi a_{eff}^3/3$.

and the DDA simulation for the same value shows a resonance peak above 600 nm. The peaks reported are exclusively due to a shape dependence of the resonance and every possible interaction between the nanoparticles is discarded so they actually show an approximated situation compared to the experimental graphs. In any case, it is worth noticing few points. The resonance wavelength corresponding to a 0.2 ratio is 480 nm, a wavelength located between the two experimental peaks. One can expect that ideal oblate non-interacting nanoparticles would generate a peak in this area and in case of non-interaction the experimental peak would fall around here. This result suggests that the axes ratio for the experimental sample is closer to 0.2 than 0.1 and consequently the particle size assessed by AFM is lacking in accuracy. It is actually known

that AFM tends to overestimate the particle size due to tip convolution. The real nanoparticles width is likely to be around 12-13 nm with a height of 2-2.5 nm. In principle the peak splitting can occur even though the nanoparticles do not interact with each other. Shape effects strongly influence the number of plasmon modes and the position of the resonance peak so that for spheroidal or ellipsoidal particles the ratio between the axes is a fundamental parameter. Non-interacting oblate spheroids have two plasmon modes due to the presence of a long in-plane axis and a short out-of-plane axis. Since the experimental setup used does not offer the possibility to excite the perpendicular mode (the light is shone along the normal to the surface) and both in-plane directions have the same mode (the two in-plane axes are equal), a mere oblate shape does not account for the peak split. The same conclusion is arrived at when considering prolate spheroids. Like the oblate case, non-interacting prolate spheroids have two resonance modes which can both be excited at normal incidence and Fig.9.2 shows DDA spectra of prolate spheroids with different axes ratio.

The simulation results show that a larger ratio corresponds to a larger shift but the wavelength values are significantly blue-shifted compared to the experimental ones. Thus the experimentally observed splitting cannot be assigned to shape effects of non-interacting nanoparticles and the optical properties are determined by the electrodynamic interaction between the particles.

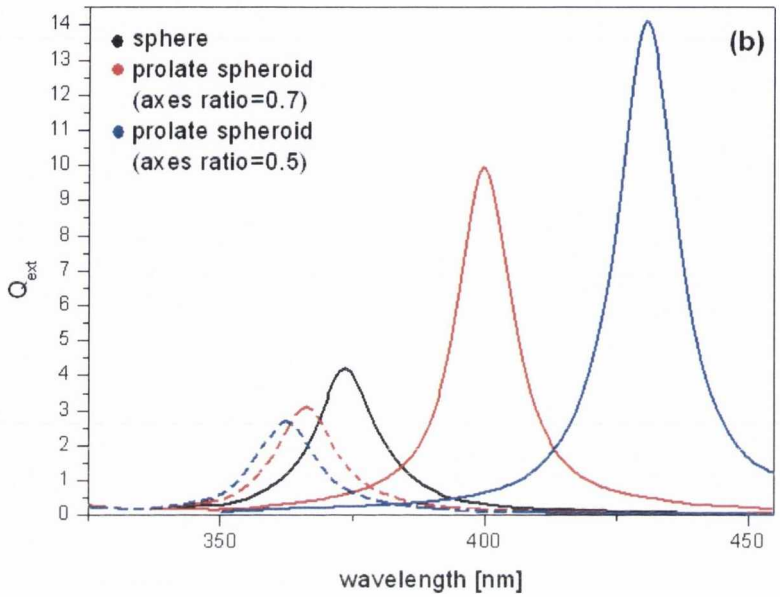

Figure 9.2: DDA optical spectra calculations for prolate spheroids with different axis ratios. Q_{ext} is the extinction factor equal to $C_{ext}/\pi a_{eff}^2$ where C_{ext} is the extinction cross section and a_{eff} is defined through the effective volume: $4\pi a_{eff}^3/3$. The thick line indicates the red-shifted longitudinal component while the dashed line represents the blue-shifted transversal polarization.

9.1.2 Volume effects

As well as being shape dependent, the resonance is also size dependent. Fig.9.3 shows the calculated volume dependence of the resonance peak where the optical response is different for oblate spheroids with different "effective radius".

As the volume changes, the resonance wavelength seems almost unaffected suggesting that the volume effects do not act as strongly as the shape effects. Finally, for small particles the scattering process can be ignored since the absorption dominates the whole extinction. In Fig.9.4 absorption and scattering components are compared for the different volumes considered. As expected for nanoparticles with a small radius the extinction is due almost exclusively

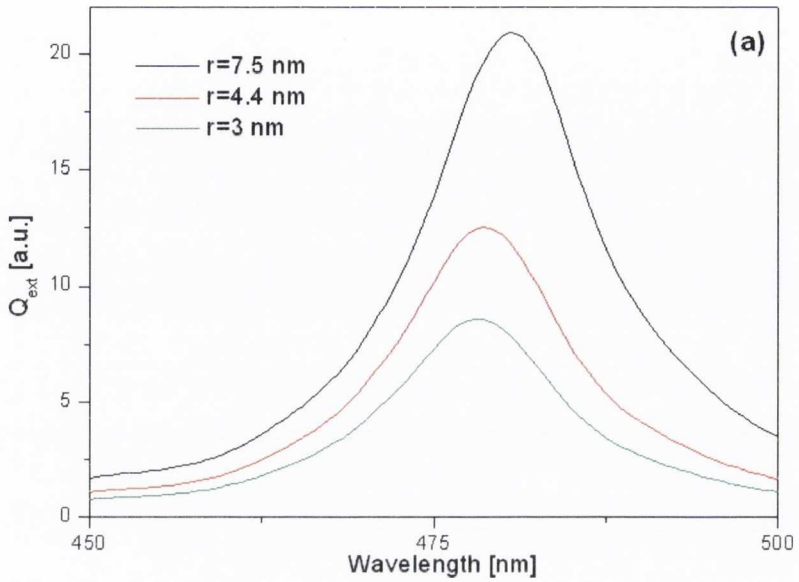

Figure 9.3: DDA optical spectra calculation for oblate spheroids of different effective radius

to the absorption with the scattering component barely visible only for the widest radius.

9.2 Interparticle effects

As seen in the previous section, intraparticle effects cannot be considered responsible for the experimental peak splitting. This is actually due to the interaction between the particles inside the chain which is polarization dependent. When the light is polarized along different directions it stimulates direction-dependent interactions that give rise to different optical responses. This is shown in Fig.9.5 where DDA is applied to arrays of spherical particles with a diameter of 15 nm and a separation along the chain of about 4 nm. An increase in the number of nanoparticles, from 1 to 10, creates an enhanced collective

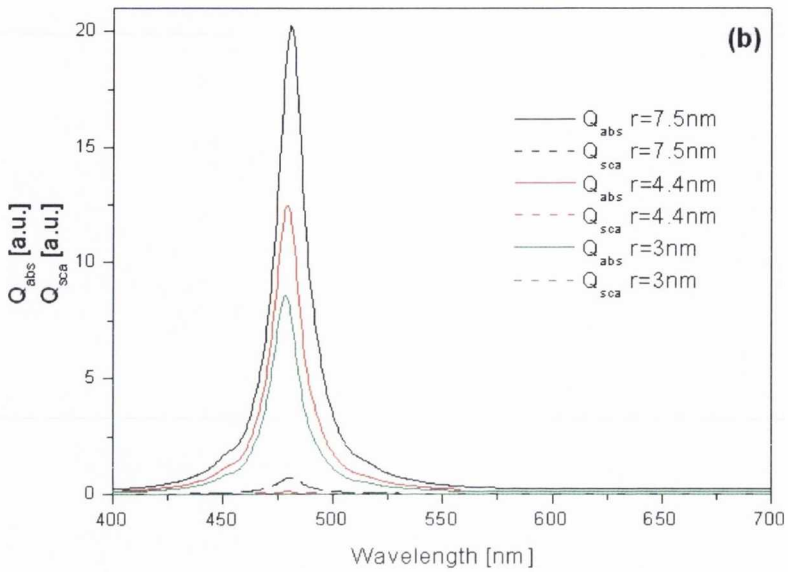

Figure 9.4: DDA optical spectra calculation for oblate spheroids with a comparison between absorption and scattering response.

behaviour responsible for the red- (longitudinal polarization) and blue-shifts (transversal polarization). The mismatch in the resonance wavelength is due to the difference between the model assumed and the real sample: size, shape, particle size dispersions and interparticle separation dispersion play an important role. Nevertheless the model is able to qualitatively depict the system and reproduce the experimental features.

The polarization dependence of the extinction peaks has been extensively explained in the previous chapters recalling a a simple dipole-dipole interaction model. When polarized light strikes the sample the electromagnetic field excites the electron oscillation generating surface charges in every particle. In the case of longitudinal polarization the closely spaced particles will be oriented with attractive electrostatic interaction and this will weaken the internal forces

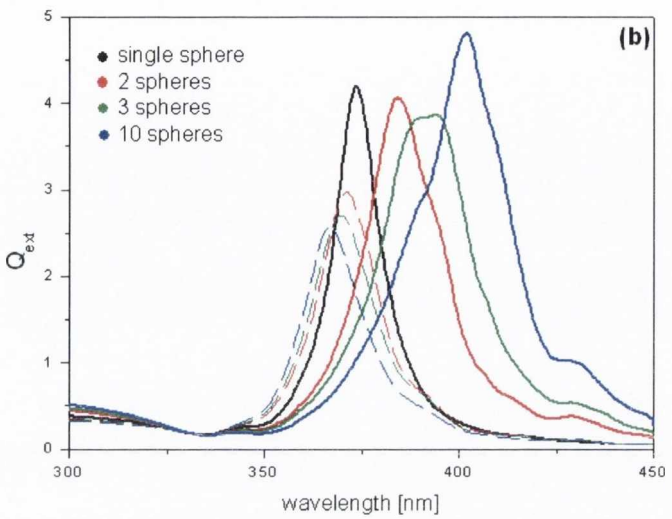

Figure 9.5: DDA optical spectra calculations for a single chain made of 2, 3, and 10 aligned spheres. The thick line indicates the red-shifted longitudinal component while the dashed line represents the blue-shifted transversal polarization.

bringing charges to equilibrium and resulting in a lower resonance frequency and a strong red-shift of the plasmon peak. Conversely, in the transverse case the charge displacement by the electromagnetic wave brings like charges closer increasing the repulsive interaction all along the chain and increasing the resonance frequency with a consequent blue-shift of the band.

The interparticle distance is obviously a critical parameter since the electromagnetic interaction and the peak splitting are strictly dependent on it. Fig.9.6 shows how the resonance peak shifts in an array of ten particle as a function of the distance between the particles. In this case the distance is constant and the particles are equispaced. An increase in the average distance is responsible for a weaker particle-particle interaction with a resulting reduction in the peak shifting. Fig.9.7 shows the difference in resonance between the longitudinal and transversal component as a function of the interparticle distance. The

increase with the particle distance is due to the reduced interaction.

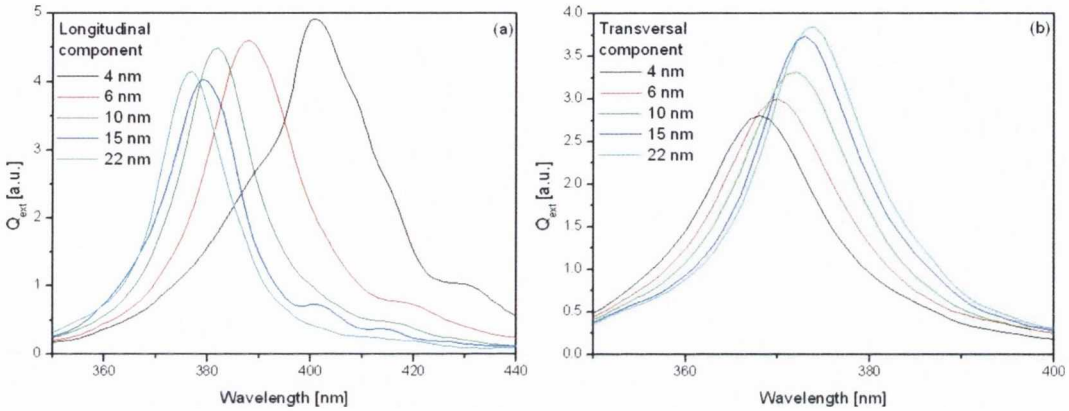

Figure 9.6: DDA optical spectra calculations a single chain made of 10 aligned spheres with different interparticle distance. Longitudinal (a) and transversal (b) component are reported.

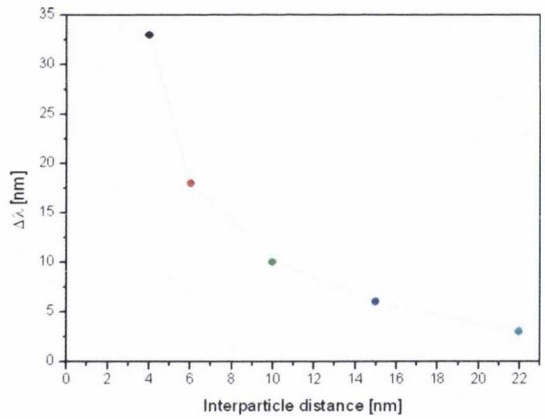

Figure 9.7: Resonance wavelength difference between longitudinal and transversal component for the same systems as Fig.9.6. The dashed grey line is a guide for the eye.

9.3 Defects in the arrays

So far we have considered only arrays of spherical equispaced nanoparticles. In reality the distance between the particles varies and considering an increased or

decreased proximity between some of the particles inside the array can reveal different aspects. For instance, if a small number of particles are more closely spaced the d^{-3} distance dependence of the near-field could allow them to exert a much greater influence on the overall absorption spectrum and maybe cause a spectral shift.

We modified the idealized model by introducing defects inside it in the form of different proximities for some of the particle inside the array. We started with a ten-particle array and varied the distance between two of the particles. Fig.9.8 shows the results obtained in this case.

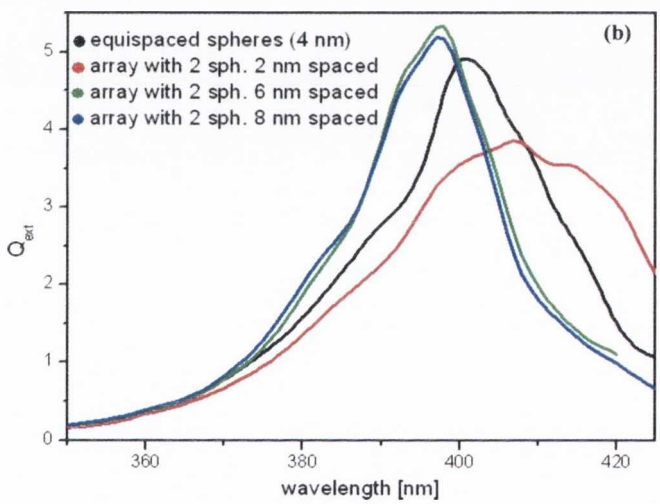

Figure 9.8: DDA optical spectra calculation for an array of 10 particles with modification of the distance between two of them.

Compared to the equispaced array (black line for 4 nm spacing) the introduction of asymmetry generates a peak shift due to the different contribution exerted by the close particles. When the distance between the two is decreased down to 3 nm the peak red-shifts because the interaction, which depends on d^{-3}, is strongly enhanced. Increasing the distance between the two particles

attenuates the near-field interaction and the overall effect is a blue-shift of the peak with respect to the equispaced array. However, there is a cut-off distance after which further increase of the 2 particles distance no longer affects the peak position.

9.4 Conclusions

To better understand the nature of the resonance shift, computer simulations were performed using the Discrete Dipole Approximation (DDA) method, a powerful technique that enables calculation of absorption and scattering of nanoparticles. Since oblate spheroids resemble more closely the shape of the experimental nanoparticles, we simulated the absorption spectra of silver oblate and noninteracting nanoparticles through DDA using this configuration with the field parallel to the long axis. The results obtained suggests that the particle size assessed by AFM lacks in accuracy. Furthermore, the study of particles with prolate and oblate spheroidal shows that the experimentally observed splitting cannot be assigned to shape effects of noninteracting nanoparticles and the optical properties are determined by the electrodynamic interaction between the particles. When the light is polarized along different directions it stimulates direction-dependent interactions that give rise to different optical responses.

Since the presence of defects inside the array could affect the overall optical response compared to a regularly spaced array, we simulated a linear array of 10 nanoparticles where two of them inside the chain are separated by different distances. The results show that the difference in the optical response is due

to a d^{-3} distance dependence: the increased (or decreased) proximity of the two particles affects the peak position as a result of the enhanced (or reduced) near-field interaction. However, there is a maximum distance after which the interaction is no longer significant and the response does not change.

References

[1] U. Kreibig and M. Vollmer. *Optical Properties of Metal Particles.* Springer, Berlin, (1995).

[2] B.T. Draine and P.J. Flatau. *J.Opt.Soc.Am.A*, 11:1491, (1994).

[3] E.M. Purcell and C.R. Pennypacker. *Astrophys. J.*, 186:705, (1973).

[4] B.T. Draine. *Astrophys. J.*, 333:848, (1988).

[5] B.T. Draine and J.J. Goodman. *Astrophys. J.*, 405:685, (1993).

[6] S.B. Singham and C.F. Bohren. *Opt.Lett.*, 12:10, (1987).

[7] H. Portales, N. Pinna, and M.P. Pileni. *J.Phys.Chem.A*, 113:4094, (2009).

[8] N.B. Piller. *Opt.Lett.*, 22:1674, (1997).

[9] M.A. Yurkin and A.G. Hoekstra. *J.Quant.Spectr.Rad.Transf.*, 106:558, (2007).

[10] A. Brioude, X.C. Jiang, and M.P. Pileni. *J.Phys.Chem.B*, 109:13138, (2005).

[11] http://www.astro.princeton.edu/ draine/DDSCAT.6.1.html.

[12] B.T. Draine and P.J. Flatau. *J.Opt.Soc.Am.A*, 25:2693, (2008).

[13] F. Cuccureddu, S. Murphy, I.V. Shvets, M. Porcu, and H.W. Zandbergen. *Nano Lett.*, 8:3248–3256, (2008).

[14] J. Grand, P.M. Adam, A.S. Grimault, A. Vial, J.L. Lamy de la Chapelle, M. Bijeon, S. Kostcheev, and P. Royer. *Plasmonics*, 1:135, (2006).

[15] P.B. Johnson and R.W. Christy. *Phys.Rev.B*, 6:4370, (1972).

Chapter 10

Conclusions and Summary list

Ciascun apra ben gli orecchi,
di doman nessun si paschi;
oggi siàn,giovani e vecchi,
lieti ognun, femmine e maschi;
ogni tristo pensier caschi:
facciam festa tuttavia.
Chi vuol esser lieto, sia:
di doman non c'è certezza.
L.de Medici (Canzone di Bacco)

10.1 Conclusions

During this PhD project a new deposition technique has been developed following the need to create nanostructures on vicinal substrates with a bottom-up

approach. The technique is called Atomic Terrace Low Angle Shadowing (ATLAS) and the ATLAS devices have been designed and developed entirely in our laboratory. ATLAS is a system able to deposit a highly collimated flux onto a substrate at shallow angle. The main capability of the ATLAS device is the possibility to deposit nanowires of any evaporable material on a wide range of substrates, restricted only by the requirement that the latter forms ordered atomic or bunched terraces. Details of the technique concepts are reported in the "Applied Physics Letters" paper published in 2008 [1].

During the project two separate systems have been designed and built "ab initio" to the working stage. The first one (ATLASα) is a prototype, which actually works as a full time growth chamber. The second one (ATLASβ) is an upgraded instrument which allows for greater experimental flexibility.
The design of an UHV system is an extremely time consuming task since it involves different stages that have to be considered in parallel. There are a series of key features to deal with during the design process: from vacuum requirements to desired components to geometry etc. It is worth to remind that prior to the start of this PhD no ATLAS instruments system were designed or built and the whole systems were developed and completed during this project. First of all, the chamber design requires a good deal of time in order to choose the right chamber shape and construction material. The geometry of the main chamber is vital to the full system because influences the possibility to connect additional components (immediately or in the future) and must then be studied with attention. This step was particularly challenging for the ATLASβ

since the first system (ATLASα) was originally thought to be used only for testing the technique and no particular attention was dedicated to the chamber shape. The ATLASα system was built connecting together pre-existing parts from other UHV systems but, at the same time, respecting the requirements that the technique demands. At this stage the chamber required a number of ports sufficient to accommodate the turbomolecular pump, the ion gauge, the sample holder, the thickness monitor and a couple of flanges more to connect, far from the sample, the effusion cell or any other possible component (viewports included).

As regards as the second system, ATLASβ, the designing stage was developed much more carefully. Several shapes for the main chamber were considered in order to fulfill the technique requirements and the necessity to mount many more diagnostic and analytical tools than the prototype. Finally, a cylindric shape with rounded ends was chosen. This shape allows to have the desired distance between sample and material source as well as having a good number of ports for the estimated additional components such as ion guns, loadlock, multiple effusion cells, rotating stages, RHEED etc. The growth chamber was tilted by 30° to fully exploit the capacity of the crucibles in the effusion cells collocated in the upper part of the chamber, opposite the sample.

As every UHV system, both ATLAS presented several technical problems on a daily basis, from leaks to broken parts to routine bakeouts etc. Additionally, ATLASβ was built by using only new parts and a brand new commissioned chamber, requiring the time-consuming periodic interaction with chamber (and components) manufacturer companies to clear up misunderstandings and aris-

ing issues.

After the successful testing of the technique and the assembling of the ATLASβ the first system (ATLASα) was not abandoned due to the positive results and was turned into a full time growth chamber. The main drawback of this system is the lack of a loadlock chamber so that the chamber must be vented each time a sample is loaded or removed. Also this implies that before a new deposition is carried out, a thorough outgassing of the sources procedure is needed and the system has to be routinely baked out to temperatures of about 250°C for several hours, or even days, to achieve pressures below 10^{-7} mbar. This procedure extends the experimental time and limits the throughput of samples. The ATLASβ remedies to these drawbacks by means of a loadlock and definitely offers a higher throughput. Despite its structural problems, the yield of the ATLASα system was brought to optimum and all the results reported in this thesis and in the related papers were obtained by using ATLASα. A detailed description of the instrumentation is reported in a "Review of Scientific Instruments" paper published last year [2].

A necessary requirement for the ATLAS technique is the use of a vicinal surface. At the beginning of the project various materials were briefly explored, such as $SrTiO_3$ (STO), but since the most promising results were obtained with c-plane α-Alumina (or Sapphire), the latter was chosen as a suitable template candidate for the ATLAS technique. Although, as reported in literature, Sapphire can give a step-and-terrace morphology without extremely complex and excessive treatment (usually it only needs annealing in

air at high temperature), it took some time to get the right configuration and stepped morphology. During this project the morphological surface evolution of c-plane alumina samples upon annealing was investigated for flat and vicinal substrates. The samples were annealed for different times at 1100°C. Flat samples did not provide step bunching, but on the contrary miscut samples provided good results since the high temperature annealing process was able to trigger the step bunching process. These results are even more attractive since most of the works reported in literature focus only on flat samples. It was found that a stable configuration shows steps around 1.5-2nm±0.5nm high with an average terrace width around 40-45nm±15nm. The results obtained highlights that it is possible to produce nice ordered and regular step morphologies even at "low" temperature since all the annealing process was performed at 1100°C. In fact, most of the step bunched results in literature are reported to happen at very high temperature, usually over 1200°C. In parallel, it was found that the surface morphology presents a number of coalescence points, i.e. local areas where two steps merge and form multiple steps. Close to the merging areas, parallel steps change direction running along a different, but energetically favorable, low index direction. The AFM studies were confirmed and further analyzed by HR-TEM, in collaboration with Dr.Zandbergen group from TUDelft. The TEM studies showed clearly the bunching of the steps with a great close up on one single macrostep.

From the results obtained C-plane oriented α-alumina proves to be a suitable candidate to act as a template for the nanowire growth using the ATLAS technique. All these results are being collected in a paper which is now in the final

draft before submission [3].

Once the suitable templates were obtained, the ATLAS technique was demonstrated and successfully used to routinely grow linear nanostructures of different materials such as silver, iron and cobalt. The ATLAS technique is based on geometrical considerations and the dependence of the growth morphology on various parameters was investigated.

One of the main parameters is obviously the deposition angle. Intuitively, the deposition angle influences the amount of terrace exposed to the atomic flux and its modification generates a different morphology. This confirmed by the experimental results.

Another critical parameter is also the direction of the steps, ascending or descending, with respect to the flux. This parameter can actually change the amount of terrace exposed to the beam and, in turn, affect the morphology of the final nanostructures. An unexpected result was obtained when the substrate was mounted such a way that the flux stroke the ascending staircase. In this case it was found that the nanoparticles nucleate and grow on the outer step edge, conversely to what expected. This phenomenon has been reported in literature and ascribed to a particular phenomenon called *"steering effect"*. According to it, the morphology of the nanoparticles can be altered by the long range Van Der Waals interaction between the atomic flux and the vicinal substrate. The atoms approaching the substrate surface can experience a steering effect which favors the formation of the islands on the outer step edge. However, these results need further investigations in order to be fully

understood.

Furthermore, the deposition time was found to affect the surface morphology since the particle size is strictly related to it. Longer deposition times bring larger particles.

It was also investigated the effect of a post-annealing procedure on the ordered nanoparticles arrays. In this respect, it was found that the annealing of the nanoparticle samples induces a reorganization and gradually destroys the topological asymmetry.

The nanostructures produced by means of ATLAS were characterized via optical spectroscopy. In particular, the optical properties of silver nanoparticles arrays were investigated by means of UV-vis spectroscopy.

Due to the plasmon resonance phenomenon, silver is able to show a strong absorption peak in the visible range. Since the nanostructures studied present a high degree of anisotropy, they respond in a different way to the longitudinally and transversally polarized light. As a result of the direction dependent response, the resonance peak is split and the observed effect can be interpreted in terms of dipole-dipole interaction. In brief, the electric field causes a redistribution of the confined electrons and since the particles in the array are closely interacting, the overall optical response depends on the field orientation. When the driving field is parallel to the nanoparticle arrays unlike charges on different particles face each other and the attractive Coulomb force lowers the resonance frequency. The opposite happens when applying the driving field normal to the nanoparticle arrays: repulsive interactions enhance the resonant

frequency and blueshift the resonance peak.

The role of surface morphology was also investigated. Samples with different nanoparticle sizes, separations etc. can show similar resonance curves: uniform and irregular samples can, in some cases, show the same plasmonic response due to the fact that irregular samples may have enhanced interaction in a few areas where the concentration of nanoparticles is particularly high. As a result, the overall response of the sample becomes comparable to the one given by a sample with higher uniformity.

The nanostructures produced are quite remarkable in terms of dimension and order. Nowadays, the fabrication of planar and linear arrays of ordered nanowires or nanoparticles is a hot topic and many efforts are being dedicated to the development of new techniques able to produce them. The ATLAS technique, as a consequence of the results obtained, collocates as a novel and alternative method with a promising future. The nanostructures fabricated may find applications in several fields, from biotechnology to integrated photonics as, for example, transmission lines of electromagnetic energy.

The plasmonic resonance results were included in a Nano Letters paper published in 2008 [4].

Interesting preliminary results were also obtained on the iron and cobalt nanostructures measuring hysteresis loops by Alternating Gradient Field Magnetometre (AGFM) and performing Ferromagnetic Resonance (FMR), the latter in collaboration with Dr.R.C.Barklie group, TCD Dublin. These results are currently under further investigation.

To better understand the nature of the resonance shift, computer simulations using the Discrete Dipole Approximation (DDA) method were performed. The optical properties are obtained by representing the target as an array of polarizable point dipoles which acquire dipole moments in response to the external and local electric field. The accuracy is strictly related to the number of dipoles used to describe the target. The main drawback is the significant computational time required when the number of dipoles increases.

Shape and volume effects were initially considered and the results obtained proved that volume effects do not act as strongly as shape effect. In particular, the results obtained by studying particles of different spheoridal shape, oblate and prolate, suggest some lacks in particle size assessment by using AFM. Furthermore, it stands out that, although theoretically possible, the peak splitting cannot be assigned to shape effects of non-interacting oblate or prolate spheroidal particles. The optical properties are determined by the electrodynamic interaction between the particles. When the light is polarized along different directions it stimulates direction-dependent interactions that give rise to different optical responses. This is confirmed by considering arrays made of a different number of nanoparticles at constant interspacing distance. The higher the number, the stronger the overall interaction with a more pronounced peak shifting. Besides, it has been shown that increasing the interparticle distance inside the array corresponds to a reduced shift, due to the decreased interparticle interaction.

Moreover, it was shown that the presence of defects inside the array can affect the peak position.

The DDA simulation results were part of the Nano Letters paper published in 2008 [4].

10.2 Summary

Here is reported a summary list to help resuming the work and the accomplishments achieved during this PhD project and extensively discussed in the present thesis.

- Design, assembling, building, testing and maintenance of the first ATLASα system from the ground up to working stage. Prior to this system no ATLAS devices existed in the group. This system was used for testing and then became a full time growth chamber with an optimal throughput in relation to its limits. All the results obtained and discussed in this thesis in terms of grown nanostructures were obtained by performing the experimental growth with this system.

- Design, assembling, building, testing and commission of the second ATLASβ system from the ground up to working stage. This system was designed and built and then commissioned for being a full time deposition device.

- This PhD thesis produced two separated ATLAS devices which are now part of the existing facilities of the group.

- A study of the morphological evolution of Sapphire upon annealing was performed in order to obtain a suitable template for the ATLAS deposition. "No miscut" and miscut samples were studied by annealing them at 1100°C for several hours. The best results were obtained with the 3°

miscut samples, while usually the results reported in literature focus on "no miscut" samples. Furthermore, stepped morphologies were obtained at lower temperature than the ones reported in literature. HR-TEM micrographs provided confirmation and a remarkable close up of the step bunching process.

- Nanowires and nanoparticles arrays of silver, cobalt and iron were successfully and routinely fabricated by means of the ATLAS technique. A thorough investigation of several deposition parameters (such as deposition angle, deposition time etc.) was carried out in order to determine the dependence of the nanostructures growth and morphology on them. Unexpected results were obtained in relation to the growth of nanoparticles on the outer step edge giving rise to the possibility of further investigations.

- Nowadays, ordered and planar arrays of nanostructures are quite difficult to fabricate by bottom-up approach. Most of the research about nanostructures focuses on top-down lithographic techniques which have their own drawbacks. The nanowires reported in literature which are said to be fabricated by bottom-up approaches usually refer to chemical methods and, most of the times, are made of bunches of threedimensional tangled nanopillars that do not seem very suitable for practical use. Besides, usually planar and ordered arrays of nanowires fabricated by bottom up approaches, seem to be larger in dimensions that the one we propose and obtain at room temperature (10-30nm) by means of ATLAS technique.

To this end, the ATLAS technique, although in its embryonic stage, has produced very interesting results and promises to offer much more with further optimization and full exploitation in the future, collocating as an interesting alternative method.

- Optical characterization of the nanostructures grown by ATLAS (silver nanoparticles arrays) was carried out producing very interesting the results. Due to the anisotropy, the nanoarrays respond in a different way when illuminated with polarized light, the response depending on the direction of the polarization. This results in the peak shift on the UV-vis spectra. To sum up, the nanostructures features can be tailored by playing adequately with the growth parameters and this allows for the plasmonic properties to be tuned, offering the potential to develop new types of photonic devices. It has also been found that the topology of the surface cannot be deduced from measured optical spectra. All these results are part of a Nano Letters paper published in 2008.
  Preliminary results obtained by AGFM and FMR on magnetic, iron and cobalt, nanostructures are under investigation.

- It is worth reminding that this thesis introduced for the first time the optical work on plasmons in the group which was never handled nor faced before. In fact, the work and background of the group focus on different subjects, mainly thin films fabrication, STM and magnetism.

- DDA optical computer simulations were performed to provide a better

insight view of the plasmonics phenomena. The results obtained clarified several issues and in particular confirmed that the peak shifting is entirely due to the interparticle dipole-dipole interaction and not attributable to any particle shape anisotropy. The role of volume, shape, interparticle distance and the presence of defects inside the arrays were considered. Although the group has background with numerical modelling utilising different computational approaches (in particular DFT), DDA was developed for the first time and successfully applied during this thesis project as evolution of the plasmonics studies. The DDA results are included in the Nano Letters paper published in 2008.

References

[1] I.V. Shvets, H.C. Wu, V. Usov, F. Cuccureddu, S.K. Arora, and S. Murphy. *Appl.Phys.Lett.*, 92:023106, (2008).

[2] F. Cuccureddu, V. Usov, S. Murphy, C. O'Coileain, and I.V. Shvets. *Rev.Sci.Inst.*, 79:053907, (2008).

[3] F. Cuccureddu, S. Murphy, I.V. Shvets, M. Porcu, H.W. Zandbergen, N.S. Sidorov, and S.I. Bohzko. *In Preparation.*

[4] F. Cuccureddu, S. Murphy, I.V. Shvets, M. Porcu, and H.W. Zandbergen. *Nano Lett.*, 8:3248–3256, (2008).

I don't want to hear from those who know
They can buy, but can't put on my clothes
I don't want to limp for them to walk...

E. Vedder

...E quindi uscimmo a riveder le stelle.

D.Alighieri

(La Divina Commedia, Inferno XXXIV, 139)